12-2016

Evaluating the performance of passive chilled beams with respect to energy efficiency and thermal comfort

Janghyun Kim
Purdue University

PURDUE UNIVERSITY
GRADUATE SCHOOL
Thesis/Dissertation Acceptance

This is to certify that the thesis/dissertation prepared

By Janghyun Kim

Entitled

Evaluating the performance of passive chilled beams with respect to energy efficiency and thermal comfort

For the degree of Doctor of Philosophy

Is approved by the final examining committee:

James E. Braun Co-chair	Eckhard Groll
Athanasios Tzempelikos Co-chair	W. Travis Horton

To the best of my knowledge and as understood by the student in the Thesis/Dissertation Agreement, Publication Delay, and Certification Disclaimer (Graduate School Form 32), this thesis/dissertation adheres to the provisions of Purdue University's "Policy of Integrity in Research" and the use of copyright material.

Approved by Major Professor(s): James E. Braun

Approved by: Jay P. Gore 12/8/2016

Head of the Departmental Graduate Program Date

EVALUATING THE PERFORMANCE OF PASSIVE CHILLED BEAMS WITH RESPECT TO ENERGY EFFICIENCY AND THERMAL COMFORT

A Dissertation

Submitted to the Faculty

of

Purdue University

by

Janghyun Kim

In Partial Fulfillment of the

Requirements for the Degree

of

Doctor of Philosophy

December 2016

Purdue University

West Lafayette, Indiana

For those people that I love.

ACKNOWLEDGEMENTS

My boss in the military once said, “You can learn at least one thing from any people around you”, and I have tried to learn from all of the people around me ever since. For the past five years, there are so many people who have inspired me and taught me a lot of things in life. So here it goes.

I would like to express my deepest gratitude to both of my advisors, Professor James E. Braun and Professor Athanasios Tzempelikos, for constantly pointing me towards the right direction and questioning me to broaden my knowledge. Without your insight and passion on the research, I don’t think I would have made this far. I truly appreciate your efforts of keeping me in pace.

I would also like to thank Professor W. Travis Horton who was always there as a troubleshooter when I was struggling and frustrated alone in the backyard of Bowen Laboratory. And I would like to thank Professor Eckhard Groll for serving on my dissertation committee and giving me valuable and productive comments.

I have spent a lot of time in my experiments in the Living Laboratories and Bowen Laboratory. Donghun Kim, Jie Cai, Bonggil Jeon, Yeonjin Bae, Orkan Kurtulus, Robert Brown and Donna Cackley helped me to set up and facilitate the experiments that I have done in the Living Laboratories. Miles Evans, Yuwei Hung, Deanna Quickle, David Rundio, Jose Daniel Sanchez and Frank Lee helped me to set up and facilitate the

experiments that I have done in Bowen Laboratory. I appreciate all these people for taking a valuable part in my research.

My Purdue life outside the research was full of excitement and adventure because of Seungkyu Lee, Huisung Kim, Nicholas Kim, Hyunjun Shin and Whitney Emberton Jones. They have supported me at all times even when I was being completely unreasonable. I truly thank for that. And I was able to maintain my competitiveness level in general through my basketball teammates, Yul Kwon, Hyukgyu Kim, Wonkyu Kim and Shinyoung Kim. All those yelling and fighting that we have done in CoRec for several years will never be forget and those numerous games that we have won together will always be my confidence in life.

I would also like to thank my family who made me strong and independent. And for last but not least, Insun Yoon who has been my mental support for the past decade. I can’t even express how much I appreciate your support and sacrifice towards my life. We will always enjoy our life together.

TABLE OF CONTENTS

Page

Page

Page

LIST OF TABLES

Table Page

LIST OF FIGURES

Figure Page

Figure Page

Figure Page

NOMENCLATURE

A	surface area, m^2	**Subscript**	
A'	free area of coil in plan view, m^2/m	*0*	nominal
ACH	air change rate per hour, m^3/hr	*air*	air
AHU	air handling unit	*avg*	average
AUST	area-weighted uncooled surface temp., ^oC	*bot*	bottom
alt	altitude of the location above sea level, m	*bnd*	bonding
C	coefficient or correction factor	*cap*	cooling capacity
CAV	constant air volume	*cc*	cooling coil
c_p	specific heat, J/kg·K	*chb*	chilled beam
D	diameter, m	*chr*	characteristic
d	pipe insertion depth, m	*coi*	coil
E	effectiveness	*con*	convection
e	surface emittance	*cor*	corrected
FC	forced convection effect factor	*cov*	surface cover
fo	free area of bottom perforated surface, %	*ctr*	center
g	gravitational acceleration, m/s^2	*dif*	diffuser
H	height, m	*eqv*	equivalent
HR	humidity ratio, kg_{H2O}/kg_{air}	*fin*	Fin
h	heat transfer coefficient, W/m^2K	*flr*	floor
k	thermal conductivity, W/mK	*fre*	free area
L	length, m	*glb*	globe
LL	Living Laboratory	*i*	inlet
LPD	lighting power density, W/m^2	*ind*	Indoor (air)
$\dot{m}$	water mass flow rate, kg/s	*ini*	initial
NTU	number of transfer units	*inp*	inner pipe
n	number of	*int*	internal load
PCB	passive chilled beam	*lft*	left
P	perimeter, m, or parameter	*m*	mean
pi	room position index	*max*	maximum
$\dot{Q}$	heat extraction rate or cooling capacity, W	*min*	minimum
$\tilde{Q}$	harmonic heat flux oscillation, W	*o*	outlet
$\dot{q}$	volumetric flow rate, m^3/s or l/s	*OA*	outdoor air
R	thermal resistance, m^2K/W	*opr*	operative
Ra	Rayleigh number	*out*	outdoor

RH	relative humidity, %	*otp*	outer pipe
r	linearization factor for cooling, $^oC^3$	*pan*	panel or ceiling surface
s	pipe spacing (surface distance), m	*pcb*	passive chilled beam
T	temperature, ^oC	*pip*	water pipe or tube
t	time	*plv*	pipe level
U	overall heat transfer coefficient, W/m^2K	*r*	return
u	(x-axis) velocity, m/s	*RA*	return air
V	volume, m^3	*rad*	radiation
$\dot{V}$	volumetric flow rate, m^3/s or CFM	*ref*	reference
v	velocity, m/s	*rgt*	right
VAV	variable air volume	*SA*	supply air
W	width, m	*slb*	slab
z	adjustment factor for *AUST*, ^oC	*sup, s*	supply
		surf	surface
Greek symbols		*spn*	suspended
α	thermal diffusivity, m^2/s	*thm*	thermal
β	thermal expansion coefficient, 1/K	*top*	top
γ	weighting factor	*tot*	total
δ	thickness or distance, m	*ver*	vertical
ε	emissivity	*wal*	wall
η	efficiency	*wat*	water
μ	uncertainty		
θ	$T-T_{ind,m}$, ^oC		
$\tilde{\theta}$	harmonic temperature oscillation, ^oC		**Superscript**
ν	kinematic viscosity of air, m^2/s	’	per unit length
ρ	density, kg/m^3	”’	per unit area per unit length
σ	Stefan Boltzmann constant, W/m^2K^4	*”	dimensionless form per unit area
φ	density of pipe layout, m/m^2	*	dimensionless form
ϕ	form factor		
ψ	stream function		
ω	vorticity		

ABSTRACT

Kim, Janghyun. Ph.D., Purdue University, December 2016. Evaluating the Performance of Passive Chilled Beams with Respect to Energy Efficiency and Thermal Comfort. Major Professors: James E. Braun and Athanasios Tzempelikos, School of Mechanical Engineering.

Existing modeling approaches for passive chilled beams determined from tests on individual chilled beams in a laboratory are not adequate for assessing overall energy usage and occupant comfort within building simulation programs. In addition, design guidelines for passive chilled beam systems are needed for identifying appropriate applications and optimal configurations. This thesis includes (i) extensive experimental studies for characterizing the performance of passive chilled beams, in both laboratory settings and in field studies, (ii) development of passive chilled beam performance prediction models, (iii) integration of these models into building simulation models/tools and (iv) use of building simulation for overall assessment of different passive chilled beam system configurations in different climates in order to provide guidelines for appropriate applications.

Experiments were conducted with a single passive chilled beam in a laboratory setting and with multiple passive chilled beams installed in a real occupied office space. Based on the experimental results, models that can predict total cooling capacity and chilled surface temperature of passive chilled beams were developed. These models use essential operating conditions of the system and thermal conditions in the environment as inputs and are able to predict the energy and thermal comfort performances of the passive chilled beam system when integrated into a system simulation. The validity of using a model developed from laboratory tests on a single passive chilled beam in a system simulation for spaces with multiple chilled beams was evaluated. Comparison of

laboratory and field measurements indicates that the conventional method of predicting total cooling capacity of a passive chilled beam from laboratory measurements underestimates its performance when installed in a system. These differences could have an important impact on system sizing and commissioning.

Side-by-side field measurements were conducted to compare energy and comfort performance of a passive chilled beam system against constant and variable air volume systems for nearly identical office spaces. While maintaining very similar thermal comfort levels in the two offices, the passive chilled beam system led to a 57% reduction in electric energy compared to the constant air volume system. However, the variable air volume (VAV) system consumed 21% less energy compared to the passive chilled beam system during the field measurements. This is mostly because of the current configuration of the passive chilled beam system which represents the worst case scenario in terms of system configuration. The parallel air system used in the field measurement is a typical air system including the outdoor air and return air damper system. As a starting point followed by various configurations assessment with computer simulations, the return air damper was closed during the entire field measurements of the passive chilled beam system. In order to consider more realistic energy savings compared to VAV systems, alternative passive chilled beam configurations were evaluated using a system simulation model that was validated with the available measurements.

The integrated simulation tool was developed and validated for the case study office space and was then used to perform comprehensive comparisons of alternative passive chilled beam and conventional systems in order to evaluate savings potential in various climatic zones. While maintaining the same thermal environments in spaces, the best passive chilled beam configuration provided electrical energy savings up to 24% for hot and humid climates and up to 35% savings for hot and dry climates compared to a variable air volume system.

The radiation cooling effects of passive chilled beams were also analyzed through experiments and simulations. Both experiments and computer simulations revealed that the effect of the radiation cooling of passive chilled beams is not significant in terms of energy savings and thermal comfort improvement. Based on simulation results covering

various passive chilled beam system configurations and climatic zones, the percentage of radiation cooling energy relative to total passive chilled beam cooling energy varied between 7 to 15%.

CHAPTER 1. INTRODUCTION

1.1. Background

Reducing energy consumption in buildings is an important part of reducing global energy usage and environmental impact. It has been reported by the International Energy Agency (IEA) [1] that residential and commercial buildings account for approximately 32% of global energy use and over 30% of global CO_2 emission. Furthermore, it is predicted that the global energy demand in buildings will increase more than 100% by the year 2050 compared to 2007 due to the "expected increase of number of households, service building area, higher ownership rates for existing energy consuming devices and demand for new types of energy services in response to the expanding global population". More than half of existing buildings are expected to remain for several decades. Therefore, significantly reducing energy use in the building sector requires stringent energy saving requirements for new buildings and retrofitting existing buildings with advanced technologies. In commercial buildings, improvements to both the building envelope and HVAC systems are critical in achieving the ETP scenarios of IEA [1] which is to reduce carbon emission level to limit the global temperature increase. Furthermore, modeling these technologies and analyzing their energy impact are critical parts of assessing their economics towards realizing success in the marketplace.

Radiant heating and cooling systems provide opportunities for improving thermal comfort while potentially reducing energy use. While radiant heating has been successful worldwide, radiant cooling is only popular in northern Europe and has recently been introduced in other continents and countries. A radiant cooling system is defined as "any system where surrounding surface temperatures are lowered to remove sensible thermal loads from a conditioned space and its occupants, thus providing (or contributing to) thermal comfort" or "sensible cooling system provides more than 50% of the total heat

flux by thermal radiation“[2]–[4]. Typically, any latent load requirements are handled separately for a radiant cooling system using a dedicated outdoor air system (DOAS) that conditions only the ventilation air. Compared to conventional all-air systems, this can lead to reduced overall cooling requirements; a significant benefit of the radiant cooling systems. Since the amount of air carried to the space can be reduced significantly, there is also less fan energy consumption compared to conventional systems. Furthermore, the reduction of air flow allows downsized ductwork.

The cooling load can be further reduced by taking advantage of the improved comfort associated with radiant cooling of occupants, which can allow a somewhat higher zone temperature for the same comfort level. Furthermore, higher radiant surface temperatures (needed to stay above the dew point of the air) lead to higher operating temperatures than those of conventional cooling systems, and improved energy efficiency for chillers. It is also possible to couple the radiant cooling system with energy storage within the building thermal mass, to allow load shifting and reductions in peak load [3].

Compared to alternative technologies, radiant cooling systems have been projected to have relative economic benefit according to simple payback calculations with significant energy savings potential [5] as shown in Figure 1-1. In this figure, technical energy savings potential is defined as “the annual energy savings that would occur relative to typical new equipment if the technology option was immediately installed as components / equipment / systems / practices in all reasonable applications”. The simple payback is defined as “the cost of energy savings afforded by the technology divided by the incremental premium of the energy efficiency measure”, where the incremental premium is calculated as cost difference between original and new technology.

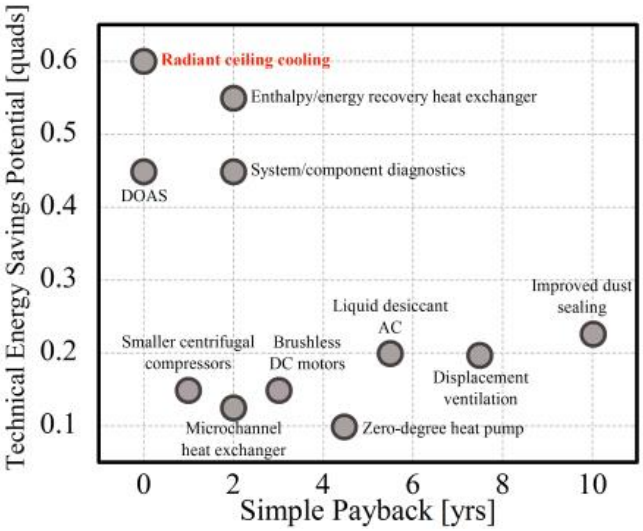

Figure 1-1. Estimated energy savings potential and payback for different technologies [5].

In addition to these benefits, there are some synergies that can be achieved through coupling with other energy savings approaches and technologies. For example, the use of warmer operating temperature provides opportunities for use of a broad range of cooling sources such as ground water, municipal water, storm water retention, night-sky radiant cooling and roof-spray evaporative cooling. The radiant cooling system can also enable performance improvement opportunities for a parallel ventilation system. For example, it can extend the use of natural ventilation when employing an appropriate control strategy. Alternatively, a DOAS employed with radiant cooling can be implemented as displacement ventilation (DV) with underfloor air distribution (UFAD) to provide improved indoor air quality. For this type of implementation, a dropped ceiling can be removed, leading to downsized duct work and reduced fan energy. Furthermore, the thermal decay of the UFAD system can be reduced by direct radiation heat transfer between the chilled ceiling and floor surfaces.

1.2. Passive Chilled Beam

A passive chilled beam is one type of cooling systems that is commercially available. They are widely used in northern Europe and have been recently introduced in North America. A typical passive chilled beam has similar geometry to a fin and tube heat

exchanger. Although several suggestions and ideas have been proposed for different chilled beam types (such as having a wavy fin pattern), the most common type of chilled beam uses square vertical fins along the water pipe as shown in Figure 1-2. To increase radiation effects, a horizontal and perforated panel may be attached at the bottom (under the fin and tube array). Copper and aluminum are used for the water pipes and fins.

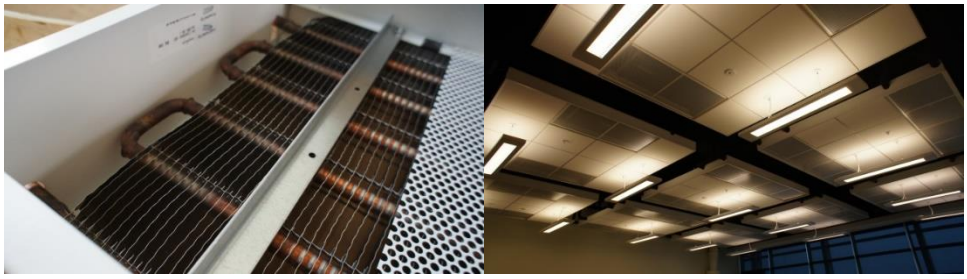

Figure 1-2. Passive chilled beam and perforated panel.

The passive chilled beam is basically a heat exchanger driven by natural convection. As shown in Figure 1-3, it causes natural air circulation by cooling the air at the ceiling level, while the bottom perforated panel usually stabilizes the flow and increases heat extraction by radiation. Chilled beams have higher heat transfer rates per unit face area compared to the ceiling panel type, and they do not need to be installed over the entire ceiling area. Yet, the optimum location of the chilled beams needs to be carefully determined according to space geometry, occupied areas and window positions, since it will affect both the cooling performance and thermal comfort in the space. Useful resources include performance characteristics (i.e., cooling capacity) as a function of beam dimensions and temperature of air and water provided by a few manufacturers. Table 1-1 presents a performance map summary, showing how each dependent variable (such as cooling capacity, air velocity and pressure drop) can be predicted from related independent variables [6]–[9]. The table also shows fixed variables for mapping the cooling capacity and presents the availability of correction factors for a certain range of fixed variables. Typical operating range of chilled water temperature and water mass flow rate through the passive chilled beam is between 14-18^{o}C and 0.02-0.2 kg/s, respectively. The performance of the passive chilled beam can be controlled by these two operating

conditions and its actual cooling capacity will also vary depending on the indoor space conditions such as air temperature, surface temperatures and air movements around the unit.

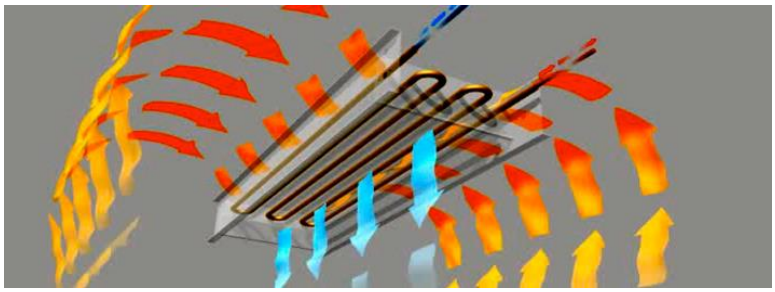

Figure 1-3. Natural air circulation with a passive chilled beam [9].

Table 1-1. Performance maps of passive chilled beams.

Manufacturer	Cooling capacity			Air velocity[1]	Pressure drop	Testing standard
	Independent variables	Fixed variables	Correction factor	Independent variables	Independent variables	
Fläkt Woods	$T_{ind}-T_{wat,m}$ W_{chb},~~H~~$_{chb}$	$\dot{q}_{wat}=0.05$ l/s	$\dot{q}_{wat}$ (0.025-0.2 l/s)	H_{ver} $\dot{Q}'$ W_{chb} H_{chb}	$\dot{q}_{wat}$ W_{chb} H_{chb} L_{coi}	Method V (Future Nordtest)
	W_{chb},~~H~~$_{chb}$,~~L~~$_{chb}$	$\dot{q}_{wat}=0.05$ l/s $T_{ind}-T_{wat,m}$ $=8℃$	N/A			
Halton	$T_{ind}-T_{wat,m}$ W_{chb},~~H~~$_{chb}$	$\dot{m}_{wat}=0.08$ kg/s	$\dot{m}_{wat}$ (0.015-0.08kg/s)	N/A	N/A	N/A
Price	$T_{ind}-T_{wat,m}$ W_{chb},~~L~~$_{chb}$	$\dot{q}_{wat}=0.06$ l/s	N/A	N/A	W_{chb} L_{chb} .	EN Standard 14518
TROX USA	$T_{ind}-T_{wat,m}$ W_{chb},~~H~~$_{chb}$, L_{chb}	$\dot{q}_{wat}=0.03$ l/s $fo=50\%$ $\frac{H_{spn}}{W_{chb}}=0.5$	$\dot{q}_{wat}$. (0.01-0.1 l/s) H_{spn}/W_{chb} (0.1-1)	$\dot{Q}'$	$\dot{q}_{wat}$ W_{chb}	DIN 4715
	fo H_{spn}/W_{chb}, H_{chb}	$T_{ind}-T_{wat,m}$	N/A			

[1] Values are valid for a space without external influences such as heating source and forced air movements

1.3. Scope and Objectives

The approaches used by passive chilled beam manufacturers to map performance are reasonable for sizing chilled beams for a particular application but are not adequate for incorporation in building simulation tools to enable assessments of overall energy usage and occupant comfort. In addition, design guidelines for passive chilled beam systems are needed for identifying appropriate applications and optimal configurations. This work will develop improved passive chilled beam testing and semi-empirical modeling that will allow performance measurements from tests on a single chilled beam in a laboratory setting to be used in modeling multiple chilled beams in a building application within a building simulation tool. The research includes characterizing the performance of passive chilled beams by experimental investigations and development of models, and integration of these models into building simulation models for overall assessments of passive chilled beam systems. The integrated simulation tool will be used to perform comprehensive comparisons of passive chilled beam and conventional systems in order to provide guidelines for appropriate applications. The objectives of this research are the following and these are also shown in Figure 1-4 in a sequential order:

1. Characterizing the performance of passive chilled beam system: A single passive chilled beam is tested in a controlled environment to measure performance as a function of basic parameters and investigate convection and radiation heat transfer mechanisms with various operating conditions. A semi-empirical passive chilled beam model, able to provide sufficient outputs for analyzing the effect on energy efficiency and thermal comfort, is developed based on experimental measurements. In order to verify the validity of using the model developed for an individual passive chilled beam from experiments in an integrated system simulation, in-situ field measurements with multiple passive chilled beams installed in an actual occupied office environment is performed to use as a basis of verification. After characterizing the performance of a single passive chilled beam, a system level of comparison is conducted by a side-by-side field measurement between an office with the conventional air system and an office with the passive chilled beam system for two months during the summer season in West Lafayette,

Indiana. The purpose of this experiment is to provide realistic basis of the relative performance between different systems. Additional experiment to quantify the effect of radiation cooling of passive chilled beams is conducted as well.

2. Integrated model development and overall and relative assessment of passive chilled beam systems using building simulation: The passive chilled beam model is integrated with a zone thermal model, including envelope and HVAC systems, to evaluate the energy and comfort performance of passive chilled beams in commercial buildings. Using the integrated model, the passive chilled beam system is compared with conventional air systems to estimate potential benefits in terms of energy efficiency and thermal comfort. Full-scale experiments in open plan offices will be used to validate these results. Finally, the results will be used to develop design guidelines for passive chilled beam systems.

1.4. Document Overview

Chapter 2 presents a detailed literature review on modeling approaches for passive ceiling cooling systems. The different models are categorized into passive ceiling coolers (2.3.1), indoor environment models (2.3.2), and integrated models (2.3.3). The limitations of these models are summarized in section 2.3.4. Passive chilled beams are discussed in section 2.4 with extensions to integrated building simulation models.
Chapter 3 presents the methods used to characterize the performance of the passive chilled beam at the component level. The experiment of the passive chilled beam in a laboratory setting is presented in 3.1.1. Similarly, the experiment of multiple chilled beams in a real occupied office is presented in 3.1.2. The semi-empirical models for passive chilled beams are discussed in section 3.2. The contents of Chapter 3 focus only on the passive chilled beam which is a part of the first research objective shown in 1.3.
Chapter 4 presents the experimental investigation and modeling of the conventional air system and the passive chilled beam system. A side-by-side experiments, shown in section 4.1, are first conducted in two offices next to each other while one of the offices is conditioned with a conventional air system and the other office conditioned with the

passive chilled beam system. An integrated building simulation model is developed in section 4.2. A validation of this integrated building simulation model is performed by comparing the results against the side-by-side experimental results. The contents of Chapter 4 focus more on the system level partially covering both first and second research objectives shown in section 1.3.

Chapter 5 presents the overall and relative assessment of the passive chilled beam system using the whole building energy simulation tool. Relative potentials of the passive chilled beam system compared to the conventional air system under different climates and with different configurations are analyzed in 1.1. The contents of Chapter 5 cover a part of the second research objectives shown in section 1.3.

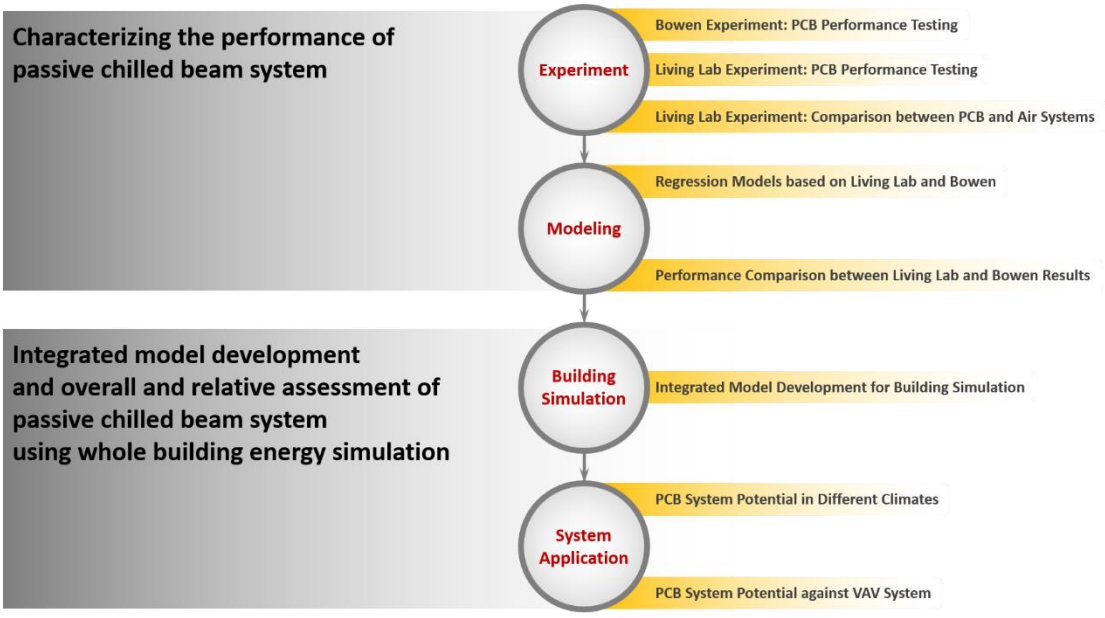

Figure 1-4. Flowchart of research.

CHAPTER 2. LITERATURE REVIEW AND RESEARCH GAPS

2.1. Radiant Cooling Systems

There is a series of studies [2], [3], [10]–[12] on radiant cooling system by Center for the Built Environment (CBE) and several standards and handbook [13]–[19] that provide design guidelines for radiant cooling systems. The initial study [3] from CBE starts with defining the scope of radiant cooling system research and the remaining studies address each objective that was outlined in the scoping study. Although these studies and standards cover a lot of portions of principles of radiant cooling systems, there are still gaps that need to be filled to provide practical design and operational guidelines for each specific type of radiant cooling technologies. The proposed objectives in the radiant cooling research scoping study are “design and simulation tools, applications in actual buildings, synergies with other strategies and building systems and climate-related limitations for North America”. The specific problems addressed and their solutions depend on the type of radiant cooling system such as ceiling panel system, in-slab embedded system, and, especially, passive chilled beam system.

2.2. Passive Ceiling Cooling Systems

There are generally three types of passive ceiling cooling system configurations depending on their installation and operation type. These are presented in the following subsections.

2.2.1. Ceiling Panel Type

As shown in Figure 2-1, a water U-shaped pipe is mechanically bonded over a horizontal panel in ceiling panel configurations. The water pipe and horizontal panel work as thermally conducting devices and are generally made of copper and aluminum,

respectively, to minimize temperature variation along the surface that faces the room interior. Based on previous studies, the ceiling panel system is usually installed over the entire ceiling surface, however it is equally divided into several sections (which are then called ceiling panels) as shown in Figure 2-1 to provide easier installation and maintenance. The bottom (chilled) surface which is cooled by the flow of chilled water through the tubes induces both convection and radiation heat extraction from the space. Since radiant ceiling panels have been extensively studied, there are various modeling techniques available in literature.

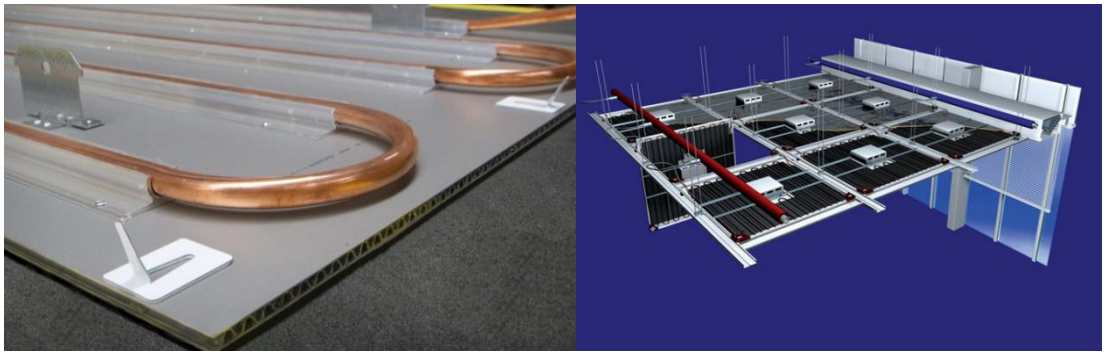

Figure 2-1. Ceiling panel type [20], [21].

2.2.2. In-slab Embedded Type

The embedded ceiling cooling type is similar to a radiant floor system. As shown in Figure 2-2, the water pipes are embedded in a solid material (usually concrete). Typically, the thermal response of an embedded radiant ceiling type is slower than that of the other two configurations because of the high thermal capacitance of concrete. However, high thermal mass can also delay the peak load, which is often desirable. The system's way of extracting heat from a space is similar to that of ceiling panels. This type of radiant cooling is more complex in terms of a retrofit compared to the other types. Recent studies of the embedded type include a multi-story building with radiant slabs between floors that can work either as radiant floors for heating or radiant ceilings for cooling [22].

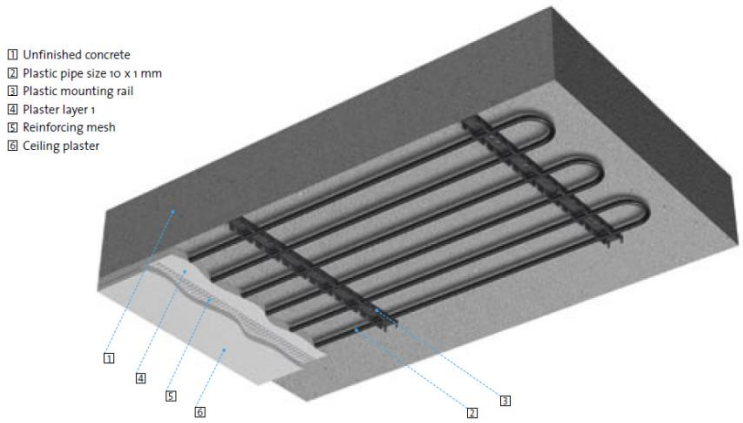

Figure 2-2. In-slab embedded type [21].

2.2.3. Passive Chilled Beam Type

Passive chilled beams are slightly different from a radiant system by its strict definition. However, since it involves radiation heat transfer with indoor surfaces through its chilled surface panel, it can be considered as a system having radiant heat transfer capability. In the radiant cooling research scoping study [3], passive chilled beams are included as one of the radiant (ceiling) panel systems. However, there are significant differences between typical radiant ceiling panels and passive chilled beams, due to the convection and radiation cooling mechanisms, leading to different installation and operation. There is also an active type of chilled beam where an air duct and nozzles are incorporated in a chilled beam unit. Active chilled beams mostly rely on forced air movement, which makes them less effective in terms of radiant capability. Passive chilled beam have approximately a mix of convective and radiative heat transfer and can be categorized as lying somewhere between active chilled beam (mostly convection) and radiant ceiling panel (50% or more of radiation). Application and design guidelines for chilled beam systems can be found in several books [23]–[25] published from the American Society of Heating, Refrigeration, and Air-Conditioning Engineers (ASHRAE) and the Federation of European Heating, Ventilation and Air Conditioning Associations (REHVA). These guidebooks mostly provide previous findings and know-how obtained from major chilled beam manufacturers. Though they provide useful and practical information for chilled beam systems, they do not provide recommendations on maximizing system performance

in terms of energy efficiency and thermal comfort. Moreover, there are no detailed models available for passive chilled beams.

2.3. Modeling Passive Ceiling Cooling Systems [26]

Various studies of radiant ceiling cooling systems have been conducted within the past two decades. Models of different scope, focus, scale, resolution and complexity have been developed to predict energy use and thermal comfort effects. In this section, the models are categorized as: “passive ceiling cooler”, “indoor environment” or “integrated” models in terms of the domain of interest as shown in Figure 2-3. Then each domain type was categorized as “simplified”, “detailed”, “empirical” and “black box” in terms of the modeling approach. Table 2-1 shows the entire list of models in this section within this classification (plus the configuration type), and they are listed with the same order as they are presented in the following sections. Studies that focused solely on experimental work about system design or application [27]–[34], although useful, are not discussed since the focus of this section is on modeling methods for radiant ceiling cooling systems.

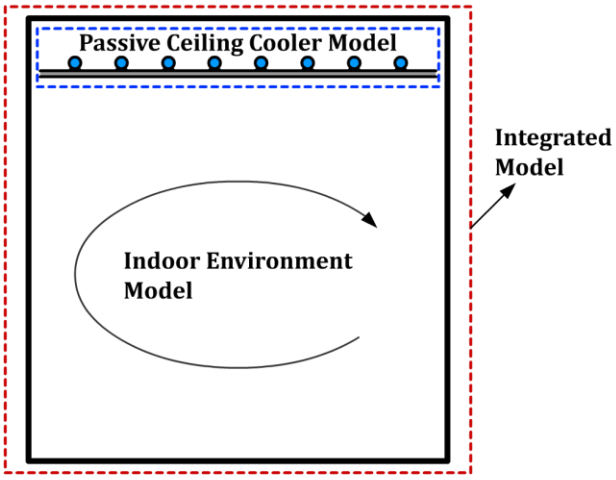

Figure 2-3. Domain of interests in models.

2.3.1. Passive Ceiling Cooler Models

Passive ceiling cooler models focus on the ceiling cooling system itself with minimum interactions with the indoor environment. In these models, system configurations such as

Table 2-1. Summary of model classification.

Domain Type	Modeling Approach	Configuration Type	Author (or company)	Model #
Passive ceiling cooler (section 2.3.1)	simplified	embedded	Kilkis et al.	1
		embedded	Koschenz and Dorer	2
		ceiling panel	Mumma	3
		ceiling panel	Tian	4
		ceiling panel, embedded	Strand et al.	5
		embedded	Weber and Johannesson	6
		ceiling panel	Okamoto et al.	7
		passive chilled beam	Halton	8
	detailed	embedded	Antonopoulos	9
		ceiling panel	Tye-Gingras and Gosselin	10
Indoor environment (section 2.3.2)	simplified	ceiling panel, embedded	Castillo and Tovar	11
	detailed	ceiling panel, embedded	Rees and Haves	12
		ceiling panel, embedded	Ben Nasr et al.	13
		ceiling panel, embedded	Ayoub et al.	14
		ceiling panel, embedded	Kim et al.	15
		ceiling panel, embedded	Catalina et al.	16
		ceiling panel, embedded	Corgnati et al.	17
		ceiling panel, embedded	Karadag	18
		ceiling panel, embedded	Taki et al.	19
		ceiling panel, embedded	Chiang et al.	20
	empirical	ceiling panel, embedded	Novoselac et al.	21
		ceiling panel, embedded	Causone et al.	22
		ceiling panel, embedded	Andrés-Chicote et al.	23
Integrated (section 2.3.3)	simplified	ceiling panel, embedded	Diaz	24
	detailed	ceiling panel	Niu	25
		ceiling panel, embedded	Stetiu et al.	26
	black box	embedded	Ferkl and Siroky	27
		ceiling panel	Ge et al.	28

inlet/outlet water temperatures, average panel surface temperature and system geometry are all parameters to be considered. Either the inlet air conditions to the cooler are specified or the indoor environmental parameters are assumed as fully mixed conditions. Passive ceiling cooler models can be divided into simplified (lumped control volumes) and detailed (discretized analysis) as described below.

2.3.1.1. Simplified Models

The advantage of using simplified models is that they provide simple and computationally efficient approaches that can capture the most important physics of the device. Since the ceiling cooling system is just one of the components of the entire environmental control system, the use of such simplified and faster models will provide significant improvement in terms of computational effort in whole building simulation. Most of the simplified models that have been developed are quasi-steady representations that do not consider any energy storage within the passive ceiling cooler. Therefore, it is important to verify whether these models coupled to building models can appropriately represent the dynamics of integrated systems.

Kilkis et al. [35] developed a model of an embedded type for both ceiling cooling and floor heating. To predict the cooling capacity of the system, convection and radiation heat transfer coefficients, area-weighted uncooled surface temperature (*AUST*) and temperature difference between the uniformly assumed panel (or ceiling surface) surface temperature ($T_{pan,m}$) and fully mixed temperature ($T_{ind,m}$) of the zone were used. Several correlations were adopted for the heat transfer coefficients and *AUST*. The cooling capacity was calculated as the sum of convective and radiative heat flux where the opposite side of the indoor space is assumed perfectly insulated:

$$\dot{Q}''_{cap} = \dot{Q}''_{rad} + \dot{Q}''_{con} = h_{rad}(T_{pan,m} - AUST) + h_{con}(T_{pan,m} - T_{ind,m}) \quad (2.1)$$

In the above equation, the radiation and convective heat transfer coefficients depend on physical parameters such as surface characteristics, room geometry and indoor temperatures according to:

$$h_{rad} = C \cdot r \cdot \sigma \quad (2.2)$$

$$h_{con} \cong (1 - 2.22\times10^{-5} alt)^{2.627} \cdot (4.96/(4A_{flr}/P_{flr}))^{0.08} \cdot 2.67\left|T_{pan,m} - T_{ind,m}\right|^{0.25} \quad (2.3)$$

where parameters C and r are calculated from:

$$C \cong e \qquad (A_{pan}/A_{ind} \le 0.3) \quad (2.4)$$

$$r \cong \left\{0.9659 + 0.00495\left(T_{pan,m} - 10\right)\right\}\times10^{8} \qquad (10^{\circ}\mathrm{C} \le (T_{pan,m} + AUST)/2 \le 18^{\circ}\mathrm{C}) \quad (2.5)$$

The average temperature (*AUST*) in Eq. (2.1) is equal to:

$$AUST = T_{ind,m} - pi \cdot z \tag{2.6}$$

where:

$$z = 7/(T_{out} - 45) \quad (26^{\circ}\mathrm{C} \le T_{out}/2 \le 36^{\circ}\mathrm{C}) \tag{2.7}$$

Eq. (2.2) and Eq. (2.4)-(2.7) are based on previous studies [36], [37]. Eq. (2.3) was adopted from a well-known study [38] which is used widely for computing the natural convection heat transfer coefficient. Analytical steady state fin model theory was used to derive an equation for mean water temperature ($T_{wat,m}$) in a water pipe of the embedded type to represent a relationship between $T_{pan,m}$ and $T_{wat,m}$. A schematic description with relevant parameters is shown in Figure 2-4. To derive an equation for water mean temperature, an energy balance was first applied to derive relevant equations.

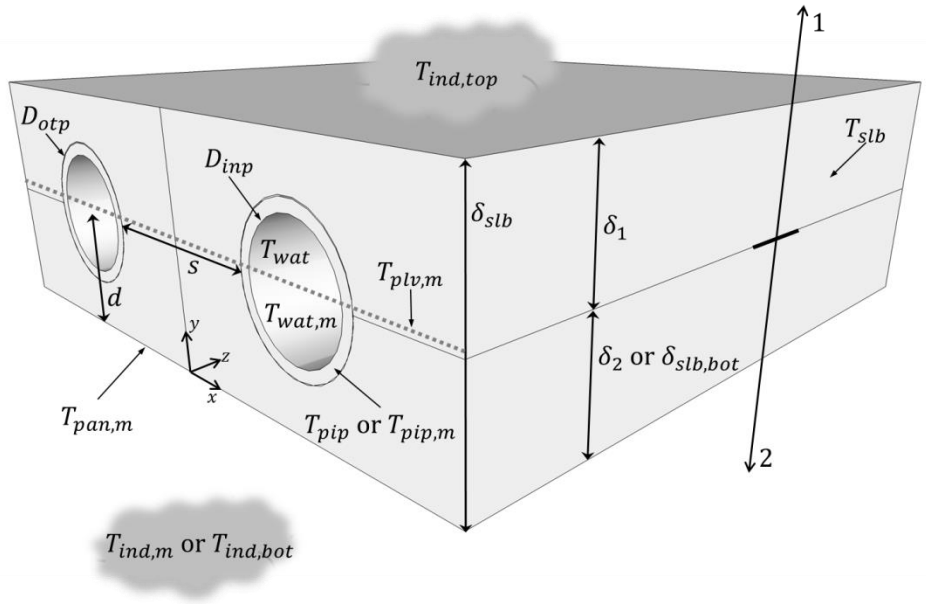

Figure 2-4. Parameters related to in-slab embedded type.

$$\left[2s\eta_{fin} + D_{otp}\right] h_{rad}(T_{pan,\max} - AUST) + \left[2s\eta_{fin} + D_{otp}\right] h_{con}(T_{pan,\max} - T_{ind,m}) = \dot{Q}''_{cap}(s + D_{otp}) \tag{2.8}$$

The left hand side of Eq. (2.8) includes a temperature difference based on maximum surface temperature ($T_{pan,max}$) of the radiant surface with a fin efficiency parameter (η_{fin}). From Eq. (2.8), $T_{pan,max}$ can first be rearranged as shown below.

$$T_{pan,max} = \frac{\dot{Q}''_{cap}(s + D_{otp}) + \left[2s\eta_{fin} + D_{otp}\right] h_{rad} AUST + \left[2s\eta_{fin} + D_{otp}\right] h_{con} T_{ind,m}}{\left[2s\eta_{fin} + D_{otp}\right] h_{rad} + \left[2s\eta_{fin} + D_{otp}\right] h_{con}} \quad (2.9)$$

Surface temperature of the pipe ($T_{pip,m}$) can then be formulated based on an energy balance:

$$T_{pip,m} = T_{pan,\max} + \dot{Q}''_{cap}\left[R_{cov} + \left(\delta_{slb,bot} - \frac{D_{otp}}{2}\right) \Big/ k_{slb}\right] \quad (2.10)$$

R_{cov} in the above equation can be used when there is additional surface cover under the radiant surface. The final form of the water temperature equation can then be derived:

$$T_{wat,m} = \frac{\dot{Q}''_{cap} \cdot (s + D_{otp})}{\eta_{thm} \cdot \pi}\left[\frac{1}{h_{wat} D_{inp}} + \frac{1}{2k_{pip}} + \frac{R_{slb}}{D_{otp}}\right] + T_{pip,m} \quad (2.11)$$

where:

$$h_{wat} \cong 1056\left[0.02(T_{wat,m} + 273) - 4.06\right] \frac{v_{wat}^{0.8}}{D_{inp}^{0.2}} \quad (2.12)$$

$$\eta_{thm} = \frac{\dot{Q}_{cap}}{\dot{Q}_{cap} + \dot{Q}''_{top} A_{pan}} \quad (2.13)$$

Eq. (2.12) is adopted from [39]. The final goal of this model is to calculate the required water temperature to remove a certain load from a space. Additionally, the study also provides a way (sinusoidal approximation) to predict the variation of radiant surface temperature along the distance between water pipes. The model was validated by comparing the model results against the ANSYS finite element package [40]. Geometric parameters of the embedded system, design conditions of the space and thermal loads required to maintain the design conditions were given to calculate required radiant surface temperature, pipe surface temperature and water temperature. The modeling results showed good agreement with the numerical results from ANSYS.

Koschenz and Dorer [41] developed a model of embedded ceiling cooling systems which can be integrated within whole building simulation programs. The main feature of this model is that it introduces a form factor (ϕ), which acts as a correction factor in order to compensate for the conversion from a 2-dimensional to a 1-dimensional problem. For example, in a hydronic slab system, water temperature will vary as it flows through the

horizontal tube due to heat transfer with slab material. By using the form factor this variation of water temperature can be converted to a single representative mean value, thus, removing one dimension from the original problem. A formulation that uses form factor was introduced by Glück [42], [43] and can be derived from partial differential equations for heat conduction. The net heat flux to the slab from the top and bottom is expressed as:

$$\dot{Q}''_{cap} = U_{top}(T_{plv,m} - T_{ind,top}) + U_{bot}(T_{plv,m} - T_{ind,bot}) = \phi\left[U_{top}(T_{wat,m} - T_{ind,top}) + U_{bot}(T_{wat,m} - T_{ind,bot})\right] \quad (2.14)$$

The model characterizes the performance of an embedded type system in a multi-story building, thus, including both upper ($T_{ind,top}$) and lower ($T_{ind,bot}$) space fully mixed air temperatures as shown in Figure 2-4. In the above equation, $T_{plv,m}$ is defined as a mean slab temperature at pipe level. Also, U is defined as the overall heat transfer coefficient, which combines conduction within the slab material and convection between indoor air and the slab surface. By substituting a formula for form factor into Eq. (2.14), the heat flux can also be expressed in terms of the difference between the mean water and pipe level slab temperatures.

$$\dot{Q}''_{cap} = \frac{2\pi k_{slb}}{(s + D_{otp})\left[\ln\left(\frac{s + D_{otp}}{\pi D_{otp}}\right) + \sum_{j=1}^{\infty}\frac{g_1(j) + g_2(j)}{j}\right]}\left(T_{wat,m} - T_{plv,m}\right) \quad (2.15)$$

where:

$$g_k(j) = \frac{\dfrac{h_k(s + D_{otp})/k_{slb} + 2\pi j}{h_k(s + D_{otp})/k_{slb} - 2\pi j}e^{-\frac{4\pi j}{(s+D_{otp})}\delta_{3-k}} - e^{-\frac{4\pi j}{(s+D_{otp})}(\delta_1+\delta_2)}}{e^{-\frac{4\pi j}{(s+D_{otp})}(\delta_1+\delta_2)} - \left(\dfrac{h_1(s + D_{otp})/k_{slb} + 2\pi j}{h_1(s + D_{otp})/k_{slb} - 2\pi j}\right)\left(\dfrac{h_2(s + D_{otp})/k_{slb} + 2\pi j}{h_2(s + D_{otp})/k_{slb} - 2\pi j}\right)} \quad (2.16)$$

In Eq. (2.16), the index k refers to the top or bottom section (sections divided by the horizontal centerline of water pipe level as shown in Figure 2-4). Thus, h_1 is the convection heat transfer coefficient between the air and the top surface of the embedded system and h_2 is the coefficient between the air and the bottom surface. The model requires specification of the convection coefficients. The model was compared with finite element analysis software and was implemented in TRNSYS to calculate the transient response of an indoor space with an embedded type system. By applying geometrical

parameters of the embedded system and air and water conditions such as heat transfer coefficients and water temperature, the model calculates $T_{plv,m}$. Then, $T_{plv,m}$ is used as the temperature of a virtual surface at the pipe level to provide the same heat transfer rate to the indoor space. Although Eq. (2.15) should include actual transient behavior of the ceiling cooling system, it was formulated without time-dependent variables, based on the fact that steady state conditions can be reached within an hour. Consequently, the modeling and finite element analysis results showed good agreement in hourly time-step simulation. Currently, this model is implemented in TRNSYS as "Thermo-active building element".

A series of related studies [44]–[47] concentrate on the ceiling panel type shown in Figure 2-5. Their method of formulating the analytical model uses a similar approach to Kilkis et al. [35], but also includes better characterization of the ceiling panel geometry by considering heat transfer on both bottom (the room) and top (usually a plenum) sides of the panel. Furthermore, the study developed a simple linear correlation of cooling capacity estimation with significant parameters for practical applications. The studies also cover the effect of a cooling system operating with different ventilation systems such as dedicated outdoor air systems (DOAS) [44].

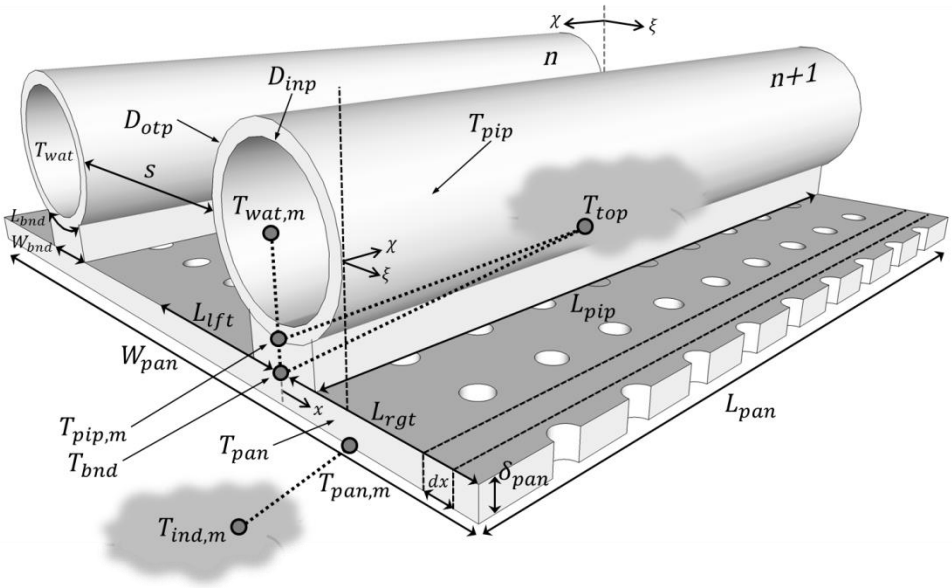

Figure 2-5. Parameters related to ceiling panel type.

The air-side equations to calculate the cooling capacity are listed below:

$$\dot{Q}''_{cap} = U(T_{ind,m} - T_{pan,m}) = (\dot{Q}''_{con} + \dot{Q}''_{rad})_{bot} + (\dot{Q}''_{con} + \dot{Q}''_{rad})_{top} \quad (2.17)$$

where the convection and radiation terms for the bottom and top side are given by:

$$\dot{Q}''_{con,bot} = h_{con,bot}(T_{ind,m} - T_{pan,m}) \quad (2.18)$$

$$\dot{Q}''_{rad,bot} = h_{rad,bot}(AUST - T_{pan,m}) \quad (2.19)$$

$$\dot{Q}''_{con,top} = h_{con,top}(T_{ind,m} - T_{pan,m}) \quad (2.20)$$

$$\dot{Q}''_{rad,top} = h_{rad,top}(T_{ind,m} - T_{pan,m}) \quad (2.21)$$

Similar to [35], Mumma's model also uses *AUST* as a basis of radiation heat transfer as shown in Eq. (2.19). However, since the temperature difference between plenum surfaces will be less significant compared to the indoor space, the top side radiation was formulated based on $T_{ind,m}$. The convection and radiation heat transfer coefficients are calculated using Eqs. (2.22)-(2.25).

$$h_{con,bot} = FC_{con,bot} + 2.13(T_{ind,m} - T_{pan,m})^{0.31} \quad (2.22)$$

$$h_{rad,bot} = 5\times10^{-8}\left[(AUST+273)^2 + (T_{pan,m}+273)^2\right]\left[(AUST+273) + (T_{pan,m}+273)\right] \quad (2.23)$$

$$h_{con,top} = FC_{con,top} + 0.134(T_{ind,m} - T_{pan,m})^{0.25} \quad (2.24)$$

$$h_{rad,top} = 4.8\times10^{-8}\left[(T_{ind,m}+273)^2 + (T_{pan,m}+273)^2\right]\left[(T_{ind,m}+273) + (T_{pan,m}+273)\right] \quad (2.25)$$

Eqs. (2.23) and (2.25) were adopted from [4]. While the second terms in the convection coefficient equations in Eqs. (2.22) and (2.24) are based on a well-known previous study [38], the first term which represents the forced convection effect is correlated by introducing a 2^k factorial experiment design method [48]. The final correlation of $FC_{con,bot}$ and $FC_{con,top}$ were formulated with the most significant parameters: temperature difference between panel surface ($T_{pan,m}$) and room air ($T_{ind,m}$), air velocity (V_{air}) and width of nozzle diffuser (W_{dif}) of the ventilation system [46].

The water-side equations are expressed as:

$$T_{pan,m} = T_{wat,i} + \frac{\dot{m}c_p\left(T_{wat,o} - T_{wat,i}\right)}{A_{pan}C_{pan}U}(1 - C_{pan}). \quad (2.26)$$

$$C_{pan} = \frac{\dot{m} c_p \left(T_{wat,o} - T_{wat,i} \right)}{A_{pan} U \left(T_{ind,m} - T_{wat,i} \right)} \tag{2.27}$$

In Eq. (2.27), a panel heat removal factor C_{pan} is defined as a ratio of actual sensible cooling capacity to the maximum possible cooling capacity of the panel. The concept of C_{pan} is the same as that of fin efficiency where the maximum heat transfer rate can be achieved from the assumption of considering a base temperature equal to the fin surface temperature (in this case, radiant surface temperature equal to water inlet temperature). Eqs. (2.26)-(2.27) were formulated based on mass and energy balances for the fin and tube geometry as developed for flat plate solar collectors [49]. The analytical model was used to develop a practical correlation, which can be used directly to calculate cooling capacity of the ceiling cooling panel as a function of the most significant parameters. Eight significant parameters were identified using a fractional factorial design method [48]; the correlation and application range can be found in Jeong and Mumma [47]. The modeling results showed good agreement against manufacturer's data under standard test conditions of DIN 4715.

Tian et al. [50] used the modeling approach by [46] and added correction factors (C_{cap}) for the panel's cooling capacity (Eq. (2.29)) for the case without a ventilation system (effect of forced convection). Also, Eq. (2.28) was used for forced convection on the bottom side of the panel with parameters related to air characteristics around the ceiling panel. Eq. (2.19) was used for bottom and top side radiation. An experiment was performed to obtain C_{cap} as a function of panel-air temperature difference, to improve the accuracy of the cooling capacity under specific operating conditions. The recommended correction factors are shown in Table 2-2.

Table 2-2. Correction factors.

$T_{ind,m} - T_{pan,m}$	C_{cap}
6.3	1.13
7.9	1.23
10	1.25

$$FC_{con,bot} = 0.1656\left[\left(u_{air}W_{pan}\right)/\nu_{air}\right]^{0.63} k_{air}/W_{pan} \tag{2.28}$$

$$\dot{Q}''_{cor} = C_{cap}\cdot\dot{Q}''_{cap} \tag{2.29}$$

Strand, Baumgartner and Pederson [51], [52] described a generic radiant heating and cooling system model which is used in EnergyPlus [53], [54]. The model can represent either a ceiling panel or an embedded type since the "effectiveness NTU" method is used to treat the radiant system as a generic heat exchanger. The model can calculate the actual heat extraction rate by using the "effectiveness NTU" method. The model can be coupled with a building model to determine the ceiling surface temperature along with the convective and radiative heat exchange in the space. The effectiveness NTU equations used in the model are shown below.

$$\dot{Q}_{cap} = \left(\dot{m}c_p\right)_{wat}\left(T_{wat,i} - T_{wat,o}\right) = E\dot{Q}_{max} = E\left(\dot{m}c_p\right)_{wat}\left(T_{wat,i} - T_{pan,m}\right) \tag{2.30}$$

where:

$$E = 1 - e^{NTU} \tag{2.31}$$

$$NTU = \frac{UA}{\left(\dot{m}c_p\right)_{wat}} \tag{2.32}$$

$$UA = h_{wat}(\pi DL_{chr}) \tag{2.33}$$

In estimating the overall heat transfer coefficient (U), conduction in the water pipe is neglected. In Eq. (2.33), a well-known Colburn equation was used to calculate the water-side heat transfer coefficient (h_{wat}) and total tube length was used for the characteristic length (L_{chr}). When the water conditions (temperature and flow rate) are known, the effectiveness (E) can be calculated. Then, the only unknowns in Eq. (2.30) will be $\dot{Q}_{cap}$, $T_{wat,o}$ and $T_{pan,m}$. These unknowns are coupled and solved with the building model energy balance equations (indoor surface heat balance, outdoor surface heat balance and indoor air heat balance). Compared to the other simplified models, this model is relatively difficult to couple with any building simulation program since it requires interaction with building model internal heat balance equations to solve for parameters related to the radiant system. There are several studies [55], [56] which have used this model in whole building simulation.

Weber and Jóhannesson [57] presented another interesting approach of modeling the embedded type system by developing a thermal resistance and capacitance (*RC*) network model in the frequency domain. A simplified geometry which includes nodes of pipe, core, upper and lower space of embedded type cooling system was formulated with both triangular and star RC network models as shown in Figure 2-6. The advantages of both RC network models were verified and compared. The purpose of these model developments was to replace the complexity of previous time-domain models' computing time and instability to frequency-domain models with adequate computing efficiency and accuracy. The energy balance equations on the embedded system were formulated based on admittance (*E* and *H*) and transmittance (*F* and *G*) between nodes. Admittance is defined as the ratio of heat transfer rate entering the embedded system to temperature oscillation and transmittance is defined as the ratio of heat transfer rate leaving the system to temperature oscillation. Eq. (2.34) and (2.35) show the energy balance equations of the triangular and star RC network, respectively, expressed with matrices. Subscripts 1, 2, 3, *C* and Γ represent node number 1, 2, 3, core node and Γ-link, respectively. Since the equations are expressed in frequency domain, $\tilde{Q}$ denotes harmonic heat transfer rate oscillation (*W*), $\tilde{\theta}$ denotes harmonic temperature oscillation (^{o}C) and coefficient matrix with *E*, *F*, *G* and *H* represents the transfer function between nodes. To solve the star RC network with Eq. (2.35), an analytical solution [58] is adopted between wall and core nodes to calculate heat flux and temperature in the frequency domain first; then the remaining link between core and pipe is solved iteratively. To solve the triangular RC network with Eq. (2.34), the transmittance for each link is solved by first neglecting Γ-link. Then, a ω-RC transform [59] is adopted to solve resistances and capacitances in parallel links between nodes. After acquiring all the resistances and capacitances of the entire triangular RC network, initial admittances and transmittances can be calculated. Eq. (2.34) can be finally solved by calculating modified resistances and capacitances of the Γ-links with the assistance of the finite element method's calculation. The calculation results of both models were in good agreement compared to the conventional finite element method's solution. There is also another study which focuses more on the validation of the same model [60].

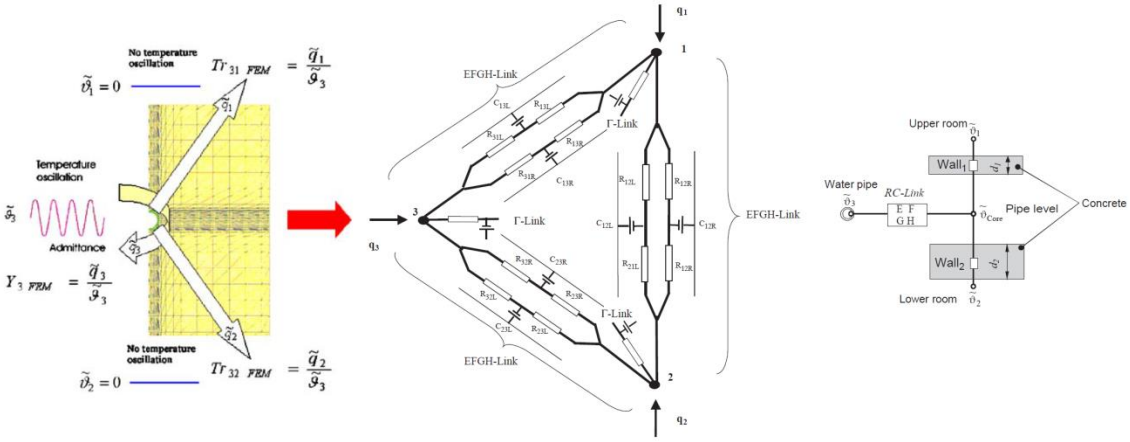

Figure 2-6. Representation of RC network models [57].

$$\begin{pmatrix} \tilde{Q}_1 \\ \tilde{Q}_2 \\ \tilde{Q}_3 \end{pmatrix} = \begin{pmatrix} E_{13}+E_{12}+E_{1\Gamma}+F_{1\Gamma} & F_{12} & F_{13} \\ -G_{12} & E_{23}-H_{12}+E_{2\Gamma}+F_{2\Gamma} & F_{23} \\ -G_{13} & -G_{23} & -H_{23}-H_{13}+E_{3\Gamma}+F_{3\Gamma} \end{pmatrix} \begin{pmatrix} \tilde{\theta}_1 \\ \tilde{\theta}_2 \\ \tilde{\theta}_3 \end{pmatrix} \tag{2.34}$$

$$\begin{pmatrix} \tilde{Q}_1 \\ \tilde{Q}_2 \\ \tilde{Q}_3 \end{pmatrix} = \begin{pmatrix} E_{1C}-\dfrac{F_{1C}G_{1C}}{H_{3C}+H_{2C}+H_{1C}} & -F_{1C}\dfrac{G_{2C}}{H_{3C}+H_{2C}+H_{1C}} & -F_{1C}\dfrac{G_{3C}}{H_{3C}+H_{2C}+H_{1C}} \\ -F_{2C}\dfrac{G_{1C}}{H_{3C}+H_{2C}+H_{1C}} & E_{2C}-\dfrac{F_{2C}G_{2C}}{H_{3C}+H_{2C}+H_{1C}} & -F_{2C}\dfrac{G_{3C}}{H_{3C}+H_{2C}+H_{1C}} \\ -F_{3C}\dfrac{G_{1C}}{H_{3C}+H_{2C}+H_{1C}} & -F_{3C}\dfrac{G_{2C}}{H_{3C}+H_{2C}+H_{1C}} & E_{3C}-\dfrac{F_{3C}G_{3C}}{H_{3C}+H_{2C}+H_{1C}} \end{pmatrix} \begin{pmatrix} \tilde{\theta}_1 \\ \tilde{\theta}_2 \\ \tilde{\theta}_3 \end{pmatrix} \tag{2.35}$$

Okamoto et al. [61], [62] developed a semi-analytical model to predict the performance of ceiling panel cooling systems. The study formulates model equations by starting with an energy balance of an infinitesimal control volume on a cooling panel shown in Figure 2-5. The energy balance equation is defined as:

$$\dot{Q}(x) = \dot{Q}_{top} + \dot{Q}_{bot} + \dot{Q}(x+dx) \tag{2.36}$$

Eq. (2.36) can be expressed as a differential equation as follows:

$$\begin{aligned} & -k_{pan}\delta_{pan}L_{pan}\frac{dT_{pan}}{dx} \\ & = U_{top}L_{pan}dx\left(T_{pan}(x)-T_{ind,m}\right)+U_{bot}L_{pan}dx\left(T_{pan}(x)-T_{ind,m}\right) \\ & -k_{pan}\delta_{pan}L_{pan}\left[\frac{dT_{pan}}{dx}+\frac{d^2T_{pan}}{dx^2}dx\right] \end{aligned} \tag{2.37}$$

U_{top} and U_{bot} are overall heat transfer coefficients at the top and bottom side of the panel surface, respectively, which consider both convection and radiation heat transfer. Eq. (2.37) can be solved as shown in Eq. (2.38) with the following boundary conditions:

$$T_{pan}(x) - T_{ind,m} = \frac{\cosh\left[\sqrt{\frac{U_{bot}+U_{top}}{k_{pan}\delta_{pan}}}\left(x - 1/2\varphi\right)\right]}{\cosh\sqrt{\frac{U_{bot}+U_{top}}{k_{pan}\delta_{pan}}}\Big/2\varphi} \cdot T_{pan}(0) \tag{2.38}$$

Boundary conditions:

$$T_{pan}(x=0) = T_{pan}(0) \tag{2.39}$$

$$\frac{dT_{pan}}{dx}\left(x = \frac{s + D_{otp}}{2}\right) = 0 \tag{2.40}$$

Eq. (2.38) represents the relationship between panel surface ($T_{pan}(x)$) and indoor air temperature ($T_{ind,m}$) including the (currently unknown) parameter $T_{pan}(0)$. φ is the pipe density, which can represent different layouts and is physically defined as the "effective pipe length on panel". Before deriving equations to couple $T_{pan}(0)$ with water temperature ($T_{wat,m}$), the heat transfer rate from the panel surface to indoor air was formulated by integrating the equations of the top and bottom part of the panel, respectively.

$$\dot{Q}_{bot} = 2\cdot\int_0^{1/2\varphi} U_{bot} L_{pip}\left(T_{pan}(x) - T_{ind,m}\right)dx = \frac{2U_{bot}L_{pip}}{\sqrt{\frac{U_{bot}+U_{top}}{k_{pan}\delta_{pan}}}}\left[\frac{e^{\sqrt{\frac{U_{bot}+U_{top}}{k_{pan}\delta_{pan}}}\Big/\phi} - 1}{e^{\sqrt{\frac{U_{bot}+U_{top}}{k_{pan}\delta_{pan}}}\Big/\phi} + 1}\right]\left(T_{pan}(0) - T_{ind,m}\right) \tag{2.41}$$

$$\dot{Q}_{top} = 2\cdot\int_0^{1/2\varphi} U_{top} L_{pip}\left(T_{pan}(x) - T_{ind,m}\right)dx = \frac{2U_{top}L_{pip}}{\sqrt{\frac{U_{bot}+U_{top}}{k_{pan}\delta_{pan}}}}\left[\frac{e^{\sqrt{\frac{U_{bot}+U_{top}}{k_{pan}\delta_{pan}}}\Big/\phi} - 1}{e^{\sqrt{\frac{U_{bot}+U_{top}}{k_{pan}\delta_{pan}}}\Big/\phi} + 1}\right]\left(T_{pan}(0) - T_{ind,m}\right) \tag{2.42}$$

Then the total heat transfer rate for the entire panel surface ($\dot{Q}_1$) is calculated by adding Eqs. (2.41) and (2.42), and it can be rearranged as follows.

$$\dot{Q}_1 = C_1\left(T_{pan}(0) - T_{ind,m}\right) \tag{2.43}$$

where:

$$C_1 = 2\sqrt{\left(U_{bot}+U_{top}\right)k_{pan}\delta_{pan}L_{pan}^2}\,\tanh\left(\sqrt{\frac{U_{bot}+U_{top}}{k_{pan}\delta_{pan}}}\Big/2\varphi\right) \tag{2.44}$$

To derive equations to couple $T_{pan}(0)$ with $T_{wat,m}$, first, the heat transfer rate from water to bonding material ($\dot{Q}_2$), which is located between pipe and panel, is calculated.

$$\dot{Q}_2 = C_2(T_{wat,m} - T_{pip,m}) \tag{2.45}$$

where:

$$C_2 = L_{bnd} L_{pip} h_{wat} \tag{2.46}$$

$$h_{wat} = (1663 + 24T_{wat,m}) u_{wat}^{0.8} / D_{inp}^{0.2} \tag{2.47}$$

The product $L_{bnd}L_{pip}$ in Eq. (2.46) represents the surface area matched between the pipe and bonding material as shown in Figure 2-5. Then, the heat transfer rate between bonding material and panel surface ($\dot{Q}_3$) is expressed as:

$$\dot{Q}_3 = C_3\left(T_{pip,m} - T_{pan}(0)\right) \tag{2.48}$$

where:

$$C_3 = W_{bnd} L_{pip} \frac{1}{R_{pip-bnd} + \sum \delta_i / k_i + R_{bnd-pan}} \tag{2.49}$$

The last term in Eq. (2.49) represents the overall thermal resistance between the pipe and the panel. The term $\sum \delta_i / k_i$ can be used for extra layers. Under the assumption that the top side of the water pipe is well insulated, all heat transfer rate to the water pipe is conducted from the radiant panel. Thus, $\dot{Q}_1$, $\dot{Q}_2$ and $\dot{Q}_3$ are equivalent due to energy balance. By eliminating $T_{pan}(0)$ and $T_{pip,m}$ with Eqs. (2.38), (2.43), (2.45) and (2.48), the cooling capacity of the ceiling panel can be calculated as:

$$\dot{Q}_{cap} = \frac{C_1 C_2 C_3}{C_1 C_2 + C_2 C_3 + C_3 C_1}\left(T_{wat,m} - T_{ind,m}\right) \tag{2.50}$$

One of the features of this model is that it includes specific geometric features of the ceiling panel type, such as the bonding thickness of material between the water pipe and the panel surface as shown in Figure 2-5. Furthermore, it includes a density of pipe layout (φ) that characterizes the water tube layout. However, the model requires both convection and radiation heat transfer coefficients as inputs rather than using a separate formulation similar to Eqs. (2.22)-(2.25). To validate the model, results were compared to

experimental measurements under steady state conditions, where the indoor temperature was fixed at 28°C, water flow rate was fixed at 2.5 L/min and water temperature varied from 12°C to 18°C. Detailed information of each parameter and the validation process can be found in [62].

Currently, there are no comprehensive passive chilled beam models available that are based on first principles. The only model publicly available is empirical and has been used in DOE 2.1E [63] and EnergyPlus [53]. The model was developed by one of the major manufacturers [64] and is a lumped model that calculates the cooling capacity according to air and water conditions and chilled beam geometry. Radiation heat transfer from the chilled beam surface and the driving force of low velocity air movement cannot be considered with this model. In Eq. (2.51), A'_{fin} is the surface area on the air side of the beam per unit beam length, m^2/m, and U is an overall heat transfer coefficient for heat transfer between the air in the indoor space and water in the pipe. The model neglects radiative heat transfer, so U is a function of temperature difference, mass flow rate of air through the beam ($\dot{m}''_{air}$) and water velocity (u_{wat}). Since the air flow is driven by temperature differences (natural convection), the mass flow rate of air through the beam is also correlated based on temperature difference between a fully mixed indoor air temperature and water temperature, supply side air volume flow rate and free area of coil in plan view (A'_{fre}). Default coefficients which represent a certain size of the chilled beam can be found in the manuals of DOE 2.1E [65] and EnergyPlus [66].

$$\dot{Q}'_{cap} = A'_{fin} U \left(T_{ind,m} - T_{wat,m} \right) \tag{2.51}$$

$$U = C_0 \left(T_{ind,m} - T_{wat,m} \right)^{C_1} \left(\dot{m}''_{air} \right)^{C_2} \left(u_{wat} \right)^{C_3} \tag{2.52}$$

$$\dot{m}''_{air} = \frac{C_4 \left(T_{ind,m} - T_{wat,m} \right)^{C_5} + C_6 \dot{q}'_{air,sup}}{A'_{fre}} \rho_{air} \tag{2.53}$$

2.3.1.2. Detailed Models

Detailed models described in this section focus on the passive ceiling cooler as the system of interest. They use fully mixed indoor air temperature as a boundary condition and discretize the system to calculate temperature distributions.

Antonopoulos [67]–[70] published a series of studies in the 1990s on the embedded type of radiant cooling systems. Although the initial work [67] presented a 1-D analytical model, the next studies mainly focused on the temperature distribution inside a slab, calculated cooling capacity per unit area of radiant ceiling, and conducted parametric analyses of the embedded system based on a numerical model. The 1-D modeling approach was similar to the Jeong and Mumma [47] simplified model, using a panel heat removal factor (C_{pan}) based on [49]. The second study [68] simplified a transient 2-D numerical model of the embedded slab into a periodic steady state 2-D model, by assuming a daily cycle of ambient temperature as a boundary condition – including periodic solar radiation on the radiant surface. The third study [70] focused on a transient 3-D numerical model of the embedded slab as shown in Figure 2-4. The governing transient conduction equations and their corresponding boundary conditions are shown below.

$$\rho_{slb} c_{p,slb} \frac{\partial T_{slb}}{\partial t} = \frac{\partial}{\partial x}\left(k_{slb} \frac{\partial T_{slb}}{\partial x} \right) + \frac{\partial}{\partial y}\left(k_{slb} \frac{\partial T_{slb}}{\partial y} \right) + \frac{\partial}{\partial z}\left(k_{slb} \frac{\partial T_{slb}}{\partial z} \right) \tag{2.54}$$

Boundary conditions:

$$\begin{cases} T_{slb}(0,x,y,z) = T_{slb,ini} \\ \dfrac{\partial T_{slb}(t,0,y,z)}{\partial x} = 0 \\ \dfrac{\partial T_{slb}(t,s+D_{otp},y,z)}{\partial x} = 0 \\ \dot{Q}''_{bot}(t,x,0,z) = h_{con,bot}\left[T_{ind,m}(t) - T_{bot,slb}(t,x,0,z) \right] + h_{rad,bot}\left[T_m(t) - T_{bot,slb}(t,x,0,z) \right] \\ \dot{Q}''_{top}(t,x,\delta_{slb},z) = U_{top}\left[T_{eqv}(t) - T_{top,slb}(t,x,\delta_{slb},z) \right] \end{cases}$$

$T_m(t)$ in the bottom side convection boundary condition represents the mean temperature of vertical walls and floor which physically corresponds to the *AUST* used in other studies described previously. T_{eqv} is defined as equivalent temperature; however, it can be equal to the indoor air temperature if the upper part of the slab is another floor instead of an exterior surface. The transient condition of the water flowing through the embedded

pipe is calculated using Eq. (2.55), where $\dot{Q}'_{wat}(t,z)$ is defined as the heat transfer rate per unit length (in the flow direction). The inlet water temperature is used as a boundary condition. Eq. (2.56) was used to couple Eq. (2.55) with Eq. (2.54) with the assumption of negligible effect of pipe thickness.

$$\left(\dot{m}c_p\right)_{wat}\frac{\partial T_{wat}(t,z)}{\partial z}=\dot{Q}'_{wat}(t,z) \tag{2.55}$$

$$T_{pip}=T_{wat}(t,z)+\dot{Q}'_{wat}/\left(\pi D_{otp}h_{wat}\right) \tag{2.56}$$

Eq. (2.57) represents transient indoor air temperature with variable load, where $\dot{Q}_{int}(t)$ is defined as the total internal load and $\dot{Q}_{cap}(t)$ is the heat extraction rate from the embedded cooling system. Here, a boundary condition that couples indoor air conditions with the cooling output of the embedded system is specified, along with an initial air temperature.

$$\rho_{air}V_{ind}c_{p,air}\frac{dT_{ind,m}(t)}{dt}=\dot{Q}_{int}(t)-\dot{Q}_{cap}(t) \tag{2.57}$$

Boundary conditions:

$$\begin{cases}T_{ind,m}(0)=T_{ind,ini}\\ \dot{Q}_{cap}(t)=n_{pip}\int_0^{s+D_{otp}}\int_0^{L_{pip}}\dot{Q}''_{bot}(t,x,0,z)dzdx\end{cases}$$

The fourth and last study [69] summarizes all of the previous studies and presented a parametric analysis of the system to identify the most significant parameters and provide steady state cooling capacity correlations for practical applications. The study also presented a validation of all models by comparing modeling results with experimental measurements. The most significant parameters were found to be pipe spacing (s+D_{otp}), pipe insertion depth from the radiant surface (d), water inlet temperature ($T_{wat,i}$) and room air temperature ($T_{ind,m}$). A fully mixed room air temperature and constant heat transfer coefficients of convection and radiation were assumed.

Tye-Gingras and Gosselin [71] proposed a semi-analytical steady state model (which can also be used for heating applications) to evaluate the performance of ceiling cooling

panels, focused on the temperature distribution on the panel surface. A distinctive feature of this model is that it considers serpentine tube layout (previous models considered parallel tube layouts). This physical geometry induces different water inlet temperature at each tube row inlet, which makes it relatively difficult to solve the problem analytically. Thus, the model solves differential equations numerically with simplified geometric coordinates. Parameters related to the model are shown in Figure 2-5. The model assumes adiabatic boundaries for both upper and side surfaces of the ceiling panel, thus, it is formulated based on energy balance as shown below.

$$\dot{Q}'_{wat} = \dot{Q}'_{lft} + \dot{Q}'_{rgt} + \dot{Q}'_{ctr} \tag{2.58}$$

The total heat transfer rate occurs in three ways according to the pipe-centerline; the heat transfer rate of left fin ($\dot{Q}'_{lft}$); right fin ($\dot{Q}'_{rgt}$); and fin base ($\dot{Q}'_{ctr}$). The left hand side term in Eq. (2.58) can also be expressed with a total thermal resistance (R'_{tot}):

$$\dot{Q}'_{wat} = \frac{\theta_{wat} - \theta_{pip}}{R'_{tot}} \tag{2.59}$$

The model assumes negligible thermal mass; therefore the pipe surface temperature is equal to that of the panel in contact with the pipe. Thus, T_{pip}, in the θ_{pip} term, can be considered as the fin base temperature in this model. $\dot{Q}'_{ctr}$ can also be expressed as:

$$\dot{Q}'_{ctr} = UD_{otp}\theta_{pip} \tag{2.60}$$

where U is the overall heat transfer coefficient between the panel surface and indoor air. It is defined as the sum of natural convection and radiation heat transfer coefficients, obtained from previous studies [4], [38]. $\dot{Q}'_{lft}$ and $\dot{Q}'_{rgt}$ can be expressed by fin equations:

$$\dot{Q}'_{lft} = U\eta_{fin,lft}L_{lft}\theta_{pip} \tag{2.61}$$

$$\dot{Q}'_{rgt} = U\eta_{fin,rgt}L_{rgt}\theta_{pip} \tag{2.62}$$

This is where the role of tubing layout becomes important and differs from previous studies. For a parallel tube layout, the fin length (in this case either L_{lft} or L_{rgt}) is generally equal to half of the tube spacing (s). However, since the fin base temperature (in this case T_{pip}) between two facing tubes will be different in a serpentine layout, the location of the

adiabatic condition is not at the middle of tube spacing and is not fixed. To solve the problem efficiently, the study introduces simplified coordinates shown in Figure 2-5. The χ-axis represents the water flow direction and the ξ-axis represents the inter-tube direction. By using the new coordinates, an asymmetry function ($\lambda(\chi)$) was defined as "the displacement of the adiabatic position with respect to the geometrical inter-tube symmetry line at any coordinate χ on the panel between the tube rows". Thus, the relationship shown below can be established between fin length and asymmetry function as a function of χ.

$$L_{lft}(\chi)=\frac{s}{2}-\lambda_{n-1}(\chi)\quad L_{rgt}(\chi)=\frac{s}{2}+\lambda_{n}(\chi) \tag{2.63}$$

The subscript below the λ function is the index number of tube row as shown in Figure 2-5. Also, the heat transfer mechanism of the entire panel can be expressed as follows:

$$\dot{Q}'_{wat}=-\left(\dot{m}c_p\right)_{wat}\frac{d\theta_{wat}}{d\chi}=\frac{T_{wat}-T_{ind,m}}{R'_{tot}(1+1/C_{pan})} \tag{2.64}$$

where:

$$C_{pan}=R'_{tot}U\left(\eta_{lft}L_{lft}+\eta_{rgt}L_{rgt}+D_{otp}\right) \tag{2.65}$$

$$\eta_m=\frac{\tanh\left(\sqrt{\frac{U}{k_{pan}\delta_{pan}}}L_m\right)}{\sqrt{\frac{U}{k_{pan}\delta_{pan}}}L_m}\qquad m=lft,rgt \tag{2.66}$$

Boundary condition:

$$\theta_{wat}(\chi=0)=T_{wat,i}-T_{ind,m} \tag{2.67}$$

The model uses initial temperature profiles of T_{wat} and T_{pip} that are calculated under the assumption of symmetric adiabatic condition, which makes the length of the fin a constant. They are analytically calculated as shown in [45] and are used in the iterative calculation procedure as initial inputs. Based on the initial analytical solution, $\theta_{pan}(\chi,\xi)$ and $\lambda_n(\chi)$ can also be derived analytically as shown below:

$$\frac{\theta_{pan,n}(\chi,\xi)}{\theta_{pip,n}(\chi)} = \frac{\dfrac{\theta_{pip,n+1}(\chi)}{\theta_{pip,n}(\chi)}\sinh\left(\sqrt{\dfrac{U}{k_{pan}\delta_{pan}}}\xi\right) + \sinh\left(\sqrt{\dfrac{U}{k_{pan}\delta_{pan}}}(s-\xi)\right)}{\sinh\left(s\sqrt{\dfrac{U}{k_{pan}\delta_{pan}}}\right)} \tag{2.68}$$

$$\lambda_n(\chi) = \frac{1}{\sqrt{\dfrac{U}{k_{pan}\delta_{pan}}}}\ln\left[\frac{\sqrt{-\left(\dfrac{\theta_{pip,n+1}(\chi)}{\theta_{pip,n}(\chi)} - e^{-s\sqrt{\frac{U}{k_{pan}\delta_{pan}}}}\right)\left(\dfrac{\theta_{pip,n+1}(\chi)}{\theta_{pip,n}(\chi)} - e^{s\sqrt{\frac{U}{k_{pan}\delta_{pan}}}}\right)}}{\dfrac{\theta_{pip,n+1}(\chi)}{\theta_{pip,n}(\chi)} - e^{-s\sqrt{\frac{U}{k_{pan}\delta_{pan}}}}}\right] - \frac{s}{2} \tag{2.69}$$

Eq. (2.68) simply shows the solution of the fin equation with a prescribed tip temperature condition. Eqs. (2.68) and (2.69) show that the panel surface temperature $T_{pan}(\chi,\xi)$ and the location where the temperature gradient becomes zero $\lambda(\chi)$ are functions of fin base temperatures of two tube rows facing each other ($\theta_{pip,n+1}$, $\theta_{pip,n}$), panel thermal conductivity (k_{pan}), panel thickness (δ_{pip}), tube spacing (s) and overall heat transfer coefficient (U). A detailed derivation of Eq. (2.68)-(2.69) is shown in [71]. Based on previous equations, the temperature profile of the panel surface is calculated by following the procedure shown in Figure 2-7 Figure 2-7where step (i) involves equations shown in [45], step (ii) involves Eqs. (2.68)-(2.69) and step (iii) involves Eq. (2.64). The model only considers the heat transfer at the bottom side of the ceiling cooling panel and fully mixed indoor air temperature, assuming there is no loss at the upper part of the panel. Although the model neglects the effect of semi-circular tube extremities and temperature gradient in parallel to the water flow direction, the results showed that such approximations are acceptable in terms of performance prediction.

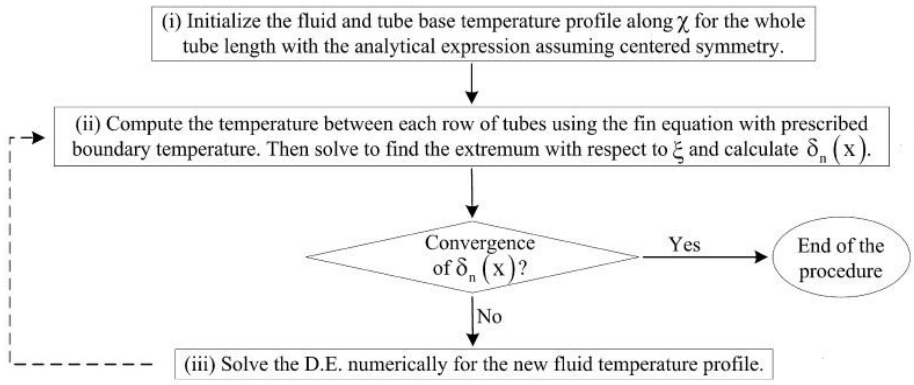

Figure 2-7. Iterative procedure of solving the problem.

2.3.2. Indoor Environmental Models

Indoor environment models focus more on the indoor space rather than the specific configuration of a ceiling cooling system as shown in Figure 2-3. Their main objective is to predict the effect of a ceiling cooling system on indoor environmental conditions. System parameters such as water temperature and specific geometry of the radiant ceiling system (e.g. pipe diameter, spacing, property etc.) are not considered in these models. However, they have the ability to include effects of heat gain, ventilation, radiation between surfaces and solar radiation which occur inside the zone. Most of the indoor models presented in this section are numerical models and since the ceiling cooling system is modeled as a boundary condition of either constant surface temperature or constant heat flux, it can be assumed that they physically represent a ceiling panel type or an embedded type.

2.3.2.1. Simplified Models

Castillo and Tovar [72] used simplified analysis to calculate the fully mixed indoor air temperature of the space. The model is categorized under indoor environment models since it does not handle any parameters related to radiant system's specification such as geometrical parameters and water conditions. In this study, a simplified theoretical model was developed that emphasizes two physical concepts: 1) a buoyant thermal plume which is generated by a heat source located at the floor and 2) a turbulent Rayleigh-Bénard convection developed from the chilled ceiling and which counteracts the heat flux

conveyed by the plume and cools the room. The basis of Rayleigh–Bénard convection theory can be found in previous studies [73]. Later, the theory was used to analyze stratification generated by a buoyancy source in a closed room. The solution of the problem is known as the filling box model [74]. The final form of the differential equation of the fully mixed indoor temperature within the space can be expressed as follows.

$$\frac{dT_{ind,m}}{dt} = \frac{\dot{Q}_{flr}}{\rho_{air} V_{ind} c_{p,air}} - C \frac{\alpha_{air}}{H_{ind}} \left(\frac{g\beta_{air}}{\alpha_{air} \nu_{air}} \right)^{2/3} \left[T_{ind,m} - T_{pan,m} \right]^{4/3} \quad (2.70)$$

Eq. (2.70) represents a space with adiabatic envelope and cooled ceiling and heated floor. Air properties (α_{air}, β_{air}, ρ_{air}, ν_{air}, $c_{p,air}$), room dimensions (V_{ind}, H_{ind}), power of heat source ($\dot{Q}_{flr}$) and temperature difference between fully mixed air ($T_{ind,m}$) and radiant panel surface ($T_{pan,m}$) are all considered in the equation. C in Eq. (2.70) is an empirical constant which can be obtained from experiments.

2.3.2.2. Detailed Models

Detailed models in this section mostly include CFD models based on a discretized indoor space. All reviewed CFD models are 3-D and steady state while boundary conditions in each model are different. Other modeling approaches discretize the zone into larger finite volumes that require less computation effort than CFD solutions. The models presented below are introduced in chronological order of development.

Rees and Haves [75] developed a nodal model of a 2-D space where a ceiling cooling system is combined with displacement ventilation. The purpose of this model is “to capture the effects of the vertical air and surface temperature gradients of the system and to make it computationally efficient enough for annual energy simulation”. Instead of discretizing a partial differential equation of an indoor space, this model uses a “semi-lumped” analysis by dividing a space into 10 air nodes, 4 vertical wall nodes and two horizontal surface (floor and ceiling) nodes. Positions of each node were selected as shown in Figure 2-8 to reflect the physical phenomena of the space, such as de-coupling of heat loads from the room air and recirculation. The basis of node positioning based on the physical phenomena is described specifically in [75]. The important parameters used

in this nodal model are convection heat transfer coefficients and air capacity rates. Experimental measurements were conducted to use mean temperatures of each node as inputs. Then, by using mass and energy balances between air to air nodes and between air to surface nodes, the capacity rates and heat transfer coefficients of each node were calculated numerically using EES software [76]. After the model was able to verify the relationship between temperatures at each node and both heat transfer coefficients and capacity rates, it was used reversely to predict air temperatures and heat transfer rates for their original intention. This requires generalized approaches for predicting the capacity rates and heat transfer coefficients of certain nodes. For the capacity rate, physical relationships between several nodes were simplified. For the heat transfer coefficients, correlations developed from previous studies were adopted for the chilled ceiling and other surfaces. The model was validated by comparing thermal loads and air temperature of each node with measured data.

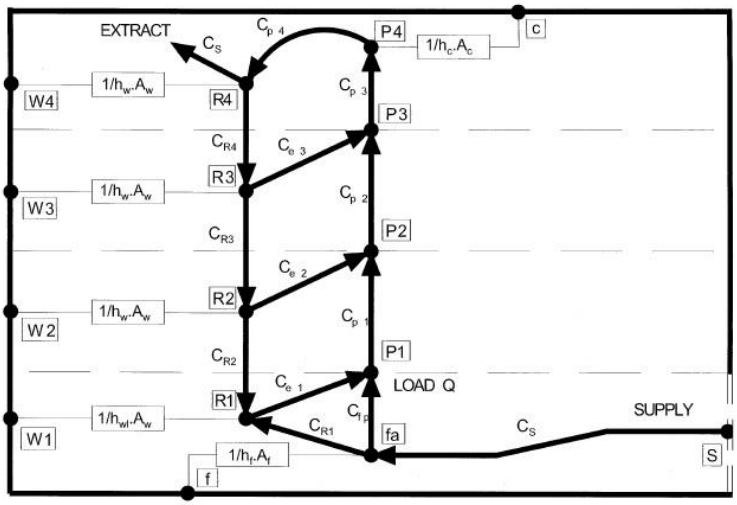

Figure 2-8. Representation of the nodal model [75].

Ben Nasr et al. [77] conducted a 2-D numerical study for a space with a chilled ceiling and a partially heated vertical wall. Staring from the general governing equations, they expressed 2-D governing equations with stream function in dimensionless form (Eq. (2.71)-(2.74)). The properties of air were assumed constant except for the density which

takes an important role in natural convection. $T_{pan,m}$ in Eq. (2.74) is the mean temperature of the chilled ceiling and $T_{int,m}$ is the mean surface temperature of the heated surface. Dimensionless numbers:

$$x^* = \frac{x}{H_{ind}\mathrm{Ra}^{0.5}} \quad y^* = \frac{y}{H_{ind}\mathrm{Ra}^{0.5}} \tag{2.71}$$

$$u^* = \frac{uH_{ind}}{\alpha\mathrm{Ra}^{0.25}} \quad v^* = \frac{vH_{ind}}{\alpha\mathrm{Ra}^{0.25}} \tag{2.72}$$

$$\psi^* = \frac{\psi}{\alpha\mathrm{Ra}^{0.75}} \quad \omega^* = \frac{\omega H_{ind}^2\mathrm{Ra}^{0.25}}{\alpha} \tag{2.73}$$

$$T^* = \frac{T - T_{pan,m}}{T_{int,m} - T_{pan,m}} \tag{2.74}$$

In this study the cooled ceiling and heated wall are at constant temperature while the other surfaces are considered adiabatic. The study numerically calculated air temperature and velocity inside the 2-D space with low and high *Ra* numbers which physically represent small and large temperature difference between surface and air.

Ayoub et al. [78] developed a model of a space cooled with a ceiling panel type system combined with displacement ventilation. An analytical wall plume model was first developed, and then it was used to develop a plume-multilayer model to apply in a space. The governing equations of the 2-D wall plume model (mass, momentum and energy) were used. No-slip and constant temperatures are specified as boundary conditions. The space installed with chilled ceiling was divided with four horizontal air layers (or air nodes) which are connected to four vertical wall sections, respectively. Solving mass and energy balance equations of each node was done similarly to the Rees and Haves nodal model [75]. A significant feature of this model is that it takes the non-uniformity of the wall temperature into account by dividing the space vertically into four air nodes and calculates the effect of this temperature variation. More specifically, by using the information of chilled ceiling temperature, supply air temperature, supply air flow rate, supply air humidity ratio, room dimension and space cooling load as inputs, the model can generate air and wall temperature variations with elevation, stratification height and panel cooling load. The model was further used in their extended work [79], [80] to

provide a design chart, correlations and an optimization process corresponding to a space installed with a ceiling cooling system coupled with displacement ventilation.

Kim et al. [81] coupled an optimization process with a CFD model to optimally design a radiant cooling system and an air conditioning system. A genetic algorithm was chosen to optimize indoor environmental parameters such as room dimensions, location of cooling panel, location of supply inlet, number of panels, panel surface temperature and width of supply inlet. After a combination of optimum parameters were selected, they were integrated within the CFD model to assess indoor thermal comfort. Other parameters which were not included in the optimization process, such as heat transfer coefficients and ventilation rates, were assumed constant.

Catalina et al. [82] evaluated thermal comfort in a space installed with a ceiling cooling system using both full-scale experiments and a CFD model. A low-Re k-ε model [83], which is an improved version of standard low Re k-ε models (where near-wall and low-*Re* effects in attached and detached flows are improved), was used to perform the CFD analysis. Three sets of steady state CFD simulations were performed (where the ceiling cooling surface temperature varied from 16.9^{o}C to 18.9^{o}C) with corresponding boundary conditions of other surfaces measured from the experiments. The radiosity method, which can calculate mean radiant temperature (MRT) for different positions along different axes by using view factors and surface temperatures obtained from the experiments, was also included.

Corgnati et al. [84] analyzed an office space equipped with a typical ventilation system coupled with a ceiling cooling system. CFD simulations were performed and they were validated with experimental measurements. The standard k-ε model was used and the boundary condition for the ceiling panel was treated as a fixed heat flux. The study used Archimedes number (*Ar*) as a generalized performance indicator of the system –where *Ar* is the ratio of thermal buoyancy force to inertial force. The main reason for using *Ar* was that the purpose of this study was to investigate the draft risk caused by a supply air jet and chilled ceiling surface. Thus, thermal comfort indices such as percentage of dissatisfied people due to draft and air diffusion performance index were calculated as a function of *Ar*.

Karadag [85]–[87] developed correlations of heat transfer coefficients that are meant to be representative for ceiling cooling systems. Several different combinations of room dimensions, emissivity, wall temperatures and ceiling temperature were applied within a 3-D CFD model. The work focuses on development of a correlation which is based on an assumption of fully mixed indoor space temperature. Using Eq. (2.75), which is based on a temperature difference between fully mixed room air and ceiling panel surface, both convection and radiation heat transfer coefficients were estimated from CFD model results for a floor temperature of 25^{o}C, ceiling panel surface temperature of 0-21^{o}C and wall temperatures between 28 and 36^{o}C. The correlations developed in [87] are based on:

$$\dot{Q}_{cap} = A_{pan} h_{con} (T_{ind,m} - T_{pan,m})(1 + \frac{h_{rad}}{h_{con}}) \tag{2.75}$$

where:

$$h_{con} = 2.6(T_{ind,m} - T_{pan,m})^{0.27} \tag{2.76}$$

$$h_{rad} / h_{con} = 3\varepsilon(T_{ind,m} - T_{pan,m})^{-0.3} \tag{2.77}$$

Taki et al. [88] reported on the performance of a new type of ceiling cooling system using data from experiments and CFD modeling. The ceiling panel system has a honeycomb slat under the ceiling panel to provide better stability of the natural convection-driven air flow. During the process of analyzing this system, a typical ceiling panel type cooling system was also modeled with CFD. A standard k-ε model was used in the CFD analysis and adiabatic walls were considered as boundary conditions. Different combinations of parameters were considered to represent various steady state conditions. For a space with 5.4 m of depth, 3 m of width and 2.8 m of height, ceiling surface temperature was varied from 12^{o}C to 21^{o}C and heat load was varied from 15 W/m^2 to 60 W/m^2 based on floor surface area. By adding the honeycomb slat, which is simply an extended surface of the ceiling panel, the amount of heat removed by the ventilation system was increased and the convection flow was stabilized compared to the conventional ceiling panel system. Chiang et al. [89] performed a full-scale CFD analysis of an office space where a ceiling cooling system and air dehumidification equipment were installed. A parallel experiment was conducted and measured data were used as boundary conditions for the CFD model

based on standard k-ε and the IMMERSOL radiation model. More specifically, average surface temperatures and emissivities were calculated for the hottest day in summer and were applied to the CFD model as constant boundary conditions. In addition to thermal comfort assessments, the effects of surface temperature of the ceiling panel, occupancy level, surface area of the ceiling panel and addition of ventilation system were studied.

2.3.2.3. Empirical Models

Several of the previously described models rely on correlations or constant values of heat transfer coefficients with respect to boundary conditions. This section includes efforts for determining empirical correlations (or constant values) of heat transfer coefficients using experimental data for a variety of ceiling cooling systems.

Novoselac et al. [90] developed correlations of convection heat transfer coefficients for a ceiling panel type cooling system using data from full-scale experiments that included tests both with and without a ventilation system. In that way, correlations were developed for natural convection and combined natural and forced convection. The purpose of this study was to capture the effect of vertical temperature variation in the space and the effect of a ventilation system. It focused on development of a new convection correlation by setting up the experimental measurements with minimal radiation effects using an internal heat gain device having low emissivity. The correlation for combined heat transfer coefficient, included in Table 2-3, was formulated as a function of ventilation air change rate and temperature difference between air temperature close to the ceiling (0.1 m from ceiling) and panel surface. The study also provides correlations for combined convection for the vertical wall and floor.

Causone et al. [91] evaluated heat transfer coefficients in a space equipped with a ceiling panel type. Total heat transfer coefficients were determined from experiments along with separate radiation and convection heat transfer coefficients for both heating and cooling cases. The experiments were conducted over a range of conditions, including water flow rates from 200 l/s to 240 l/s and supply air temperatures from 13^{o}C to 18^{o}C. Different reference temperatures were used to determine the heat transfer coefficients from the measurements as shown in Eqs. (2.78)-(2.80).

$$\dot{Q}''_{rad} = h_{rad,bot}(AUST - T_{pan,m}) \quad (2.78)$$

$$\dot{Q}''_{con} = h_{con,bot}\left(T_{ind,m} - T_{pan,m}\right) \quad (2.79)$$

$$\dot{Q}''_{cap} = U(T_{opr} - T_{pan,m}) \quad (2.80)$$

The radiation heat transfer coefficient was calculated based on *AUST* as shown in Eq. (2.78) and it was found that it can be treated as a constant value (5.6 W/m^{2}K) within the application range. Operative temperature was chosen to calculate overall heat transfer coefficient as shown in Eq. (2.80). The heat extraction rate was calculated using measured water flow rate, inlet and outlet temperatures and then used to estimate the overall heat transfer coefficient from Eq. (2.80). The average value of the overall heat transfer coefficient was 13.2 W/m^{2}K. The convection heat transfer rate was estimated by subtracting the radiation part from the total heat transfer rate. The average convection heat transfer coefficient was calculated as 4.4 W/m^{2}K based on a fully mixed room air temperature.

Andrés-Chicote et al. [92] also performed experimental studies to evaluate the cooling performance and heat transfer coefficients for a ceiling panel type system. The procedures and purpose were similar to the work of Causone [91]. A test chamber with 12.96 m^2 floor area, 3 m floor height, 5.04 m^2 window area and 1.67 m^2 of glazed door was equipped with a ceiling cooling system. Nine different combinations of test conditions were employed with ceiling surface temperatures ranging from 15.6^{o}C to 21.2^{o}C and indoor air temperatures ranging from 22.4^{o}C to 26.2^{o}C. The radiation and convection heat transfer coefficients showed good agreement with Causone's work - 5.4 W/m^{2}K and 4.2 W/m^{2}K, respectively. However, the total heat transfer coefficient was calculated as 8.5 W/m^{2}K which is quite smaller than the results of Causone's study. This difference is due to different definitions of operative temperature (T_{opr}) in Eq. (2.80). Since T_{opr} can be derived from different combinations of *AUST* and $T_{ind,m}$, different test conditions can cause different values of T_{opr}.

2.3.3. Integrated Models

Integrated models consider both the radiant system itself and the indoor environment as shown in Figure 2-3. Thus, it is conceptually a combination of a passive ceiling cooler model and an indoor environment model. Physical variations inside the space, system geometry and water flow conditions are all considered. Since some of the passive ceiling cooler models take a few indoor environmental properties into account, integrated models include additional parameters such as solar gains and radiation losses through walls and windows, or discretize the ceiling surface to calculate surface temperature variations.

2.3.3.1. Simplified Models

Diaz [93]–[97], [97]–[99] published a series of useful studies involving modeling of ceiling cooling systems for both ceiling panel and embedded types. A 1-D equivalent thermal network model was used to represent the steady state thermal behavior of the ceiling panel system. They also worked on transient models by coupling steady state radiant ceiling cooling model with transient indoor environmental model. The steady state model's node connections are shown as dotted lines in Figure 2-5. Based on the thermal network approach, the energy balance of the pipe node can be expressed as:

$$\dot{Q}'_{wat-pip} = \dot{Q}'_{pip-pan} + \dot{Q}'_{pip-top} \tag{2.81}$$

Eq. (2.81) shows that the energy extracted to the water is transferred from either the panel connected to the pipe or the top plenum of the ceiling panel. It can be formulated based on the temperature difference between mean water temperature and pipe surface temperature as shown in Eq. (2.82).

$$\dot{Q}'_{wat-pip} = \frac{T_{wat,m} - T_{pip,m}}{R'_{wat} + R'_{pip}} \tag{2.82}$$

where the resistance terms are described in Eqs. (2.89)-(2.90). The heat transfer rate to the water pipe from the panel can be expressed as a summation of heat transfer from the bottom (facing indoor) and top (facing plenum) surfaces of the ceiling panel.

$$\dot{Q}'_{pip-pan} = \dot{Q}'_{pan,bot} + \dot{Q}'_{pan,top} \tag{2.83}$$

The average panel surface temperature is calculated introducing fin efficiency:

$$T_{pan,m} = T_{ind,top} - \eta_{fin}\left(T_{ind,top} - T_{bnd}\right) \tag{2.84}$$

where T_{bnd} is the temperature at the bottom part of the bonding material (in contact with the panel), thus, it can be considered as a fin base temperature. $T_{ind,top}$ is the air temperature at the top part of the indoor space (or close to the chilled ceiling surface) and it can be expressed with weighting factors for overall heat transfer coefficients at the top and bottom sides, based on fully mixed indoor air temperature (T_{ind}) and air temperature in the ceiling plenum (T_{top}):

$$T_{ind,top} = \frac{U_{bot}T_{ind,m} + U_{top}T_{top}}{U_{bot} + U_{top}} \tag{2.85}$$

Then the 1-D fin equation is used to predict the panel surface temperature:

$$\frac{d^2T_{pan}}{dx^2} = \frac{U_{tot}\left[2\left(\delta_{pan} + L_{pan}\right)\right]}{\delta_{pan}L_{pan}k_{pan}}\left(T_{pan}(x) - T_{ind,top}\right) \tag{2.86}$$

The solution of this equation is:

$$\frac{T_{pan}(x) - T_{ind,top}}{T_{bnd} - T_{ind,top}} = \frac{\cosh\left[\sqrt{\frac{U_{tot}2\left(\delta_{pan} + L_{pan}\right)}{\delta_{pan}L_{pan}k_{pan}}}\left(\frac{s}{2} - x\right)\right]}{\cosh\left[\frac{s}{2}\sqrt{\frac{U_{tot}2\left(\delta_{pan} + L_{pan}\right)}{\delta_{pan}L_{pan}k_{pan}}}\right]} \tag{2.87}$$

Fin efficiency can be calculated based on adiabatic tip conditions as shown in the equation below:

$$\eta_{fin} = \frac{\sqrt{U_{tot}2\left(\delta_{pan} + L_{pan}\right)k_{pan}\delta_{pan}L_{pan}}\tanh\left[\frac{s}{2}\sqrt{\frac{U_{tot}2\left(\delta_{pan} + L_{pan}\right)}{\delta_{pan}L_{pan}k_{pan}}}\right]}{U_{tot}A_{fin}} \tag{2.88}$$

The water side, pipe and overall equivalent resistance between the pipe and the panel are defined in Eqs. (2.89)-(2.91) respectively.

$$R'_{wat} = \frac{1}{A_{inp}h_{wat}} \tag{2.89}$$

$$R'_{pip} = \frac{\ln\left|D_{otp} / D_{inp}\right|}{2\pi k_{pip}} \tag{2.90}$$

$$R'_{pip-pan} = \frac{\ln\left|\frac{D_{otp} + 2\delta_{bnd,top}}{D_{inp}}\right|}{\pi k_{bnd,top}} + \frac{\delta_{bnd,eqv}}{A_{bnd} k_{bnd}} + \frac{\delta_{bnd,bot}}{A_{bnd} k_{bnd,bot}} \quad (2.91)$$

A correlation developed by Celata et al. [100] was used for the water side heat transfer coefficient in Eq. (2.89). The overall resistance between the water pipe and panel is a combination of two contact resistances and a bonding material's resistance as shown in Eq. (2.91). The first term in Eq. (2.91) is the contact resistance between the pipe and the bonding material with a gap ($\delta_{bnd,top}$) which is experimentally determined. The second term is the resistance of bonding material formulated with equivalent bonding thickness ($\delta_{bnd,eqv}$) which represents an equivalent thickness of complicated geometry of the bonding material. The last term is the contact resistance between the bonding material and the panel. The ceiling panel type considered in this study considers a perforated panel. The effect of the perforation panel mostly appears in the characteristics of the air flow; however, this model includes the effect of the perforated panel geometry. Thus, parameters such as surface area of the entire panel surface, surface area of the panel cross section and perimeter of the panel, are redefined by introducing a porosity parameter. Detail definitions of the parameters are shown in [95]. To characterize thermal resistances between the ceiling panel and indoor air, experiments were performed to determine the heat transfer coefficient with values ranging between 5.9-6.5 W/m^{2}K. These values include the effects of panel perforation and ventilation. Radiation heat transfer coefficients for both bottom and top side of the ceiling panel were also determined from the experiments and were found to be around 5.25 W/m^{2}K. The same approach shown in Strand's model (ε-NTU method) was used for the water side equation to couple indoor conditions with the water supply conditions. When air temperatures of adjacent zones, water inlet temperature and mass flow rate, internal gains, supply air temperature and ventilation rate are known, the integrated model can predict water outlet temperature, ceiling average surface temperature, resultant room air temperature, cooling power of the radiant ceiling system and internal surface temperatures. Model predictions were in good agreement with experimental results. The results of these studies showed

that a steady state model of a ceiling panel type system can be used for a transient indoor environmental analysis without causing significant errors.

2.3.3.2. Detailed Models

Niu and Kooi [101], [102] developed a method to combine a ceiling cooling panel model with dynamic modeling of general building elements using a previously developed indoor analysis program (ACCURACY) [103]. The combined model uses three different approaches to analyze different elements. The transfer function method in ACCURACY is used to calculate thermal behavior of walls; the finite difference method in ACCURACY is used to calculate performance of the ceiling panel; and CFD is coupled with ACCURACY to obtain air flow patterns and temperature distributions of indoor air. Convection and radiation within the zone are taken into account as well as heat extraction by ventilation, in- and ex-filtration and solar radiation through the windows. For the ceiling cooling panel model, three different designs were considered. They were mathematically formulated based on 1-D heat conduction. Cooling capacity per unit panel surface area was expressed as a function of heat transfer rate between the water and the panel, including a second time-dependent term representing the variation of thermal mass of the panel (conduction through panel was assumed negligible):

$$\dot{Q}''_{cap} = h_{wat}(T_{pan,m} - T_{wat,m}) - \left(\rho V c_p\right)_{pan} \frac{dT_{pan,m}}{dt} \tag{2.92}$$

The water side energy balance is:

$$A_{pan} h_{wat}(T_{pan,m} - T_{wat,m}) = \left(\dot{m} c_p\right)_{wat} (T_{wat,o} - T_{wat,i}) + A_{pan}\left(\rho V c_p\right)_{wat,m} \frac{dT_{wat,m}}{dt} \tag{2.93}$$

where the right hand side terms represent energy variation while water flows from the inlet to the outlet. These equations were used to calculate required water temperature ($T_{wat,m}$) and panel surface temperature ($T_{pan,m}$) according to the required heat extraction rate ($\dot{Q}''_{cap}$). Their extended studies [104]–[108] included various application aspects of this integrated model. Except for potential energy savings with the ceiling cooling system, the condensation risk, the coupling with phase change materials or with a desiccant

cooling system and the improvement of thermal comfort were also analyzed. The ceiling cooling system showed promising energy performance with proper system arrangements. A report by Stetiu et. al. [109] provides predictions of the performance of a radiant ceiling cooling system with a program called RADCOOL. RADCOOL can calculate thermal loads, cooling capacity, air temperature and room surface temperature distributions. By coupling the program with SPARK (Simulation Problem Analysis and Research Kernel), which solves dynamic and non-linear equations corresponding to a complex physical system, both a ceiling panel type and an embedded type of radiant system could be modeled together with the indoor environment. A lot of other indoor analysis models assume uniform temperature conditions for all surfaces. However, this work divided the ceiling into 5 by 5 nodes to produce 2-D temperature variations along the ceiling. Also, the model has an ability to discretize the air temperature into 9 nodes based on the spatial characteristics of the zone. Their extended work [110] showed results for energy and peak power savings potential of radiant ceiling systems obtained using RADCOOL and DOE-2. RADCOOL was used to simulate the radiant system cases and DOE-2 was used to simulate conventional all-air systems. It was found that about 30% of energy and 27% of peak power demand could be saved by replacing a conventional system with a radiant cooling system for a single zone, based on 1999 California standards.

2.3.3.3. Black-box Models

A black box model has a “transfer function” characteristic that directly connects inputs and outputs and is usually trained with experimental or simulated data. Ferkl and Siroky [111] developed a black box model that can be used for control prediction and energy optimization of ceiling cooling system applications, based on an auto-regressive moving average with exogenous inputs (ARMAX) approach. Parameters of the model were estimated using subspace identification methods for an embedded type ceiling cooling system. A portion of a building in a university campus was chosen for the data acquisition. Ambient temperature, room air temperature, ceiling surface temperature, water inlet/outlet temperature to the ceiling panel, chiller supply temperature, three way

valve position and solar radiation intensity were measured to perform system identification.

Ge et al. [112] also developed a black box model which uses neural networks to predict condensation risk and to predict optimum pre-dehumidification time for a ceiling cooling system. Three separate models were developed. The first and second neural network models can predict the surface temperature of the ceiling panel type and dew point temperature, respectively, in a room at the start up moment to evaluate the risk of condensation. The third model can predict the optimum time for pre-dehumidification to prevent condensation. Although the model focuses on the risk of condensation rather than on performance, the performance of the ceiling cooling system is inherently included inside the training data. The data for training and validating the model was obtained from TRNSYS simulations, where the model included a dedicated outdoor air system (DOAS) coupled with a ceiling cooling system.

2.3.4. Findings and Limitations of Passive Cooling Systems Models

2.3.4.1. Summary and Discussion of Useful Findings

A variety of passive ceiling cooling system modeling approaches and modeling details were covered in the previous sections, according to different system types and domains of interest. Due to the large number of studies, it is difficult to choose the right modeling approach, assumptions and computed parameters that can help future model developers build more efficient and reliable radiant ceiling cooling system models. Moreover, for some system types (i.e., passive chilled beams), there are no validated models available. This section presents a summary of useful findings for future model developments; limitations in current models and needs for future work are described in the last section.

One of the key parameters in modeling radiant ceiling cooling systems is the heat transfer coefficient at the ceiling level. Specifically, the convection heat transfer coefficient which interacts with indoor air and the radiation heat transfer coefficient which interacts with indoor surfaces are important factors. Several studies suggested correlations of heat transfer coefficients as a function of indoor space parameters while others used constant values that were experimentally determined or adopted from previous studies. A

summary of convection and radiation heat transfer coefficients for ceiling panels or surfaces from existing literatures is presented in Table 4. Most of the correlations include a term with the temperature difference between indoor air temperature and radiant ceiling surface temperature, which is the driving force for natural convection. Correlations from [47] and [90] have an additional term which represents forced convection. Most of the "reference temperature difference" (ΔT_{ref}) definitions for convection heat transfer coefficients use fully mixed air temperature ($T_{ind,m}$) in the space and panel surface temperature ($T_{pan,m}$). However, there is one correlation [90] using air temperature at the ceiling level ($T_{ind,top}$) which is more suitable for stratified indoor environment models. Different forms of evaluation were used for ΔT_{ref} definitions for the radiation heat transfer coefficient, such as using *AUST* or operative temperature (T_{opr}), or simply using the fully mixed temperature ($T_{ind,m}$). Values from [91] and [92] were calculated based on experiments based on the temperature difference between T_{opr} and $T_{pan,m}$. Future model developers should be aware of what parameters were defined to calculate the reference temperature difference, and their application range.

The CFD models can be characterized in terms of the type and range of boundary conditions and specific turbulence models used. Table 2-4 summarizes the boundary conditions and assumptions/models used in CFD studies with radiant cooling systems presented in this section. The standard k-ε model was mostly used for the turbulence analysis. While one of the studies applied a radiation model to calculate a more accurate temperature field within the control volume, others did not use the radiation model since their focus was on the flow field or convective heat transfer analysis only. Boundary conditions varied between different studies. Studies which focused on flow field calculation often conducted an experiment to acquire values of boundary conditions which were then applied to the CFD model.

Some studies incorporate alternate methods for assessing distributed thermal comfort with lower computational requirements. For instance, Rees and Haves [75] computed vertical temperature distributions as a thermal comfort index with their nodal model. Ayoub et al. [78] and their extended work [79], [80] used their semi-analytic approach to compute stratification height and vertical temperature gradient in order to assess thermal

Table 2-3. Heat transfer coefficients used in previous modeling studies.

Reference	Convection from panel or ceiling surface		Radiation from panel or ceiling surface	
	h_{con} [W/m^{2}K]	ΔT_{ref}	h_{rad} [W/m^{2}K]	ΔT_{ref}
Kilkis et al. 1994b	$h_{con} \cong (1-2.22\times10^{-5} alt)^{2.627} \times(4.96/(4A_{flr}/P_{flr}))^{0.08} 2.67\left\|T_{pan,m}-T_{ind,m}\right\|^{0.25}$	$T_{ind,m}$-$T_{pan,m}$	$h_{rad,bot} = e\sigma\left[0.9659+0.00495(T_{pan,m}-10)\right]\times10^8$	$AUST$-$T_{pan,m}$
Jeong, Mumma 2007	$h_{con,bot} = FC_{con,bot}+2.13(T_{ind,m}-T_{pan,m})^{0.31}$ $h_{con,top} = FC_{con,top}+0.134(T_{ind,m}-T_{pan,m})^{0.25}$	$T_{ind,m}$-$T_{pan,m}$	$h_{rad,bot} = 5\times10^{-8}\left[(AUST+273)^2+(T_{pan,m}+273)^2\right] \times\left[(AUST+273)+(T_{pan,m}+273)\right]$ $h_{rad,top} = 4.8\times10^{-8}\left[(T_{ind,m}+273)^2+(T_{pan,m}+273)^2\right] \times\left[(T_{ind,m}+273)+(T_{pan,m}+273)\right]$	$AUST$-$T_{pan,m}$ $T_{air,top}$-$T_{pan,m}$
Okamoto et al. 2010	$h_{con,bot}$ = 5.65-6.05	$T_{wat,m}$-$T_{pan,m}$	$h_{rad,bot}$ = 2.54	$T_{ind,m}$-$T_{pan,m}$
Antonopoulos, Tzivanidis 1997	$h_{con,bot}$ = 4	$T_{ind,m}$-$T_{pan,m}$	$h_{rad,bot}$ = 4	$AUST$-$T_{pan,m}$
Rees, Haves 2001	$h_{con,bot}$ = 5.9	-	-	-
Ayoub et al. 2006	Min et al. (Min et al. 1956)	$T_{ind,m}$-$T_{pan,m}$	-	-
Karadağ 2009a	$h_{con,bot} = 2.6(T_{ind,m}-T_{pan,m})^{0.27}$	$T_{ind,m}$-$T_{pan,m}$	$h_{rad,bot} = 3\varepsilon h_{con}(T_{ind,m}-T_{pan,m})^{-0.3}$	$T_{ind,m}$-$T_{pan,m}$
Novoselac et al. 2006	$h_{con,bot} = \left[\{2.12(T_{ind,top}-T_{pan,m})^{0.33}\}^3+(2ACH^{0.39})^3\right]^{1/3}$	$T_{ind,top}$-$T_{pan,m}$	-	-
Causone et al. 2009	$h_{con,bot}$ = 4.4	$T_{ind,m}$-$T_{pan,m}$	$h_{rad,bot}$ = 5.6	T_{opr}-$T_{pan,m}$
Andrés-Chicote et al. 2012	$h_{con,bot}$ = 4.2	$T_{ind,m}$-$T_{pan,m}$	$h_{rad,bot}$ = 5.4	T_{opr}-$T_{pan,m}$
Diaz, Cuevas 2010	$h_{con,bot}$ = 5.9-6.5, Yuge (Yuge 1960)	$T_{ind,m}$-$T_{pan,m}$	$h_{rad,bot}$ = 5.2-5.3	$T_{ind,m}$-$T_{pan,m}$

comfort. Stratification height is the height where there is zero mass flow rate (air velocity is zero), which ideally should occur at the occupant height for optimal thermal comfort. The simplified models, thermal network and black-box models reviewed in this paper assumed fully mixed indoor air temperatures and can only be used to estimate average comfort levels for the entire space.

There are many parameters that are significant and should be considered in evaluating the performance of ceiling cooling systems. For example, Antonopoulos et al. [69] performed a parametric study of an embedded type ceiling cooling system and considered more than ten parameters associated with the embedded slab's geometry, properties, and operating

conditions. After conducting the parametric study, the most significant parameters were selected and used to develop a correlation for system cooling capacity. The selected parameters were water inlet temperature, internal load, pipe spacing, depth of the embedded piping and indoor temperature. [93] performed a parametric study to analyze the sensitivity of several parameters' uncertainty on model results for the ceiling panel type system. Bonding thickness, characteristic length, diffuser air velocity, panel porosity, panel conductivity, panel emissivity and tube conductivity were all considered. Parameters which had the largest effect on model uncertainty were characteristic length (half distance of tube spacing), conductivity and emissivity of the panel.

Although this section focuses on modeling approaches for radiant ceiling cooling systems, the final goal of related studies will be to assess the integrated performance of such a system incorporated in a whole building simulation model. This could include transient modeling of the entire system to provide results for the overall performance and practical guidelines when considering controls. For analysis of control performance, it is necessary to include transient radiant ceiling cooling models. However, for energy performance analysis, a couple of studies showed that steady state ceiling panel models (without capacitance) can be coupled to a transient indoor environment model to represent the integrated performance without causing significant errors. Diaz et al. [96] coupled a steady state model to a transient indoor environmental model and the combined model's dynamic behavior showed good agreement with experimental results. Also, Mossolly et al. [113] coupled a steady state model [44] with a transient indoor environmental model of [78]. Stratification height, vertical temperature gradient and power consumption of the system were used to validate the model with the experiments.

Table 2-4. Specifications of 3-D steady state CFD models of indoor environment with a ceiling cooling.

				Ceiling			Vertical wall			Floor		Glazing	Supply air	
Reference	**Turbulence model**	**Radiation Model**	**Code**	T_{pan}	h_{con}	Q''	T_{wal}	h_{con}	**Adia-batic**	T_{flr}	h_{con}	h_{con}	$T_{air,sup}$	$\dot{q}$
				℃	W/m^2-K	W/m^2	℃	W/m^2-K	-	℃	W/m^2-K	W/m^2-K	℃	m^3/s
Kim 2007	Standard *k-ε*	n/a	n/a	9-21	6			4			3	3.2	16	0.25
Catalina 2009	Low-Re *k-ε*	n/a	STAR-CCM+	16.9 -18.9			25.4 -26.4			25 -25.9				
Corgnati 2009	Standard *k-ε*	n/a	FLOVENT		5	17.7 -25								0.02
Karadağ 2009a	Standard *k-ε*	n/a	FLUENT	0-21			28 -36			25				
Taki 2011	Standard *k-ε*	n/a	Sabre-One	14-21					YES				19	0.05
Chiang 2012	Standard *k-ε*	IMMERSOL	PHOENICS	18-22			28.1 -29.5			28.5			18 -24	0.07 -0.14

2.3.4.2. Limitations in Existing Passive Ceiling Cooling System Models

In this section, limitations in existing models and needs for future work are discussed. Model numbers listed in Table 2-1 are used to discuss models described in section 3 for direct and easy tracking.

The primary purpose of developing component models is to enable system simulation, where radiant ceiling cooling systems are coupled with other models to simulate a zone or the entire building in order to evaluate overall performance. In addition to energy consumption, thermal comfort is an important factor that needs to be evaluated in comparing radiant and more conventional systems. Usually, there are asymmetric comfort conditions in building zones due to variability of internal heat gains, solar gains from windows and air flows due to ventilation and/or air-conditioning systems. To correctly evaluate thermal comfort in a space, distributions of thermal comfort within the space should be considered. The most popular static comfort models are the predicted mean vote (PMV) and the predicted percentage of dissatisfied (PPD). These models require indoor air temperature as one of the parameters to calculate PMV and PPD. The primary aim of CFD studies (model number 15-20 in Table 2-1) described in this paper was to evaluate spatial thermal comfort using temperature and velocity distributions. Although CFD modeling is a computationally expensive approach compared to other types of models, it is an effective way to evaluate indoor thermal comfort when air flows are significant. All of the CFD models reviewed in this paper assumed steady state conditions with boundary conditions which were idealized or measured experimentally. Since the models used different sets of boundary conditions to represent ceiling cooling systems, the results cannot be generalized for other conditions, system/space geometries, and different configurations. Catalina et al. (model number 16 in Table 2-1) and Chiang et al. (model number 20 in Table 2-1) mainly calculated PMV distributions throughout the space to evaluate comfort. Kim et al. (model number 15 in Table 2-1) used a fully mixed air temperature assumption in an optimization process and then used the optimized configuration to perform CFD analysis for evaluating thermal comfort in terms of both PMV and vertical temperature distribution. Corgnati et al. (model number 17 in Table 2-1), calculated PPD due to draft. Since the more detailed modeling has demonstrated the

importance of considering spatial comfort variations for passive ceiling cooling systems, building simulation codes need to evolve in order to consider these effects before passive ceiling cooling can be adequately assessed by system designers. Thus, there is a definite need to develop more practical simulation approaches that can fully couple “fast” CFD with building thermal models in order to provide more general assessments of the benefits of passive ceiling cooling systems (as well as other building systems) in terms of both comfort and energy. Ultimately, the goal is to have distributed comfort models with radiant system models fully embedded within commercial building simulation tools.

The fully mixed air temperature assumption (model number 1-11, 24, 27-28 in Table 2-1) is particularly poor for spaces having significant solar radiation transmission through windows, which can significantly affect interior surface temperatures. Averaging surface temperatures without considering the localized effects of absorbed solar energy has an impact on indoor environmental parameters, on comfort indices and on energy use, as well as on the correct prediction of a ceiling cooling system’s performance. For these situations, more detailed models for solar absorption and distribution [114] with or without complex fenestration systems [89] that use accurate radiation exchange calculations can be integrated with zone and passive ceiling cooler models to provide more accurate representations. Furthermore, if multiple air nodes are considered (model number 12 and 14 in Table 2-1) in lumped and thermal network models, it is possible to accurately assess distributed thermal comfort in a simpler manner.

Previous optimization studies (model number 15, 27-28 in Table 2-1) for passive ceiling cooling have used black-box models that were trained using experimental (or field measured) or simulated data. This is a reasonable approach if the training data is sufficient to fully characterize the relationship between the important inputs and outputs. In Kim et al.’s (model number 15 in Table 2-1) case, the optimization was used as a pre-process to fix the room and system configuration before their next step of CFD analysis. A lot of parameters such as location and width of diffuser, location of cooling panel, number of cooling panels and surface temperature were considered to find the optimum configuration of the system in terms of thermal comfort. Additional work is needed to

generalize this type of optimization approach before it can be included within a design process for passive ceiling cooling systems.

Typically, passive ceiling cooling devices are controlled to maintain space conditions through sensible cooling only, whereas a parallel cooling unit is applied to the ventilation stream to manage both latent and sensible loads associated with ventilation requirements. These space and ventilation loads can be met in a variety of ways leading to opportunities to minimize energy use through optimized controls. Also, since the load on passive ceiling cooling system will differ from the load on conventional all-air system [10], the model should be able to take this difference into account. For example, simplified passive ceiling cooler models (model number 7 and 8 in Table 2-1) which only use indoor air temperature as the sole parameter in the energy balance equation will not be able to capture the actual transient cooling load on the passive ceiling cooling system. The averaged radiant temperature such as *AUST* or operative temperature should be taken into account to capture the difference. Although one of the previous studies (model number 26 in Table 2-1) have specified a control logic for radiant systems to respond to specific building loads, relatively few studies have assessed the performance of different control strategies with passive ceiling cooling system model. Mossolly et al. [113] studied control optimization for a ceiling cooling system coupled with displacement ventilation. Different control strategies were applied within an integrated model that included multi-layer plume model (model number 14 in Table 2-1), ceiling panel model (model number 3 in Table 2) and Braun's cooling coil model [115]. Among three different control strategies, an optimum strategy which minimizes energy consumption was chosen. Most of the models (model number 1-5, 7-8, 10, 12-14, 27-28 in Table 2-1 excluding CFD models) reviewed in this study represent a steady state condition. Steady state models are efficient in terms of computing for energy performance analysis, however, it has not been verified whether they are appropriate for detail control analysis. Thus, additional work is necessary to study the level of transient analysis needed to properly assess passive ceiling cooling controls and additional control strategies should be investigated for a range of different systems, climates, and utility rates.

Finally, there is a clear lack of validated models for passive chilled beams and this will be discussed in detail in the following section.

2.4. Passive Chilled Beam System

There are several experimental studies [116]–[119] which focused on the flow pattern and how it affects the performance of passive chilled beams. Although these studies provide useful findings related to how the flow pattern driven by a passive chilled beam interacts with different experimental setups, the results are specific to the case studies considered and cannot be generalized. In addition, there is a lack of a full-scale experimental studies with passive chilled beams operating under various environmental and control conditions. Although chilled beam manufacturers provide performance maps as shown in Table 1-1, the test conditions and measurement details are not fully available to the public, limiting the potential for developing reliable models for use in building simulation.

In fact, the literature review in the previous section only identified one chilled beam model (model number 8 in Table 2-1, [64], [66] that is based on an experimental correlation provided by a single chilled beam manufacturer. Furthermore, there is no published validation of the model. The model is able to estimate the total cooling capacity of the passive chilled beam based on its geometrical specification, averaged indoor conditions and averaged operating conditions. Although this kind of model can be implemented in a building energy tool for a performance analysis of a passive chilled beam system, the model requires iteration at each time step for calculating averaged operating conditions such as average water and air temperatures as input parameters to the model. The computational efficiency can be improved by replacing averaged conditions with inlet conditions such as water supply temperature and air temperature above the passive chilled beam.

Another aspect of the existing passive chilled beam model is that it cannot provide any outputs that can be used to assess thermal comfort such as surface temperature (balanced by convection and radiation heat transfer) of the bottom panel of the passive chilled beam or the air velocity passing through the chilled. Passive chilled beams are mostly

considered as a convective cooling device although a typical passive chilled beam has a chilled panel that exchanges radiation heat transfer with indoor surfaces and occupants. Thus, a comprehensive passive chilled beam model should represent the natural convection flow caused by the temperature difference between indoor air temperature and water supply temperature and should represent the radiation heat exchange from the bottom panel.

Additional research is necessary to develop accurate and computational efficient models for passive chilled beams that can be integrated within system simulations to assess energy and comfort performance. Different modeling approaches may be appropriate for different purposes. For analysis of system performance for building design, empirical approaches that neglect dynamics would be appropriate if manufacturers' data are available for matching the model to specific devices. If such data are not available, then simple physics-based models that employ readily available geometric and physical parameters would be appropriate. For control analysis, dynamics should be included within models that are specified with a few parameters or based on empirical steady state performance data with additional parameters for characterizing transient performance.

2.5. Radiant versus Air Systems

Radiant systems, including passive chilled beam system, are known for their improved thermal comfort due to radiant effects. It is possible to use pre-defined thermal comfort indices such as Predicted Mean Vote (PMV) and Predicted Percentage of Dissatisfied (PPD) to compare how an indoor space is controlled between two different systems. This can either be achieved through experiments or computer simulations.

An extensive field measurement and side-by-side comparison between typical variable air volume (VAV) system and radiant system was conducted in a commercial building in India [120]. The commercial building having 23,226 square meters (250,000 ft^2) has a symmetrical building geometry where the north and south walls have relatively larger portion of building exterior surface. Typical VAV system is installed in the west half of the building while a radiant system is installed in the east half of the building. In-slab embedded type radiant cooling system is mostly installed throughout the east wing while

passive chilled beams are installed only in conference rooms. Measurements were taken for a year and differences between two systems were compared. The results showed that the radiant system saved 34% relative total energy compared to the VAV system and provided 18% increase in thermal comfort based on occupants' surveys. Also, practical information such as investment costs was compared between two systems. This extensive field study is a showcase for the benefits of such systems and easier market penetration. However, it cannot be generalized for other cases (i.e., climate and operating conditions); therefore, a reliable model integrated with a whole building simulation tool is needed. There are several studies that compare the effects between conventional air systems and radiant systems based on computer simulations [28], [106], [110]. All of these studies are modeling chilled (or heated) ceiling panels, which perform quite differently than passive chilled beams.

2.6. Integrated Building Simulation and Applications

Since passive chilled beam is a modular unit which can be installed on the ceiling with multiple units and in various layouts, and since there will always be a parallel air system (e.g. DOAS) which handles the latent and ventilation load, the entire system should be considered in evaluating energy efficiency and thermal comfort. In order to analyze this combined effect, an integrated simulation including a building envelope and the passive chilled beam system needs to be developed. This study will either use a simple envelope model which has been developed [121] to analyze the performance of passive chilled beam system in simulated environments.

There can be different application studies for a passive chilled beam system once the integrated model is validated. In terms of design, sizing and determining the layout of multiple passive chilled beams based on desired indoor conditions is necessary. There is a study [10] that highlights that conventional methods of predicting the load in a space can be different from calculating the correct load for a radiant system. This difference mostly comes from the fact that the radiant cooling system can almost instantly react to radiative heat gain while a conventional system processes this radiative heat gain when it becomes convective. Integrated building simulation can provide correct sizing of a passive chilled

beam system by taking this effect into account. Additionally, there is no study on detailed control of the passive chilled beam system. The most efficient way to control the passive chilled beam system, theoretically, is to decouple sensible and latent load and efficiently handle those between passive chilled beams and DOAS, separately. Efficiently controlling the system will also depend on climatic factors, captured by whole building simulation tools.

Passive chilled beams are typically installed with a parallel air system that handles both latent load and ventilation requirements. In other words, although the passive chilled beam can be driven by natural convection, the parallel air system creates forced air movement into the space that can affect the performance of the passive chilled beam. Additionally, there can be different types of air distribution systems such as overhead, displacement ventilation (DV) and underfloor air distribution systems (UFAD). Thus, the interaction between certain air distribution systems and passive chilled beams also needs to be analyzed for practical applications.

2.7. Aims of Thesis

The aims of the thesis are narrowed down based on comprehensive literature review of related research topics starting from the radiant cooling system and followed by the passive ceiling cooling system and passive chilled beam system as shown in previous sections. While the passive chilled beam is the main focus of this thesis, different aspects are analyzed at both the component and system levels. At the component level, modeling improvements such as increased computational efficiency and predictions of the cooling capacity and chilled surface temperature of the passive chilled beam are covered based on experiments and modeling effort (Chapter 3). At the systems level, field studies and computer simulation studies are conducted for analysis in a real world application (Chapter 4.1), development of the system level simulation tool (Chapter 4.2), synergy with other components in the system (Chapter 5) and analysis on climatic limitations (Chapter 5). The aims of this study mostly cover the basic needs of understanding the passive chilled beam system operation and performance and will contribute in future design and applications in buildings.

CHAPTER 3. EXPERIMENTAL INVESTIGATION AND MODELING OF A PASSIVE CHILLED BEAM

3.1. Performance Characterization of a Passive Chilled Beam

In this chapter, a performance characterization of a passive chilled beam is covered by two different experiments and a modeling effort based on those experimental results. A primary goal was to compare performance from testing of a single passive chilled beam in a laboratory environment with performance determined from testing of multiple passive chilled beams in an office setting.

3.1.1. Performance Measurements of a Passive Chilled Beam in a Controlled Environment

3.1.1.1. Experimental Facility and Configuration

The purpose of this experiment is to generate performance data for characterizing the performance of a single passive chilled beam under controlled conditions. In turn, this data will be used to develop passive chilled beam performance models that can be used within system simulation tools. Under different operating conditions (air temperature, surface temperatures, water supply temperature and water flow rate), comprehensive parameters are measured to capture both convection and radiation characteristics of the passive chilled beam.

The test bed in Bowen Laboratory at Purdue University (West Lafayette, Indiana) is capable of testing different HVAC systems in two adjacent identical rooms under the same weather conditions as shown in Figure 3-1. It is a light-weight and tight building where top, east, south and north are facing the ambient (west facing the other test room)

and windows installed on south wall and on north entrance. Dimension details of these test rooms are shown in Figure 3-2.

Figure 3-1. Twin test rooms at Bowen Laboratory.

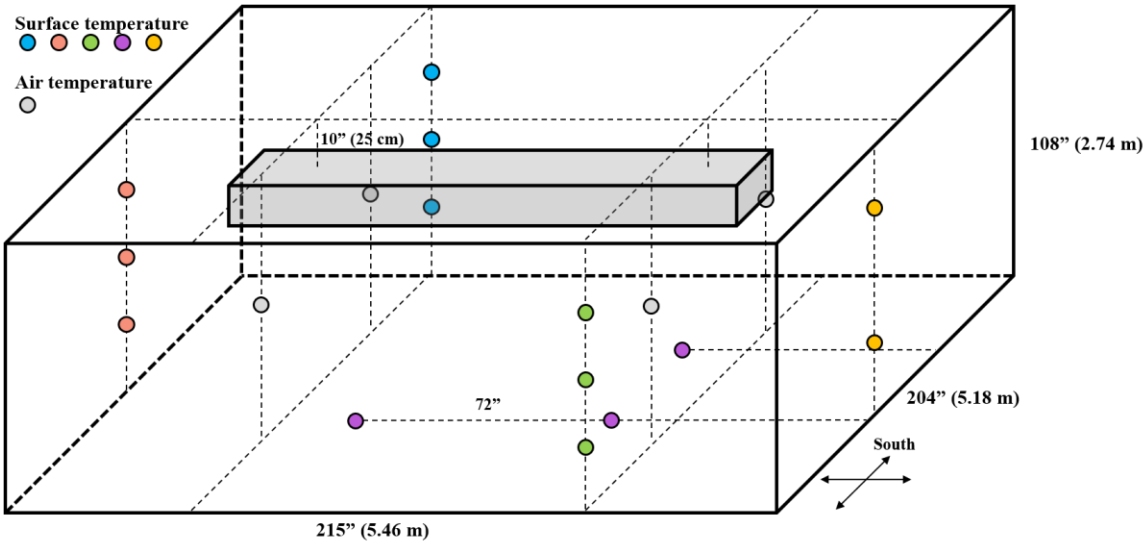

Figure 3-2. Dimension details of Bowen test rooms.

The configuration of the experimental setup is shown in Figure 3-3. All the equipment that is shown outside of the test rooms in Figure 3-3 is used to operate and control the HVAC equipment including the passive chilled beam and is installed in the mechanical room next to the twin test rooms. Chilled water to the passive chilled beam is supplied by a chilled water loop, where a vapor-compression refrigeration unit (Figure 3-4) is combined with a 119 gallon chilled water tank. The vapor-compression refrigeration unit has a two stage cooling capability with 2-5 ton cooling capacity and up to 13.3 EER. The

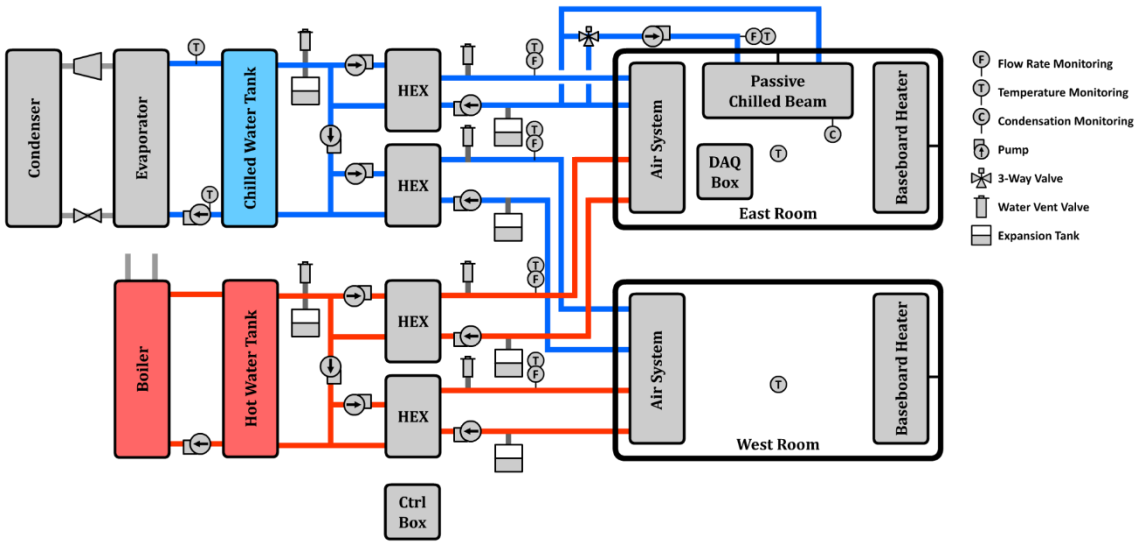

Figure 3-3. Configuration of a single passive chilled beam system.

temperature of the chilled water tank is maintained as low as possible to provide enough cooling power for the chilled beam testing. This is accomplished by controlling the water outlet temperature from the evaporator right above the freezing point with on/off control of the vapor-compression refrigeration unit. A heat exchanger is installed between the chilled water tank and the passive chilled beam water loop. This heat exchanger and a set

Figure 3-4. Vapor-compression refrigeration unit.

of water pumps on both sides of the heat exchanger are used to control the water supply temperature and water flow rate separately. A 3-way valve and an additional variable speed pump are installed in the passive chilled beam water loop to control temperature and water flow, respectively, through the passive chilled beam. A photo of the mechanical room is shown in Figure 3-5.

Figure 3-5. Mechanical room at Bowen Laboratory.

The chilled beam and its dimensions are shown in Figure 3-6. As it is shown in Figure 3-2, the passive chilled beam is installed on the middle of the ceiling of the room at 2.35 m height. The gap between the top of the chilled beam and the ceiling surface is 25 cm. Indoor environmental variables are monitored as follows (instrumentation specification data listed Table 3-1). Indoor temperatures are measured with thermocouples in four different points that are equally spaced inside the test room at 1.5 m height as shown in Figure 3-2. Indoor surface temperatures (vertical walls, floor and chilled beam surface) are also measured with thermocouples. Thermally conductive epoxies are used for the vertical wall and floor thermocouple attachments to increase conduction from the surface. The thermocouple locations are also shown in Figure 3-2. The temperatures of two different points on the bottom perforated panel of the passive chilled beam, equally

spaced in the length-wise direction, are measured with thermocouples firmly attached to the surface of the perforated panel as shown in Figure 3-7.

Figure 3-6. Installed passive chilled beam and its dimensions in Bowen test bed.

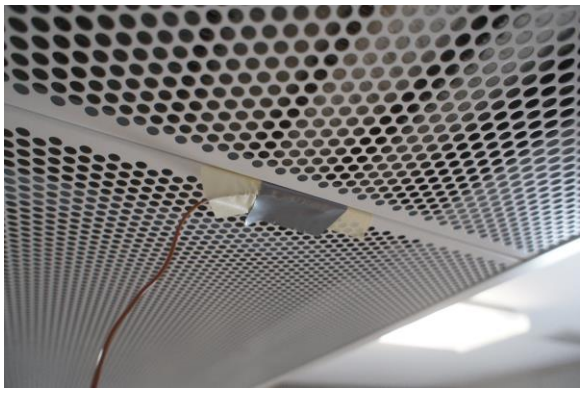

Figure 3-7. Thermocouple attachment on the surface of passive chilled beam.

Six thermo-anemometers shown in Figure 3-8 are used in this experiment to measure air velocities in the vicinity of the passive chilled beam. Three of them are installed on top of

the passive chilled beam, equally spaced in the length-wise direction and the other three are installed in the vertical direction starting from 0.3 m, 0.8 m and 1.3 m below the center of the passive chilled beam's perforated panel.

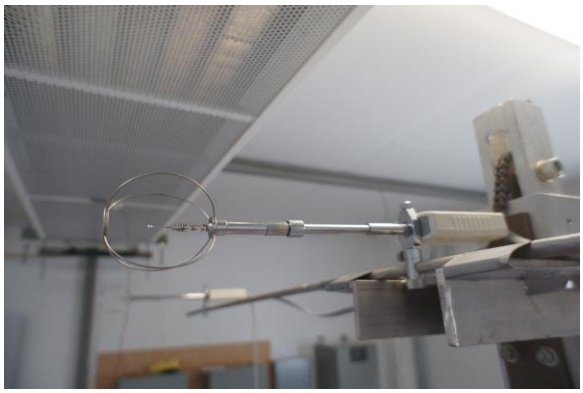

Figure 3-8. Thermo-anemometer.

An electric baseboard heater shown in Figure 3-9 is used to counteract the cooling power of the passive chilled beam unit to reach steady state conditions for reliable performance characterization.

Figure 3-9. Baseboard heater.

A National Instruments' (NI) data acquisition device cRio-9024 shown in Figure 3-10 is used to control the pump (Figure 3-11) and the 3-way valve (Figure 3-12) dedicated to the passive chilled beam and collect data during the experiments. A thermocouple module and analog input and output modules are used for wiring from and to instruments within the test room.

Figure 3-10. Data acquisition device.

Figure 3-11. Water pump.

Figure 3-12. 3-way valve.

Automated Logic's controller ME 812u-LGR and MEx 816u shown in Figure 3-13 are used to collect real-time values of sensor measurements and to control the vapor-

compression refrigeration unit and pumps in the mechanical room. All instruments described above are also shown in Figure 3-3 with specifications listed in Table 3-1.

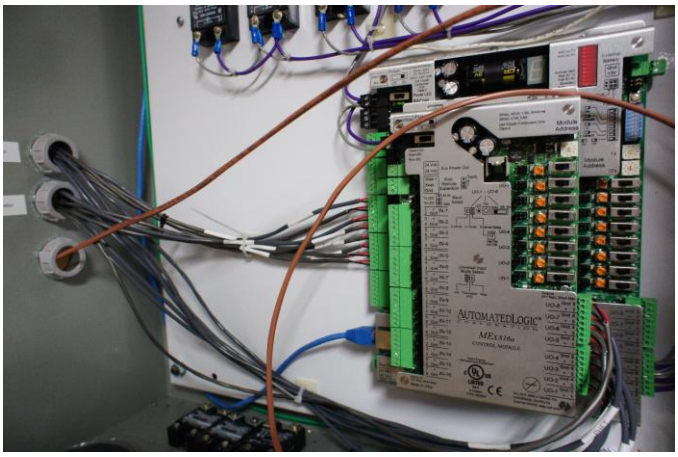

Figure 3-13. HVAC controller.

Table 3-1. Instrument specification in Bowen test bed.

Instrument	Model	Manufacturer	Accuracy
Passive chilled beam	QPVA	Fläkt Woods	-
3-way valve & actuator	B310+LRB120-SR	BELIMO	-
Pump (for chilled beam)	MAGNA 25-100	Grundfos	-
Pump	UP 26-64 F/VS, UP 15-10 F	Grundfos	-
Heat pump	25HCB6	Carrier	-
Thermocouple (Air)	TT-T-24-SLE-500	OMEGA	0.5^{o}C, 0.4%
Thermocouple (Water)	EXTT-T-24-100	OMEGA	1^{o}C, 0.75%
Water flow sensor	FTB-101, FLSC-35B	OMEGA	±0.5%
Thermo-anemometer	SensoAnemo5100LSF	SENSOR	±0.02 m/s, ±1.5%
Platinum RTD sensor	TE-703-A	Mamac Systems	±0.1^{o}C
Data acquisition	cRio 9024	National Instruments	-
Dehumidifier	DDR30B2GDB	Danby	-
Controller	ME 812u-LGR	Automated Logic	-
Controller	MEx 816u	Automated Logic	-

3.1.1.2. Experimental Procedures

The National Instruments' cRio-9024 data acquisition (DAQ) device is used to measure parameters in real-time and test different operating conditions of the passive chilled beam.

During two months (August to September 2016) of experiments, random combinations of operating conditions were tested using automated logic implemented in the DAQ. When the cooling load was not enough for testing certain operating conditions, the baseboard heater was turned on to balance the cooling load and maintain the proper operating conditions. In order to minimize the risk of condensation from the passive chilled beam when the humidity increases in the test room, a portable dehumidifier is installed in the space. The dehumidifier was operated when the relative humidity in the space reached 70% and was turned off when the dew point temperature in the space dropped to 8^{o}C. The operation of this dehumidifier was used as a transition point for moving to the next combination of operating conditions. Depending on the humidity level in the space affected by the weather conditions, elapsed time for each operating condition varied from less than an hour to several hours. After collecting measurements for two months, post-processing was performed to determine the steady state condition measurements. Whenever operating conditions could not maintain the steady state criterion (0.2^{o}C for the temperature difference between setpoint against the water supply temperature or the indoor average air temperature and 0.02 kg/s for the water flow rate difference) for at least 20 minutes, this measurement was considered unnecessary and was removed from the data set. The automated experimental procedure is summarized in Table 3-2.

Table 3-2. Procedure for automated single passive chilled beam experiments.

Step	Description
1	Randomly set a chilled water supply temperature between 15-18^{o}C
2	Randomly set an indoor space temperature setpoint between 20-24^{o}C
3	Randomly set a water flow rate between 0.05-0.15 kg/s
4	Remain at the current operating condition until the dehumidifier is turned on.
5	After the dehumidifier turns off, repeat step 1 to 4.
Post-processing	Select measurements at a steady state condition which satisfied operating for at least 20 mins with temp. changes of less than 0.2^{o}C and water flow changes of less than 0.02 kg/s.

3.1.1.3. Experimental Results

Experiments using the Bowen test bed were conducted from August to September 2016. Figure 3-14 shows an example of a consecutive experiment of 12 hours before the post-processing. This figure shows repeated tests of different operating conditions after repeated dehumidification operations. For this set of data, the window was covered and

lights were turned off to eliminate other heat gains. *AUST* is calculated in the post-processing based on measured surface temperatures in the test room while assuming 0.9 emissivity for all interior surfaces. Total cooling capacity is calculated based on the water flow rate and water temperature difference between inlet and outlet of the passive chilled beam.

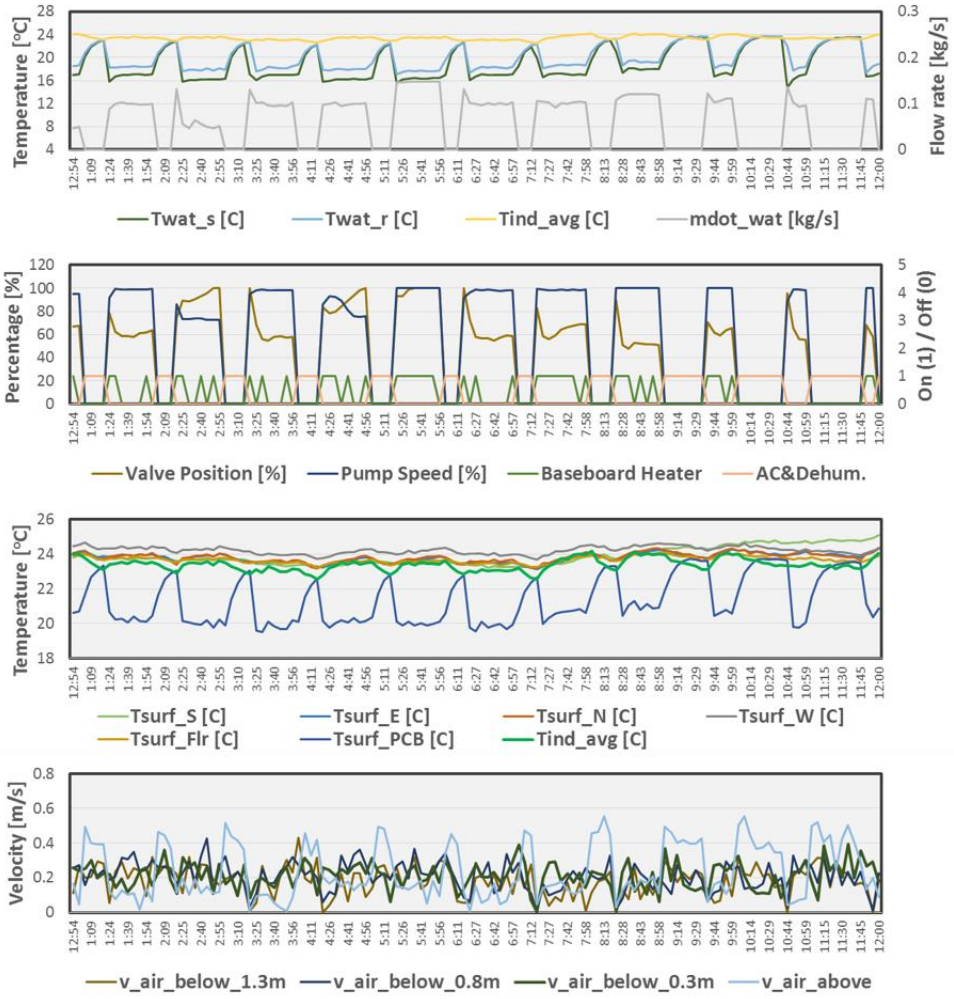

Figure 3-14. Example of experimental measurements in Bowen test bed.

Figure 3-15 shows a box plot for all of the measurements which are normalized based on maximum rated value (shown below Figure 3-15). All the measurements were mostly within recommended typical operating conditions.

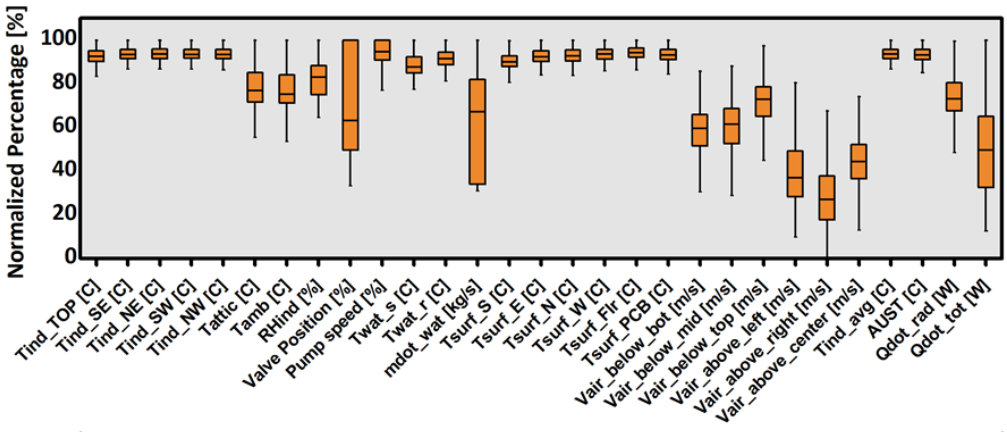

Rated Values for Parameters																												
$Tind_{TOP}$ [C]	$Tind_{SE}$ [C]	$Tind_{NE}$ [C]	$Tind_{SW}$ [C]	$Tind_{NW}$ [C]	T_{attic} [C]	T_{amb} [C]	RH_{ind} [%]	Valve Position [%]	Pump speed [%]	$Twat_s$ [C]	$Twat_r$ [C]	$mdot_{wat}$ [kg/s]	$Tsurf_S$ [C]	$Tsurf_E$ [C]	$Tsurf_N$ [C]	$Tsurf_W$ [C]	$Tsurf_{flr}$ [C]	$Tsurf_{PCB}$ [C]	$Vair_{below\_bot}$ [m/s]	$Vair_{below\_mid}$ [m/s]	$Vair_{below\_top}$ [m/s]	$Vair_{above\_left}$ [m/s]	$Vair_{above\_right}$ [m/s]	$Vair_{above\_center}$ [m/s]	T_{ind_avg} [C]	AUST [C]	$Qdot_{rad}$ [W]	$Qdot_{tot}$ [W]
25.2	24.2	24.1	24.2	24.2	37.4	33.6	68.9	100	100	19.5	20	0.1	25.8	25.0	25.3	25.0	24.4	21.2	0.3	0.4	0.3	0.2	0.2	0.2	24.2	24.9	46	813

Figure 3-15. Range of measurement parameters.

Figure 3-16 shows the operating conditions covered during this experiment and the total cooling capacity measurements. The left figure shows the range of indoor average air temperature (x-axis) and water supply temperature (y-axis), and three different levels of water flow rate, 0.05 kg/s ($\dot{m}_{wat,low}$), 0.1 kg/s ($\dot{m}_{wat,mid}$) and 0.15 kg/s ($\dot{m}_{wat,high}$) to the passive chilled beam. The markers inside the graph represents a valid point for each operating conditions which satisfied the steady state criterion (T_{error}<0.2°C / $\dot{m}_{wat,error}$ <0.02 kg/s) for a minimum of 20 minutes. Due to the equipment sizing issue in the mechanical room, the right bottom corner of the operating condition plot which represents higher cooling capacities was not reached in this experiment. The figure on the right shows total cooling capacity as a function of temperature difference between indoor average temperature and water supply temperature which is the driving force for the passive chilled beam's space cooling. The total cooling capacity was determined from measurements of water flow rate and water temperature difference between inlet and outlet of the passive chilled beam. Each point that was shown in the graph on the left is

aligned in the graph on the right according to the water flow rate level. The trend in terms of the total cooling capacity shows expected results where higher water flow rates show higher total cooling capacities when the other operating conditions are fixed.

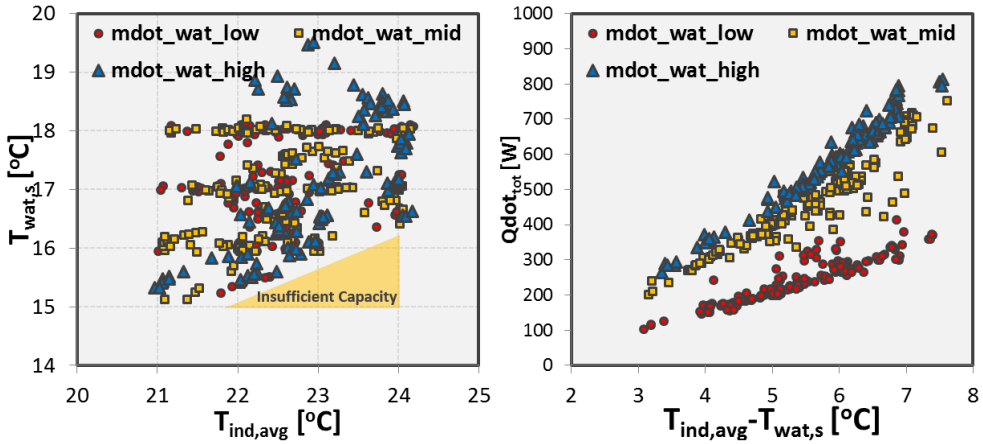

Figure 3-16. Coverage of operating conditions and total cooling capacity measurements in Bowen test bed.

Figure 3-17 shows the air velocity measurements in the vicinity of the passive chilled beam. As it is mentioned previously, six thermo-anemometers are installed below and above the passive chilled beam. The two graphs in the upper row and the left graph in the bottom row show the air velocity measurement in three different distances (0.3 m, 0.8 m and 1.3 m) from the bottom panel of the passive chilled beam. The graph in the right bottom corner shows the average air velocity measurement from three thermo-anemometers right above the passive chilled beam. The x-axis for all graphs is the temperature difference between the indoor average air temperature in the breathing level and the water supply temperature. As it is also covered in the previous study [117], the air flow field below the passive chilled beam is very unstable and it develops turbulent flow soon after the cold air falls down from the passive chilled beam. Although the average trend indicates that the air velocity increases with the temperature difference, which is expected, the actual measurements include a lot of oscillations at the same point of measurement during steady state conditions. Based on the findings from the previous study, when the passive chilled beam is operated with higher cooling capacity (larger temperature difference), the overall air velocities below the passive chilled beam also

increases as in results shown in Figure 3-17. While average measurements right above the passive chilled beam shows the slowest velocity, the air velocity at 80 cm below the passive chilled beam showed the fastest followed by the 30 cm distance and 1.3 m distance. These measurement results also follow the trend of findings from the previous study where the cold air accelerates (around 0.3 m distance) from the passive chilled beam to certain distance until the maximum velocity is reached (around 0.8 m distance). After passing the maximum point, the velocity gradually slows down (around 1.3 m distance). Analysis on the air flow field below the passive chilled beam is also an important topic in terms of precisely predicting the thermal comfort around the space. Since the flow is unstable and affected easily by internal gains in the breathing level, a numerical study on the flow field should be considered in future studies. However, this study only focuses on the average air velocity in the space based on measurements.

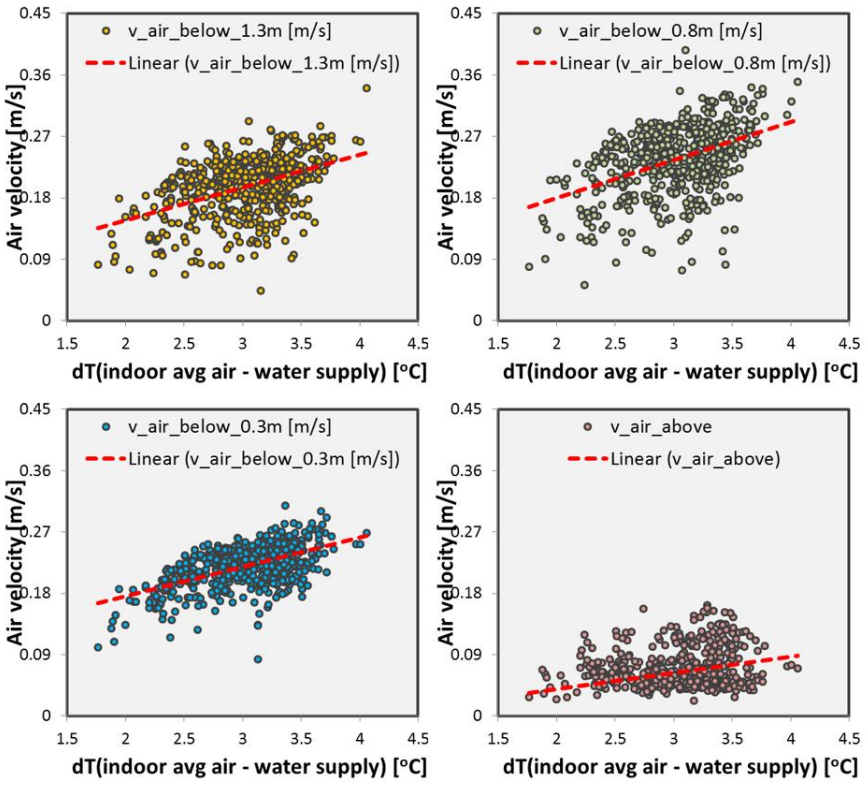

Figure 3-17. Air velocity measurements in the vicinity of the passive chilled beam.

3.1.2. Performance Measurements of Multiple Passive Chilled Beams in an Open Plan Occupied Office

3.1.2.1. Experimental Facility and Configuration

The purpose of this second experimental setup is to measure the in-situ performance of multiple passive chilled beams installed in a real occupied office space. The data is needed to understand how to translate the performance characterization of a single passive chilled beam to a real environment where multiple chilled beams interact with each other and a parallel air flow distribution system. The building automation system (BAS) was used to collect the data while operating the passive chilled beams under different operating conditions along with the use of a parallel air system.

The Living Laboratories of Ray W. Herrick Laboratories at Purdue University (West Lafayette, Indiana) are four open-plan office spaces designed with modular and reconfigurable envelope, lighting and comfort delivery (air distribution and radiant) systems. They can be used to assess the impact of building and system design and operation on energy use, indoor environmental conditions, and occupant comfort. One of the Living Laboratories (Living Lab #1) is equipped with 30 passive chilled beams, designed to provide the necessary cooling for the space. A wall air distribution system is used for satisfying latent load and ventilation requirements. Since the space is an actual office occupied with a maximum of 20 people, it is useful for studying the realistic performance of passive chilled beams at a realistic scale. The performance of passive chilled beams is relatively more affected by the indoor thermal conditions compared to conventional cooling systems due to the naturally convective cooling nature. For this reason, field measurements from a real occupied office space under different thermal conditions are taken to verify whether the model developed from testing on a single passive chilled beam can be used for a realistic environment with multiple passive chilled beams.

The test configuration in the Living Lab #1 (9.9m x 10.5m x 3.2 m high) is shown in Figure 3-18, including control equipment (pump, control valve, heat exchanger, diffuser and passive chilled beam) and sensors (temperature, valve position, pressure difference and flow rate). Thirty passive chilled beams, with dimensions shown in Figure 3-19, are

installed on the ceiling clouds and are divided into three banks to achieve variable cooling capacity near and far from the south-facing glass façade.

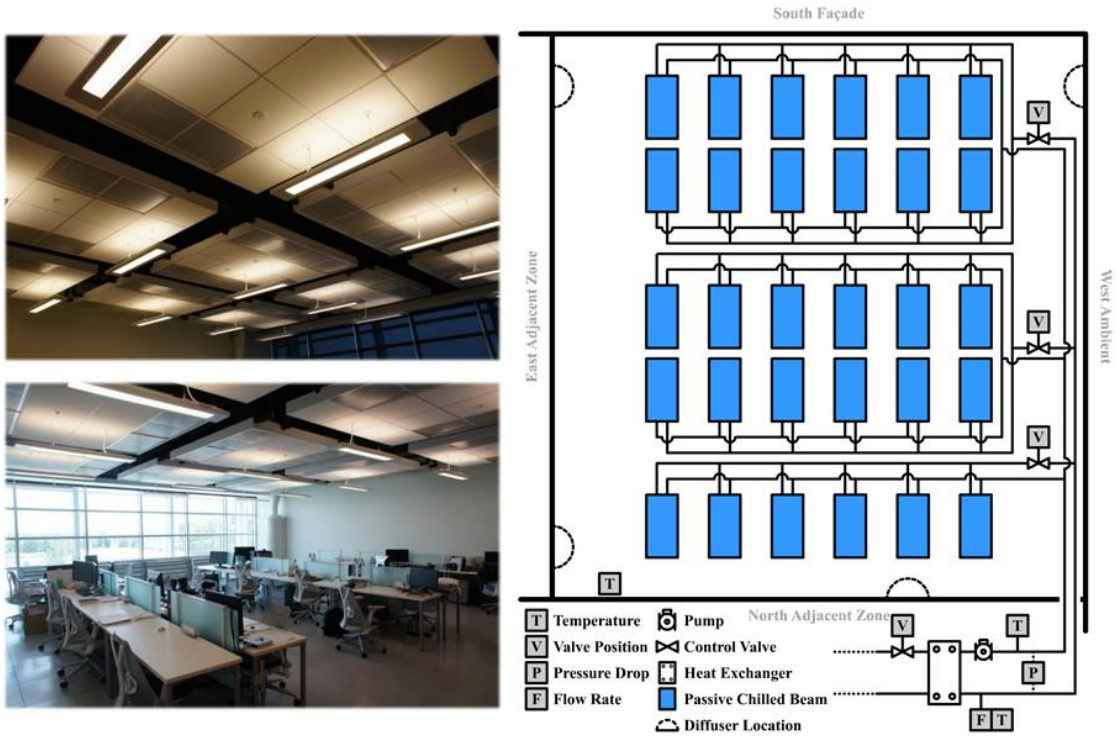

Figure 3-18. Configuration of multiple passive chilled beams system.

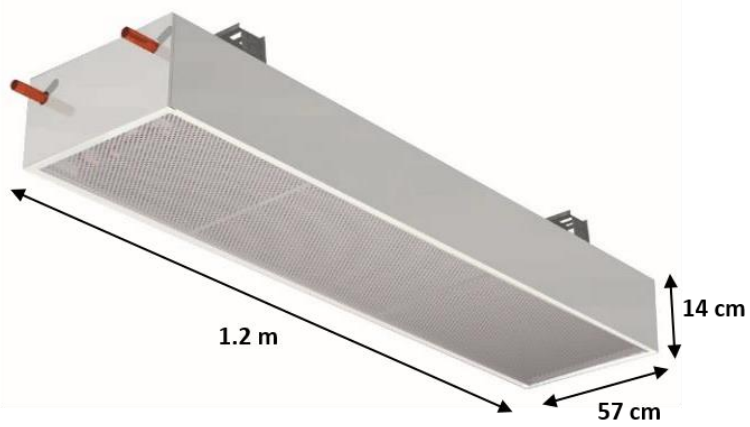

Figure 3-19. Dimension of the Passive chilled beam in Living Laboratory.

Supply water temperature to the chilled beam can be controlled through a heat exchanger connected to the district chilled water supply, using a valve on the chilled water loop. The pump is operated to maintain constant pressure difference in the chilled water loop; therefore, to test different water mass flow rates, the valve position in each bank must be varied accordingly. The current pump pressure set point in the office limits the water mass flow rate to a maximum value below the maximum typical operating range of the chilled beam. To achieve higher water mass flow rates, the valve of one of the chilled beam banks (middle bank) was kept closed during the experiments. In this way, 18 chilled beam units (south and north banks) were utilized for the field measurements for testing higher water flow rate level. In parallel, a wall air distribution system was operating to mainly handle the latent and ventilation loads. Four side-wall diffusers were used for this purpose, which have a relatively small effect on indoor air velocities (compared to conventional air distribution systems). The air system is variable air volume (VAV) and can control the space air temperature and the supply air flow rate. These features were used to maintain fairly constant indoor conditions during the measurements with passive chilled beams. A list of instruments is given in Table 3-3 and construction details are shown in Figure 3-20 and Figure 3-21.

Table 3-3. Instrument specifications in Living Laboratory.

Instrument	Model	Manufacturer	Accuracy
Passive chilled beam	QPVA	Fläkt Woods	-
Air temperature sensor	BA/BS2-WTH-SO	BAPI	±0.3^{o}C
Water temperature sensor	A/TT1K-I	ACI	±0.2^{o}C
Water flow sensor	F-1110	ONICON	±0.5%
Air flow sensor	Diamond flow sensor	Nailor Ind.	±5%
Globe thermometer	TB1	Monitor Sensors	±0.1^{o}C
Building Automation System	Niagara Framework	Tridium	-

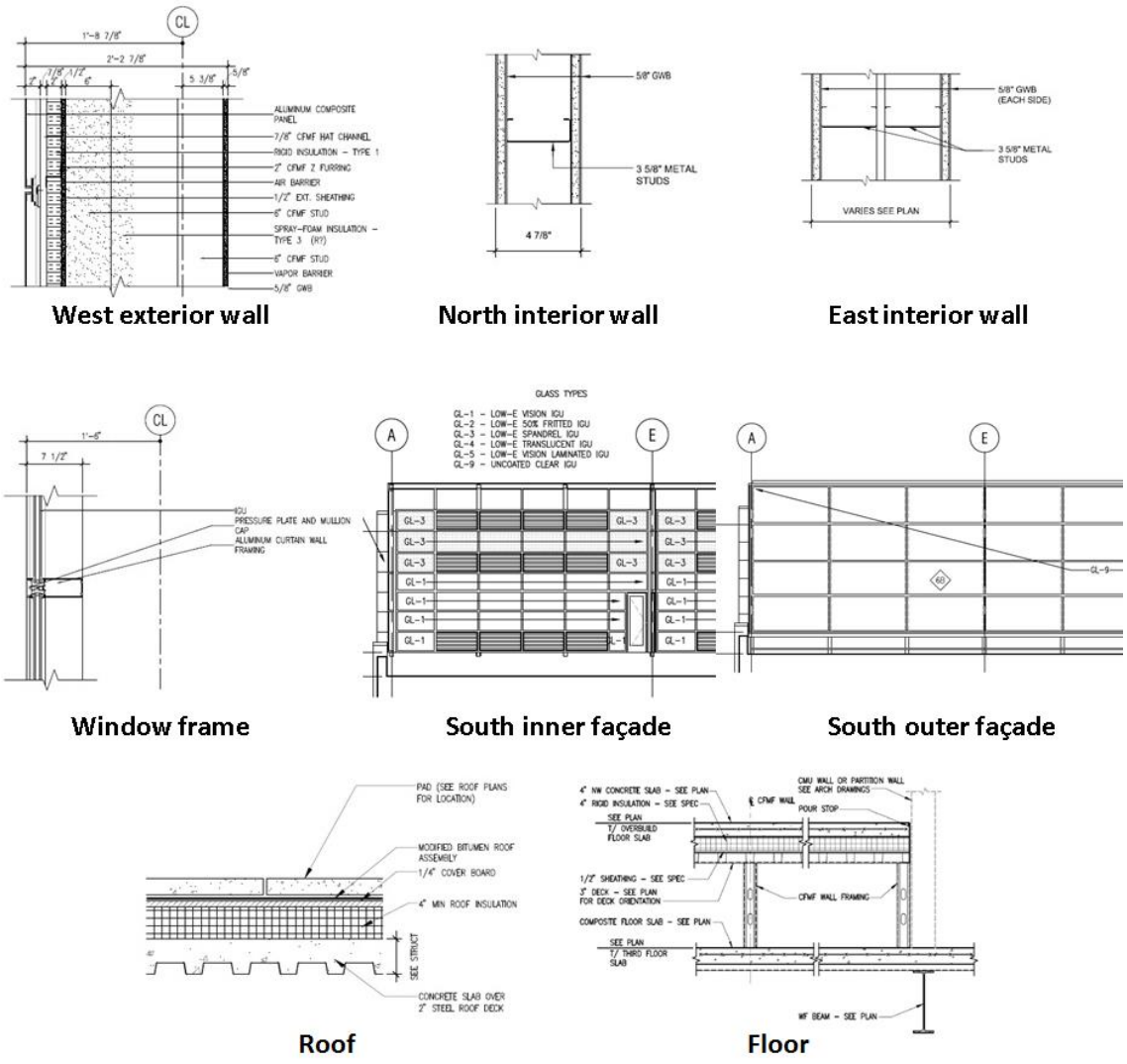

Figure 3-20. Construction details of Living Laboratory.

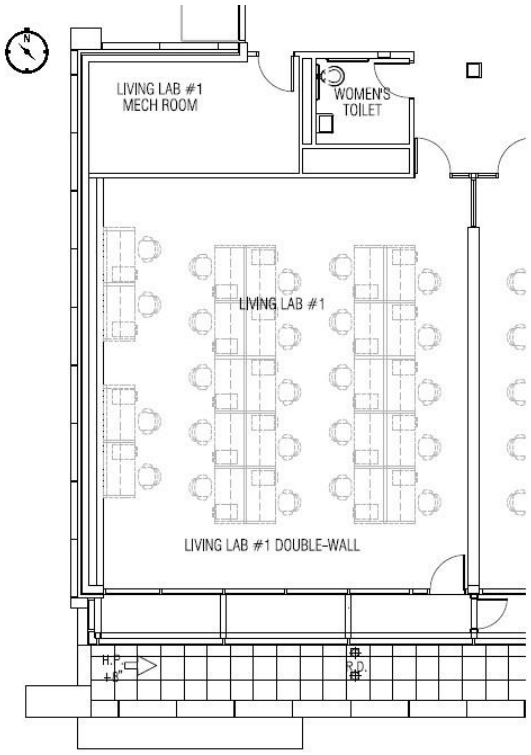

Figure 3-21. Plan view of Living Laboratory.

3.1.2.2. Experimental Procedure

One of the challenges with measuring the performance of passive chilled beams in an actual office space was to maintain relatively constant (steady state) conditions. In order to minimize the effects of occupants and solar radiation, the measurements were performed during nighttime and early morning, averaging data every 5 minutes. Additionally, each set of operating conditions was tested for at least two hours to achieve relatively steady state conditions. Since the Living Laboratories are controlled with a building automation system (BAS) using Tridium's NiagaraAX Framework, the test procedure was set up with the BAS and automatically controlled. Table 3-4 shows the steps of the measurement procedure, which were repeated during the experiment period, to obtain a sufficient range of operating conditions. Since the measurement of water mass flow rate in this setup represents the total flow rate through the multiple chilled beams (18 or 30 total), post-processing of the measured data was required to calculate the average cooling capacity of each passive chilled beam unit. Additionally, the first 15

minutes of data at the beginning of each set of measurements were removed to avoid transient effects.

Table 3-4. Procedure of field measurement.

Step	Description
1	Set space temperature set point and supply air flow rate (22-27^{o}C / 0-1200 CFM).
2	Set supply water temperature (14-18^{o}C).
3	Set chilled water flow rate (0.02-0.08 kg/s).
4	Maintain the current condition for two hours.
5	Repeat steps 1 to 4 until typical operating conditions are covered.
Post-processing	Remove first 15 mins of data for each operating condition measurement.

3.1.2.3. Experimental Results

Field measurements of the Living Lab #1 were taken from August to December 2015. Figure 3-22 shows collected measurements over the entire test period where the steady state condition was maintained for each operating condition. As shown in the first graph of the figure, the operating conditions were maintained relatively well compared to the Bowen test bed's experiment. For this reason, additional post-processing of filtering the steady state condition measurement was not necessary. Thus, the entire data set besides the first 15 minutes of transient measurement is used for the study. Rather than using the baseboard heater as in the Bowen test bed, the air system is used as the counter heating source for maintaining the certain operating condition when the cooling load is not enough. The second graph in Figure 3-22 shows the supply air temperature variation (between 20 to 60^{o}C) while the flow rate of the air system is fixed either in 600 CFM or 1200 CFM. As shown in the third graph, the number of passive chilled beams were varied between 18 and 30 units by closing and opening the valve connected to passive chilled beams. The total cooling capacity measurement in the bottom graph is calculated with the water flow rate and the temperature difference between inlet and outlet of entire passive chilled beam's water loop.

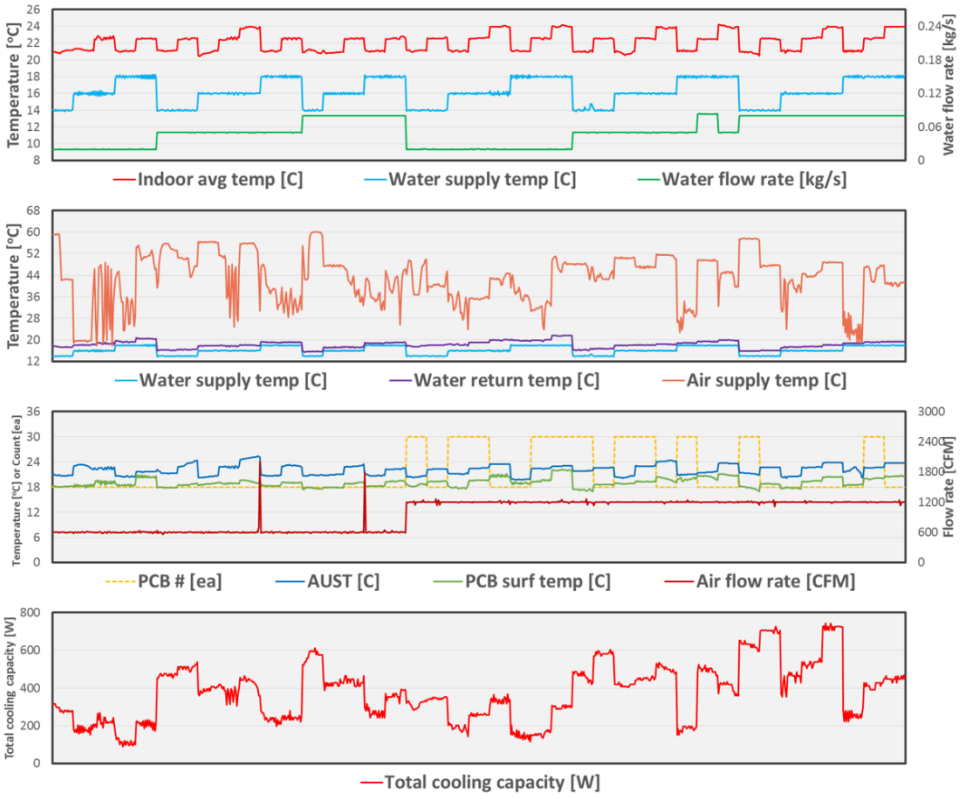

Figure 3-22. Entire field measurement in Living Lab #1.

Figure 3-23 shows a box plot for all the measurements which are normalized based on maximum rated value shown in the table below the figure. All parameters are within recommended typical operating conditions, except for the water flow rate which could not reach the maximum value of operating conditions as explained in section 3.1.2.1. Figure 3-24 shows the operating conditions covered during this experiment and the total cooling capacity measurement. The left figure shows the range of indoor average air temperature (x-axis) and water supply temperature (y-axis), and three different levels of water flow rate, 0.02 kg/s ($\dot{m}_{wat,low}$), 0.05 kg/s ($\dot{m}_{wat,mid}$) and 0.08 kg/s ($\dot{m}_{wat,high}$) to the passive chilled beam. Compared to the coverage acquired from the Bowen test bed shown in Figure 3-16, the data points are grouped within certain operating conditions and relatively lower water supply temperature (14^{o}C) were achieved in this field measurement.

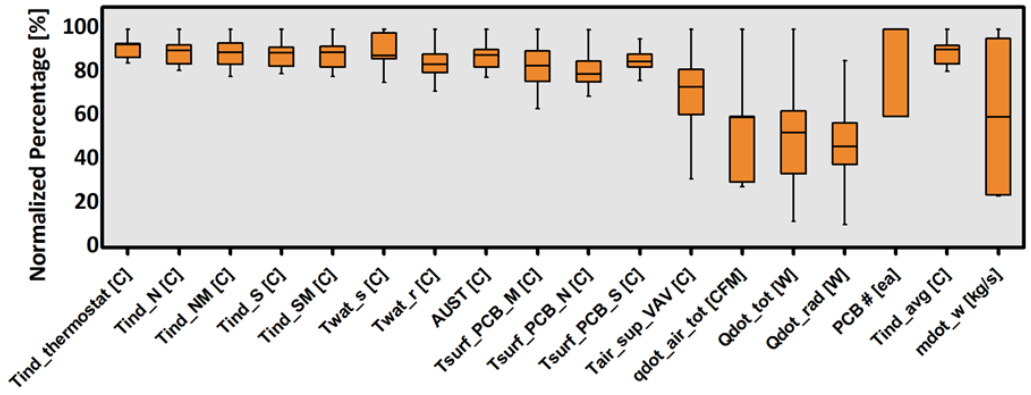

Rated Values for Parameters																	
$Tind_{thermostat}$ [C]	$Tind_N$ [C]	$Tind_{NM}$ [C]	$Tind_S$ [C]	$Tind_{SM}$ [C]	$Twat_s$ [C]	$Twat_r$ [C]	AUST [C]	$Tsurf_{PCB\_M}$ [C]	$Tsurf_{PCB\_N}$ [C]	$Tsurf_{PCB\_S}$ [C]	$Tair_{sup\_VAV}$ [C]	$qdot_{air\_tot}$ [CFM]	$Qdot_{tot}$ [W]	$Qdot_{rad}$ [W]	PCB # [ea]	$Tind_{avg}$ [C]	$mdot_{wat}$ [kg/s]
24.2	25.2	25.0	23.9	24.7	18.3	21.7	25.3	27.1	25.5	22.2	60.1	2006	744.2	24.7	30	24.6	0.1

Figure 3-23. Range of measurement parameters.

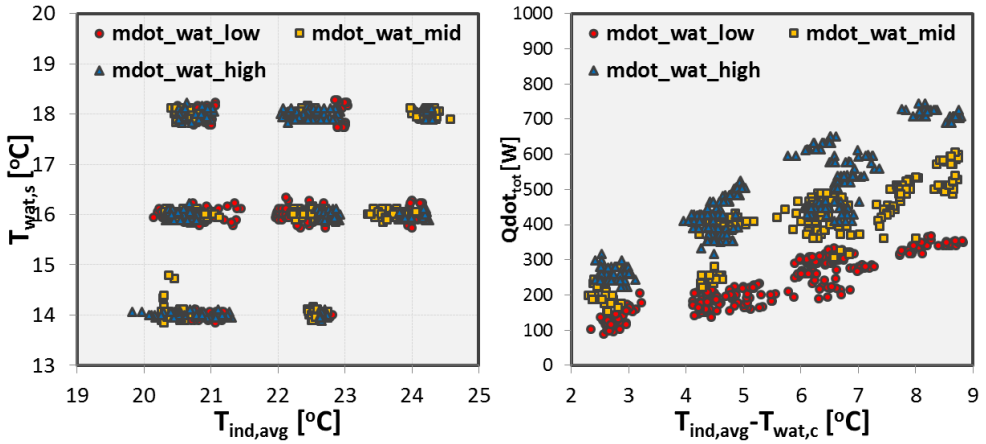

Figure 3-24. Coverage of operating conditions and total cooling capacity measurements in Living Laboratory.

3.2. Development of a Passive Chilled Beam Model

In this section, semi-empirical passive chilled beam models are developed based on measurements that were taken from the Bowen test bed and Living Lab #1. A comparison

between performances of the passive chilled beam in the Bowen test bed and Living Lab #1 is performed to verify the validity of an extended use of a model based on single passive chilled beam testing to an actual environment with multiple passive chilled beams.

3.2.1. Development of Semi-Empirical Models for a Passive Chilled Beam

Semi-empirical models for a passive chilled beam are developed based on the experimental measurements from the Bowen test bed and Living Lab #1. These models are able to estimate essential outputs for representing correct physical behaviors of the single passive chilled beam such as convective and radiative heat transfer characteristics. Different regression models with different combinations of relevant parameters were tested to choose the most precise and computationally efficient regression model. There are publically available regression models which are included in two different standards. The first standard [25] includes the simplest regression form which only uses the temperature difference between the air around the chilled beam and water mean temperature as the modeling input. A recent study [122] showed that this standard's regression form cannot represent the performance effects of varying water flow rate. Also this model uses the mean water temperature between the inlet and outlet of the passive chilled beam which would require iteration in each time step if the model is implemented in building energy simulation tools. For this reason, a new regression model was developed in this study. Eq. (3.1) presents this regression model for predicting the total cooling capacity which showed the smallest error compared to the other regression models that were tested. This model includes water mass flow rate ($\dot{m}_{wat}$) and temperature difference between air above the passive chilled beam ($T_{ind,top}$) and supply water ($T_{wat,sup}$). Each term is normalized based on nominal values ($\dot{m}_{wat_0} = 0.08\ kg/s$, $T_{wat,s,0} = 14℃,\ T_{ind,0} = 22.5℃,\ \dot{Q}_0 = 703\ W$) where the rating condition was assumed based on typical operating conditions ($T_{ind} = 22.5℃,\ T_{wat,sup} = 14℃,\ \dot{m}_{wat} = 0.08\ kg/s$) and the rated cooling capacity was selected based on the measurement with these operating conditions.

$$\dot{Q}/\dot{Q}_0 = a \times \left(\frac{\dot{m}_{wat}}{\dot{m}_{wat_0}} \right)^b \times \left(c + \frac{T_{ind,top} - T_{wat,s}}{\left(T_{ind} - T_{wat,s}\right)_0} \right)^d \quad (3.1)$$

A recently published standard [123] which is based on a previous study [64] presented a regression model that not only includes the water flow rate variation but also includes air density variation with different elevations. Although this model is an improvement in terms of predicting the performance of a specific passive chilled beam compared to the previous standard, it uses the mean water temperature as an input. In contrast, Eq. (3.1) uses the water supply temperature as an input and therefore does not require an iterative process at every time-step of a system simulation leading to improved efficiency with good accuracy.

Eq. (3.2) presents the regression model for predicting the surface temperature of the passive chilled beam which showed the smallest error compared to other regression models that were tested. The main reason for developing such a model is to verify whether the radiation cooling effect is significant in passive chilled beam applications. This model is in the form of a non-dimensional weighting factor (γ) assuming that the surface temperature of the passive chilled beam is between the water supply temperature and the air temperature above the passive chilled beam. This weighting factor is is correlated in terms of two different temperature differences and water mass flow rate. The temperature difference between *AUST* and $T_{wat,s}$ represents the radiation driving force for cooling and the temperature difference between $T_{ind,top}$ and $T_{wat,s}$ represents the convection driving force for cooling. Each term in the weighting factor equation is normalized based on nominal values ($\dot{m}_{wat_0} = 0.08\ kg/s, T_{wat,s,0} = 14℃, T_{ind,0} = 22.5℃, AUST_0 = 22.2℃$) where the rating condition was assumed based on typical operating conditions ($T_{ind} = 22.5℃,\ T_{wat,sup} = 14℃,\ \dot{m}_{wat} = 0.08\ kg/s$)

$$\gamma = \frac{AUST - T_{surf,PCB}}{AUST - T_{wat,s}},\ \gamma = a \times \left(\frac{AUST - T_{wat,s}}{\left(AUST - T_{wat,s}\right)_0} \right)^b \times \left(\frac{T_{ind,top} - T_{wat,s}}{\left(T_{ind} - T_{wat,s}\right)_0} \right)^c \times \left(\frac{\dot{m}_{wat}}{\dot{m}_{wat_0}} \right)^d \quad (3.2)$$

Matlab's nonlinear regression function was used to fit coefficients of Eqs. (3.1) and (3.2) with data sets acquired from section 3.1.1.3 and 3.1.2.3. Comparisons between these fitted regression models and the measured data for the corresponding operating

conditions are shown in Figure 3-25 and Figure 3-26. The total cooling capacity is predicted fairly well in both cases, however, the surface temperature prediction results from the Living Lab #1 has some larger deviations from the measurements compared to the results from the Bowen test bed. The larger prediction errors is mostly due to the effect of parallel air system which provided heat to the space as a counter heating source. Since one of the thermocouples that is installed on the surface of the passive chilled beam's perforated panel is relatively close to the sidewall diffuser of the air system, this counter heating affected the temperature around the passive chilled beam and its surface temperature. The results from the Bowen test bed showed better predictions, since the baseboard heater, which is the counter heating source, has a smaller impact on the surface temperature of the passive chilled beam. Besides this, regression models shown in Eqs. (3.1) and (3.2) predict the convective and radiative performance of the passive chilled beam very well.

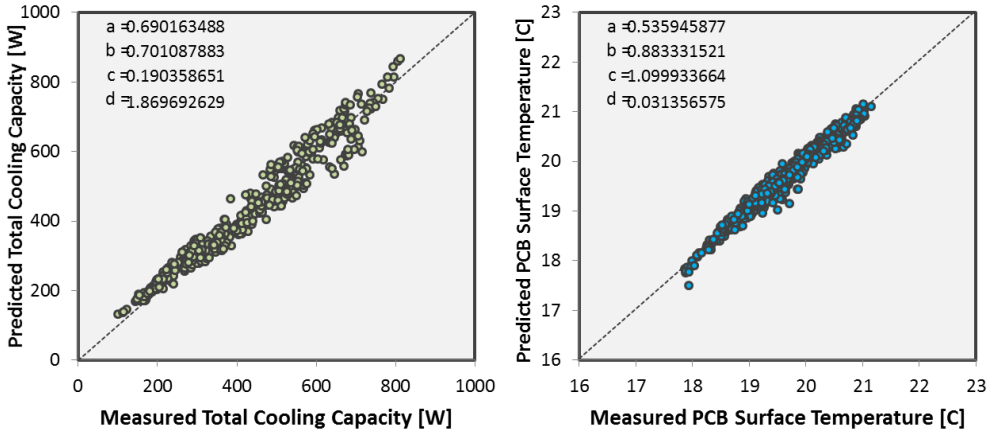

Figure 3-25. Comparison between measured and predicted model results with experiments from Bowen test bed.

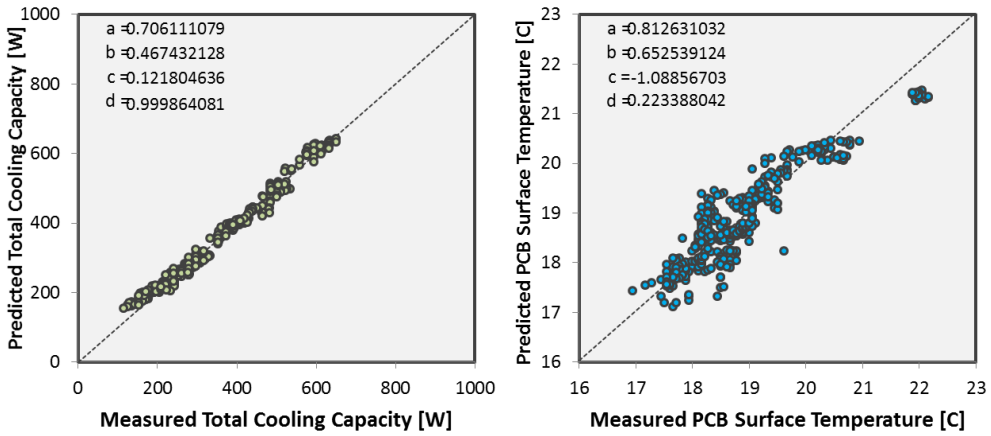

Figure 3-26. Comparison between measured and predicted model results with experiments from Living Laboratory.

3.2.2. Performance Comparison between Single and Multiple Chilled Beam Experiments

The standard practice of sizing a passive chilled beam system is to use the performance data acquired from single passive chilled beam testing. However, since natural convection is the primary driving force for the passive chilled beam's cooling, the cooling performance is not only affected by the chilled beam controllable parameters such as the water supply temperature and water flow rate but also by non-controllable indoor thermal conditions such as air temperatures below and above the passive chilled beam, local air movement and even indoor surface temperatures. This section attempts to verify whether it is appropriate to apply the single passive chilled beam testing result to an actual office with multiple passive chilled beams using results from the Bowen test bed and the Living Lab #1, as shown in Figure 3-27.

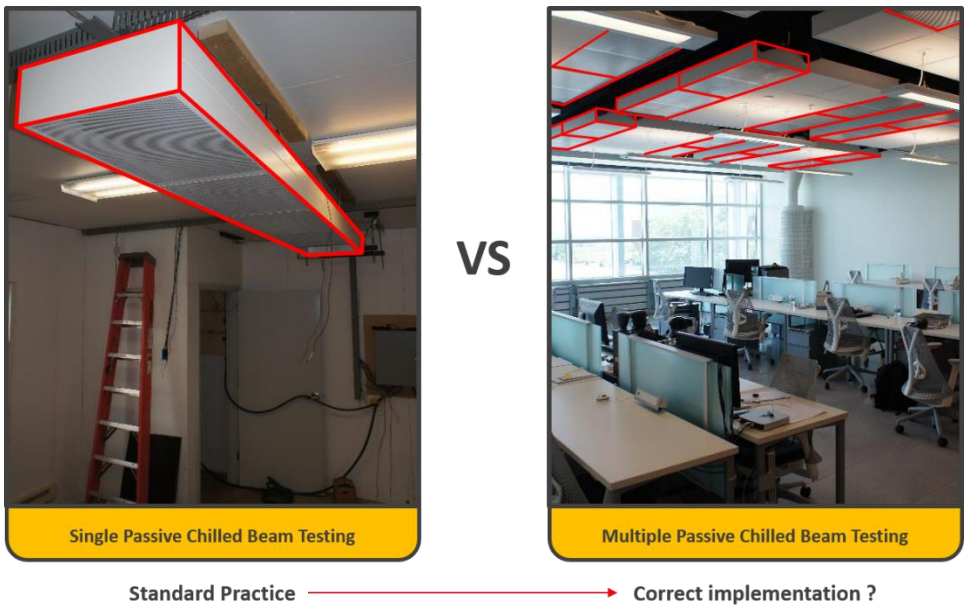

Figure 3-27. Comparison between two different chilled beam testing environments.

3.2.2.1. Performance Comparison Methodology

Comparing the performance of two passive chilled beams could be done just by comparing the regression model results shown in section 3.2.1. However, although the e passive chilled beams used in the Bowen test bed and the Living Lab #1 are the same make and model, they have different lengths as specified in Figure 3-6 and Figure 3-19. Thus, it is not fair to directly compare the total heat transfer rates for these two chilled beams. However, it is appropriate to compare the heat transfer rates per unit length if they have the same surface temperature and air inlet temperature. Figure 3-28 shows the comparison methodology used for these two passive chilled beams of different lengths that is based on achieving the average water temperature and air temperature above the chilled beam. The total cooling capacities per unit length are compared between two passive chilled beams by setting the air temperature above the passive chilled beam, water supply temperature and water return temperature the same. In this way, two passive chilled beams will maintain the same effective temperature which will drive the natural convection. The longer passive chilled beam is operated with higher water flow rate compared to the shorter passive chilled beam in order to achieve the same water outlet

temperature. In the comparison, the regression model shown in Figure 3-26 was used to represent the shorter passive chilled beam's performance, while additional measurements were taken in the Bowen test bed to represent the longer passive chilled beam's performance. Since the manufacturer of this passive chilled beam provides a software tool [124] which can also provide the total cooling capacity based on operating parameters, the software prediction is also included in the comparison.

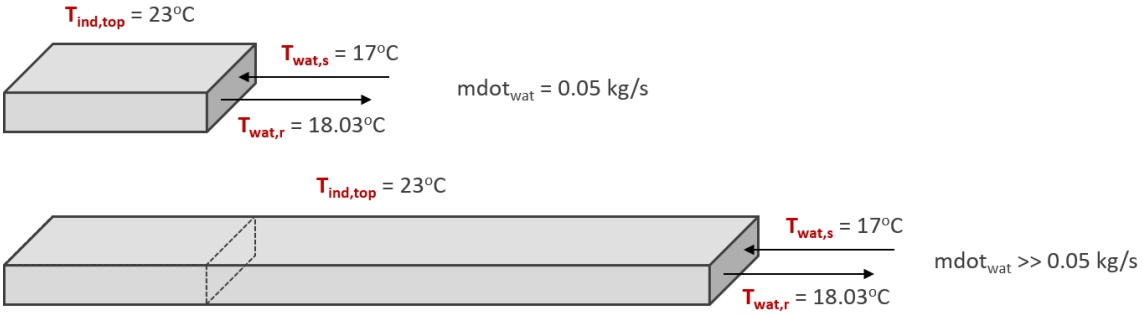

Figure 3-28. Comparison between two different lengths of passive chilled beams.

3.2.2.2. Performance Comparison Result

Figure 3-29 shows total cooling capacity predictions and measurements of a single passive chilled beam from the three different sources (Living Lab #1 regression model, Bowen test bed measurements and manufacturer's catalog) for three different water supply temperatures (16°C, 17°C and 18°C). Predictions from the Living Lab #1 model and catalog are based on 0.05 kg/s of the water flow rate and the Bowen measurements were determined by setting the water return temperature to the value determined from the Living Lab model. From these results, the total cooling capacity prediction with the Living Lab's regression model shows higher predictions by an average of 28% (35 W) compared to the Bowen test bed measurement. The prediction of the manufacturer's catalog is relatively closer to the Bowen test bed measurement, but still over-predicts performance for most of the operating conditions. Figure 3-30 shows field measurement results for 53 consecutive days (August 7th to September 29th 2016) that is described in section 4.1 which include cooling load measurements of the cooling coil and passive chilled beams in the Living Lab #1 and the cooling coil in the Living Lab #2. The circle

markers indicate the maximum and minimum values of each variable during the measurement period. Since the Living Lab #1 has 30 passive chilled beams installed in the office, the average performance difference of 35 W per passive chilled beam becomes 1050 W for the office. And based on Figure 3-30, this is 10% of the peak load and close to 75% percentile of the load that passive chilled beam takes during the cooling season in West Lafayette, Indiana.

The results described above indicate that the total cooling capacity of the passive chilled beam system can be underestimated if the typical sizing method is used. The Living Lab #1's passive chilled beams are designed based on the typical sizing method according to the manufacturer's performance data. During the summer cooling season (August 7th to September 29th 2016), the minimum water supply temperature ($T_{wat,s}$) to the passive chilled beams was measured as 17^{o}C as shown in Figure 3-30. Since the lowest temperature that can be reached is around 14^{o}C, it is also possible to handle the summer cooling load properly with less number of passive chilled beams under these conditions. Due to the physical characteristics of natural convection, the reason for the differences between the Bowen and Living Lab chilled beam performance could be related to differences in the available area above the chilled beam, local air movement driven by the parallel air system and/or internal gains. The specific reasons and remedies for the different behavior of laboratory and in-situ passive chilled beam performance should be considered in future studies in order to develop better design approaches.

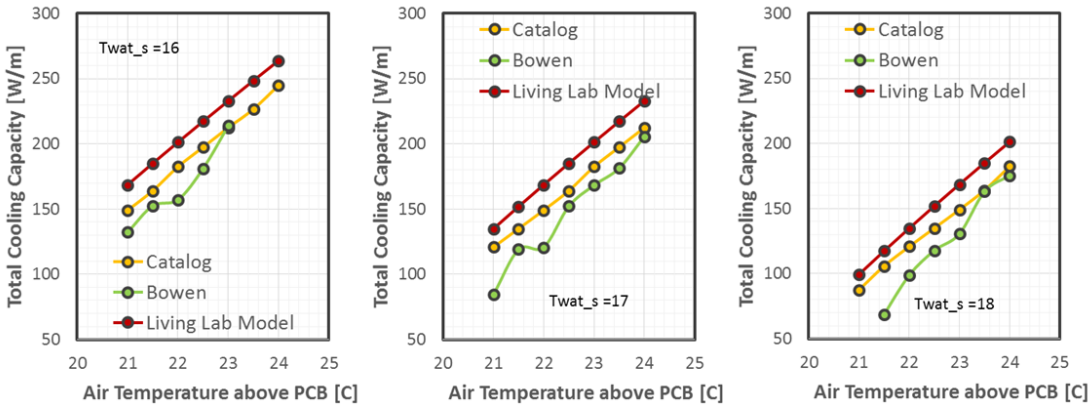

Figure 3-29. Performance comparison between single passive chilled beam testing and multiple passive chilled beams testing.

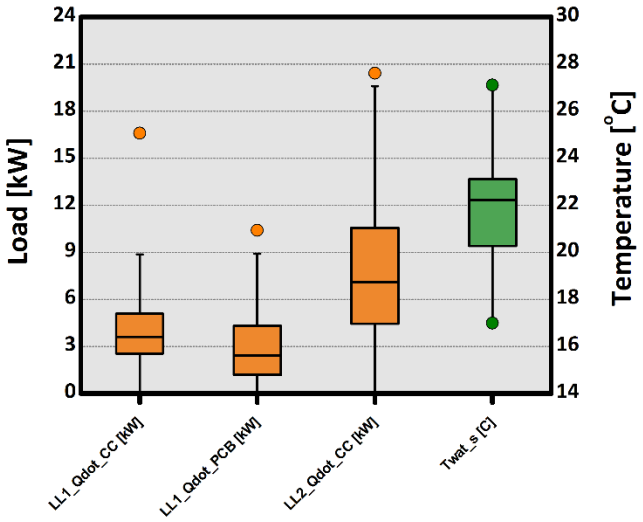

Figure 3-30. Cooling load measurement during cooling season.

3.2.3. Uncertainty Analysis

It is important to verify measurement errors associated with sensors that are used in the experiments and how those affect the calculation of additional parameters. Propagation of uncertainties in experimental measurements are estimated based on the specifications of sensors in this section. Dependent parameters such as area-weighted uncooled surface temperature (*AUST*), mean radiant temperature (T_{MRT}), operative temperature (T_{OPR}) and cooling capacity of the passive chilled beam ($\dot{Q}_{PCB}$) are calculated with independent parameters that were measured during the experiment. Each dependent parameter (P) can be calculated with multiple independent parameters (x) as shown in the equation below.

$$P = P(x_1, x_2, \cdots, x_n) \tag{3.3}$$

and the uncertainty propagation can be calculated as follows [125],

$$\mu_P = \sqrt{\left(\frac{\partial P}{\partial x_1}\mu_1\right)^2 + \left(\frac{\partial P}{\partial x_2}\mu_2\right)^2 + \cdots + \left(\frac{\partial P}{\partial x_n}\mu_n\right)^2} \tag{3.4}$$

where μ_P is the uncertainty of the dependent parameter and μ_1 to μ_n are the uncertainty of each independent parameter. Based on equation shown above and specifications shown in Table 3-1 and Table 3-3, uncertainties of dependent parameters are calculated as shown in Table 3-5. For example, the uncertainty of the *AUST* measured in the Living Lab which is calculated with each surface area of indoor surfaces, their temperatures and surface emissivity is calculated as ±0.3°C. All the other dependent parameters also show reasonable uncertainties.

Table 3-5. Uncertainty propagation of dependent parameters.

Independent Parameters		Independent Parameters		Independent Parameters		Independent Parameters		Independent Parameters		Independent Parameters	
$A_{surf,floor}$	103.65	$A_{surf,floor}$	28.28	ε_{glb}	0.9	T_{air}	23	$\dot{m}_{wat}$	0.05	$\dot{m}_{wat}$	0.11
$A_{surf,west}$	31.97	$A_{surf,west}$	14.19	D_{glb}	0.15	T_{opr}	23	$c_{p,wat}$	4190	$c_{p,wat}$	4190
$A_{surf,east}$	31.97	$A_{surf,east}$	14.19	v_{air}	0.1	γ	0.5	$T_{wat,s}$	15	$T_{wat,s}$	16
$A_{surf,north}$	30.12	$A_{surf,north}$	14.96	T_{glb}	23			$T_{wat,r}$	16.5	$T_{wat,r}$	17.04
$A_{surf,south}$	30.12	$A_{surf,south}$	14.96	T_{air}	22.5						
ε_{surf}	0.9	ε_{surf}	0.9								
T_{floor}	23	T_{floor}	23								
$T_{surf,west}$	23	$T_{surf,west}$	23								
$T_{surf,east}$	23	$T_{surf,east}$	23								
$T_{surf,north}$	23	$T_{surf,north}$	23								
$T_{surf,south}$	23	$T_{surf,south}$	23								
$AUST_{LL}$		$AUST_{Bowen}$		$T_{MRT,LL}$		$T_{OPR,LL}$		$\dot{Q}_{PCB}$		$\dot{Q}_{PCB}$	
Value	23.0°C	Value	23.0°C	Value	23.3°C	Value	23.0°C	Value	314 W	Value	479 W
$\mu_{AUST,LL}$	0.3°C	$\mu_{AUST,Bowen}$	0.2°C	$\mu_{TMRT,LL}$	0.2°C	$\mu_{TOPR,LL}$	0.2°C	$\mu_{Qdot,LL}$	59 W	$\mu_{Qdot,Bowen}$	81 W
Percentage	1.2%	Percentage	1.0%	Percentage	1.1%	Percentage	0.8%	Percentage	19%	Percentage	17%

CHAPTER 4. EXPERIMENTAL INVESTIGATION AND MODELING OF CONVENTIONAL AIR SYSTEM AND PASSIVE CHILLED BEAM SYSTEM

In the previous chapter, the passive chilled beam's performance was analyzed at the component level, with performance prediction models derived from experiments. A system-level analysis of the passive chilled beam system is performed in this chapter with experiments and simulations for overall assessment of the system. Two different side-by-side field measurements were conducted for comparing conventional air systems (constant air volume system and variable air volume system) with the passive chilled beam system. The radiation cooling effect of passive chilled beams is also assessed with field measurement comparisons. Findings that will help future implementation of the passive chilled beam system are also discussed. The whole building energy simulation model is developed and validated for an extended application study in the following chapter.

4.1. Experimental Comparison of Passive Chilled Beam System and Conventional Air Systems

This section includes a side-by-side field measurement comparison between a conventional air system and a passive chilled beam system. These field measurements are conducted in two adjacent Living Laboratory offices (Living Lab #1 and #2) at the Herrick Laboratories as shown in Figure 4-1 and Figure 4-2. In Figure 4-2, the photo on the left is the office equipped with the passive chilled beam system that was discussed in section 3.1.2.1. The photo on the right is an office equipped with conventional air system which can either operate as a constant air volume (CAV) system or variable air volume (VAV) system. The two offices are adjacent and have the same façade facing south.

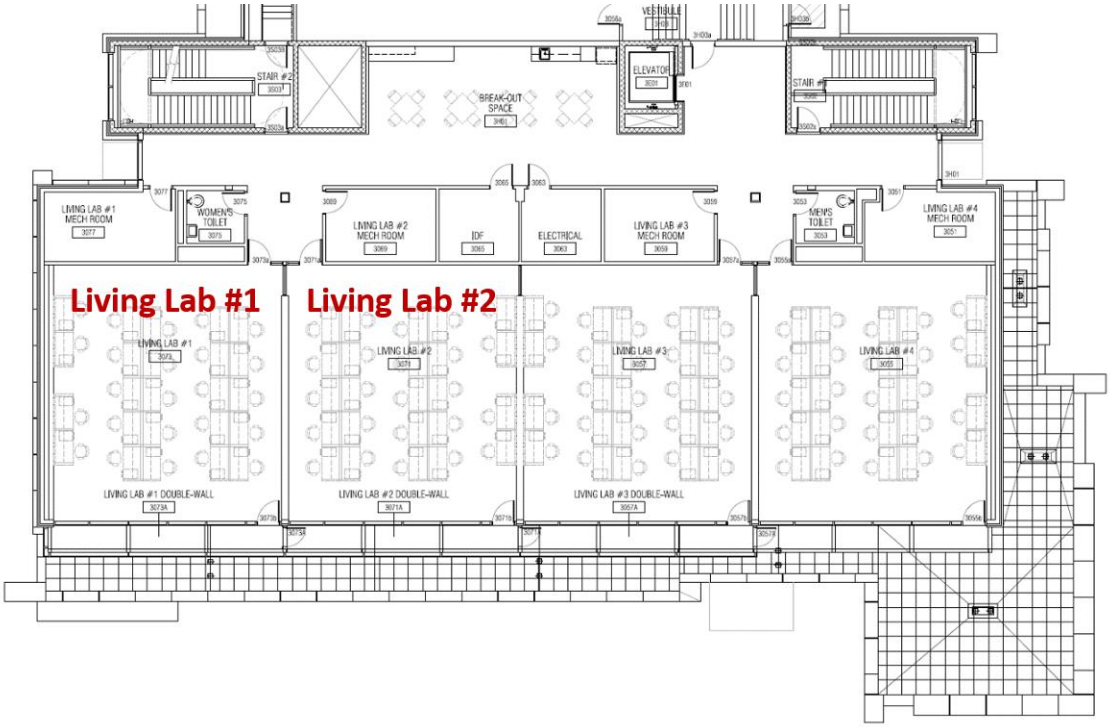

Figure 4-1. Plan view of the Living Laboratories at the Herrick Laboratories.

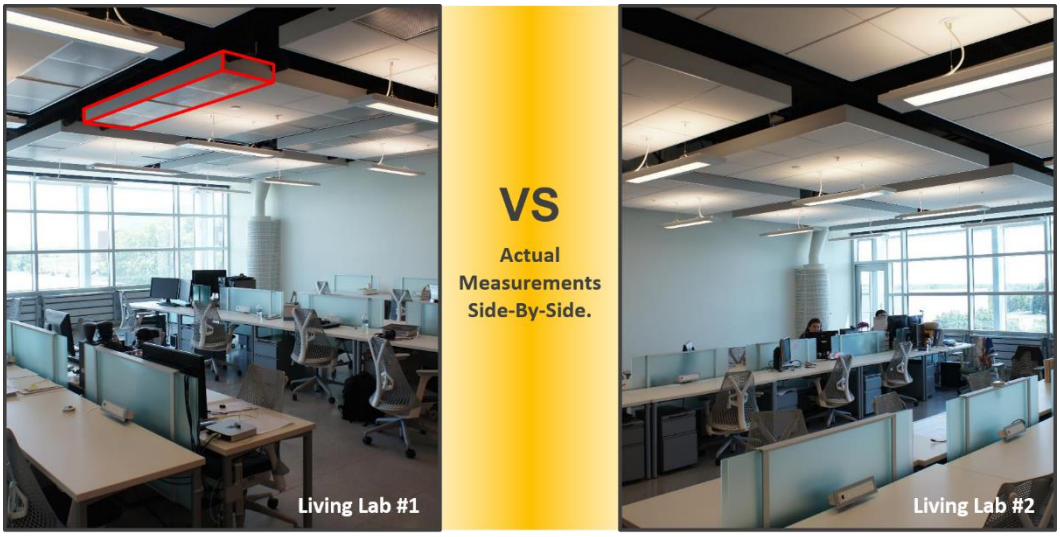

Figure 4-2. Concept of side-by-side field measurements in the Living Laboratories.

Both Living Laboratory offices are equipped with a separate air handling unit (AHU) as shown in Figure 4-3. This AHU includes supply and return fan, pre-heating coil, cooling coil, reheat coil, outdoor air and return air damper system, humidifier and an air filter. As

shown in the figure, there are sensors in different locations for measuring the condition and performance of the AHU. Since this experiment is focusing on space cooling rather than heating, components such as the pre-heating coil and reheat coil in the AHU are not used during the field study. Figure 4-4 shows the VAV box which is also separately installed in each Living Laboratory office. For this experiment, only two (connected to the overhead air distribution system) of four VAV boxes installed in the Living Lab #2 are used.

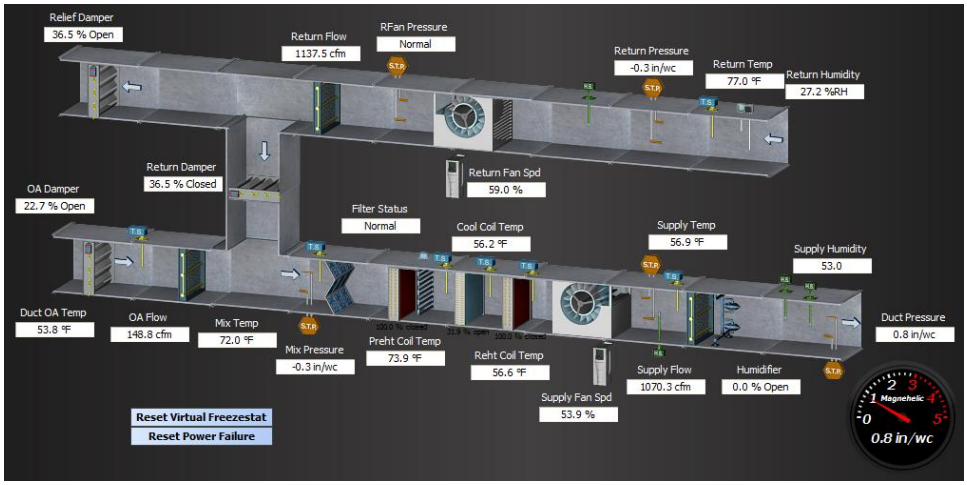

Figure 4-3. Schematic of the air handling unit in Living Laboratories.

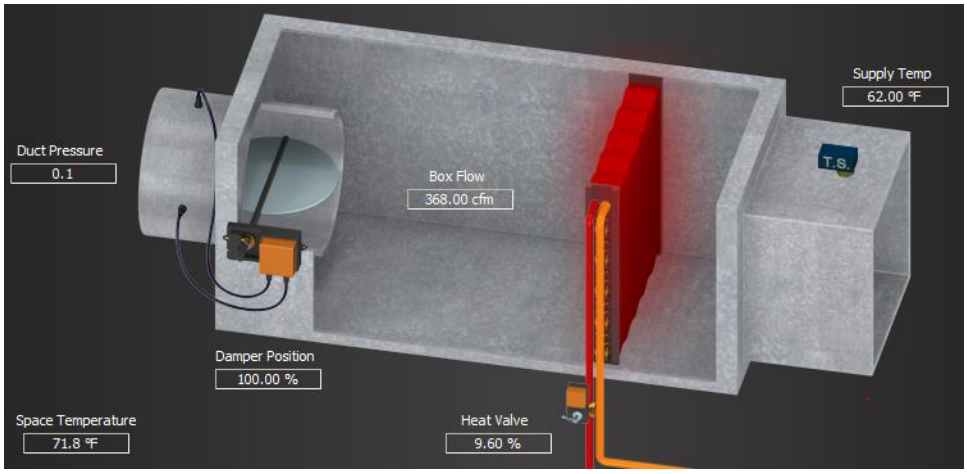

Figure 4-4. Schematic of the VAV box in Living Laboratories.

In order to fairly compare the energy consumptions between offices, the Living Lab #1 and #2 should maintain a similar thermal environment during the field measurement. In this field measurement, the operative temperature is used as the reference temperature for maintaining space thermal conditions. The operative temperature is a temperature reflecting both the convection and radiation effect in the space and it can be calculated as shown below [126].

$$T_{opr} = \gamma \cdot T_{ind} + (1-\gamma) \cdot T_{MRT} \tag{3.5}$$

where:

$$T_{MRT} = \left[\left(T_{\mathrm{glb}} + 273 \right)^4 + \frac{1.1\times10^8 \cdot v_{air}^{0.6}}{\varepsilon D^{0.4}} \left(T_{\mathrm{glb}} - T_{ind} \right) \right]^{0.25} - 273 \tag{3.6}$$

$$\gamma = \begin{cases} 0.5 & \text{if } v_{air} \le 0.2 \text{ m/s} \\ 0.6 & \text{if } 0.2 < v_{air} \le 0.6 \text{ m/s} \\ 0.7 & \text{if } 0.6 < v_{air} \le 1.0 \text{ m/s} \end{cases} \tag{3.7}$$

As in Eq. (3.5), the operative temperature (T_{opr}) can be calculated with the indoor drybulb air temperature (T_{ind}), mean radiant temperature (T_{MRT}) and weighting factor (γ). The weighting factor is determined by Eq. (3.7) and depends on local air speed (v_{air}). The mean radiant temperature can be calculated in different ways, however, for this field measurement, a globe thermometer is used to measure the globe temperature (T_{glb}) shown in Eq. (3.6) to calculate the mean radiant temperature. Globe thermometers were installed in each office as shown in Figure 4-5. Although the globe thermometer measurement only represents the local part of the office, an assumption is made that the condition in the center of the office represents the condition of the entire space. All the other sensors used for the field measurements are described in section 3.1.2.1 and are listed in Table 3-3.

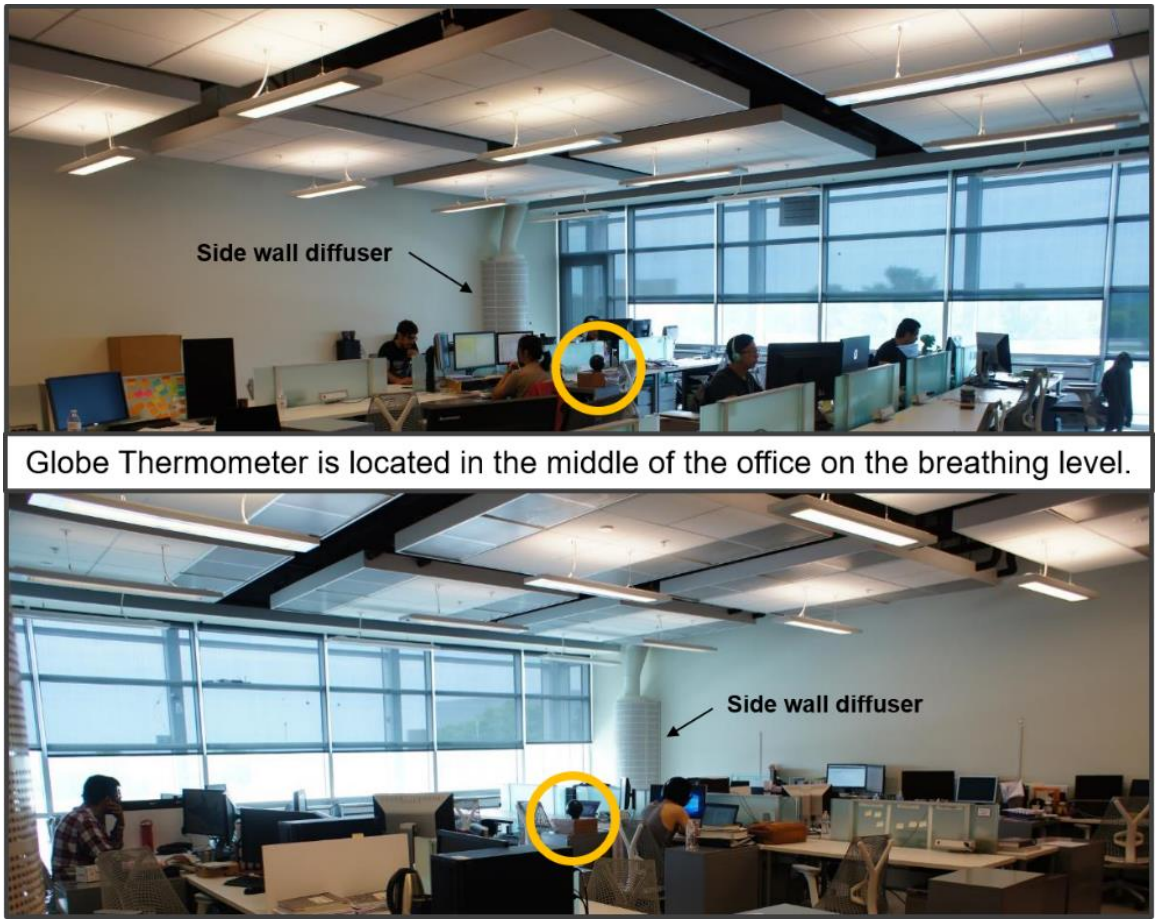

Figure 4-5. Locations of the globe thermometers in offices.

The local air velocity (v_{air}) term in Eq. (3.6) is assumed fixed and was measured in Living Lab #1 and #2 as shown in Figure 4-6. The figure contains five different measurement points (center, south-east, south-west, north-east and north-west) in each Living Lab with at least two hours of continuous measurements averaged every 10 minutes during the cooling operation. Although a conventional air system is expected to have higher average air velocity compared to the passive chilled beam system, the average air velocity of the conventional air system is measured as 0.05 m/s while the passive chilled beam system is measured as 0.09 m/s. This is mostly because of the side-wall diffuser that is used in the Living Labs as shown in Figure 4-5. Instead of having a typical overhead diffuser, this diffuser provides lower air velocity by having a larger diffuser area with perforated holes.

These two average air velocity values are used to calculate the mean radiant temperature in Eq. (3.6).

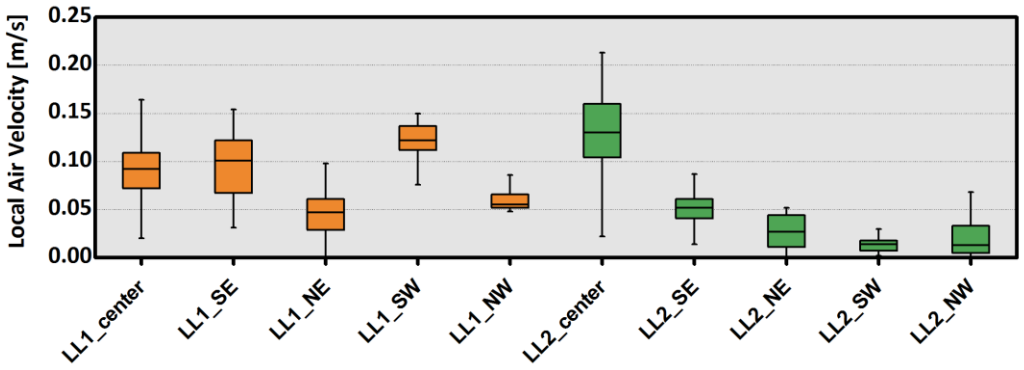

Figure 4-6. Local air velocity measurements in offices.

4.1.1. Passive Chilled Beam System versus Constant Air Volume (CAV) System

4.1.1.1. Configuration of CAV System and the passive chilled beam system

Table 4-1 shows the configurations of the CAV and passive chilled beam systems. The pre-heating coil and reheat coil in the AHU are not used in both systems. To operate this HVAC system in the Living Lab #2 as a CAV system, the flow rate of the supply fan is fixed at a constant value (900 CFM) based on the peak cooling demand. Since the flow rate is fixed with a fixed cooling coil air outlet temperature (based on peak dehumidification demand) from the AHU, the reheat coil in the VAV box is modulated to maintain the office temperature setpoint when the cooling load is relatively less. Passive chilled beams are used for handling sensible load only, thus the thirty passive chilled beams in the Living Lab #1 were modulated to maintain the space temperature setpoint. The water supply temperature and the water flow rate are both controlled to modulate the cooling power of passive chilled beams. PID controllers for controlling the water temperature and flow rate are tuned differently in order to use the water temperature more aggressively than the flow rate to meet the space sensible cooling demand. This control strategy was tested beforehand and implemented to reduce the risk of passive chilled beams overcooling due to their thermal mass which is discussed in detail in section 4.1.4.1. Dehumidification control is also an important part of using the passive chilled beam system. Since Living Lab #1 is equipped with a conventional AHU,

the cooling coil handles the latent load requirement. In order to meet the latent load variation more efficiently, two different reset control strategies are implemented. First, the cooling coil air outlet setpoint temperature is reset linearly between 10-12.2^{o}C (50-54^{o}F) according to the space relative humidity between 50-55%. Since this reset control turned out to be insufficient to meet the peak latent load demand, additional reset control was implemented, so that the air flow rate is increased from 200 CFM to 400 CFM when the space relative humidity reaches 58%. The VAV box in Living Lab #1 is only used when there is heating demand during night time.

Table 4-1. Configurations of the CAV and the passive chilled beam systems.

	Constant Air Volume (CAV) System	**Passive Chilled Beam System**
Pre-heating Coil	not used	
Cooling Coil	cooling coil air outlet stpt 54F	air outlet stpt reset (indoor RH 50-55% → 54-50F)
Reheat Coil	not used	
Supply Fan	supply fan constant 900CFM (including min. OA requirement)	two stage fan speed if RH < 53% → 200CFM/if RH > 58% → 400CFM
Return Fan	5% speed offset from supply fan	
VAV Box	modulate for reheat demand based on indoor temp stpt	enable if indoor temp < 72F
Passive Chilled Beam	not used	modulate for indoor temp stpt (temperature, flow rate)
Damper System	min. outdoor air requirement control & additional outdoor air when $T_{OA} < T_{RA}$	not used

4.1.1.2. Experimental results

4.1.1.2.1. Thermal Conditions in Offices

Field measurements were taken between August 14th and September 1st 2016. In order to focus on cooling demand conditions, fractions from the entire period of the field measurements, when the space operative temperature was maintained the same in both offices, were collected in post-processing. Figure 4-7 to Figure 4-9 show 164 hours of field measurements used for performance comparisons of the two systems. The x-axis in

all these figures matches with each other representing the time when the operative temperatures were mostly the same between Living Lab #1 and #2. As shown in Figure 4-7, the operative temperature (T_{opr}) in both offices was maintained fairly constant and similar to each other while the drybulb temperature varied relatively more in time. According to the ASHRAE Standard [127], the required outdoor air flow rate for both offices is 172 CFM. To provide enough ventilation to the space, 200 CFM was set for the minimum outdoor air rate. There were certain days when the relative humidity (*RH*) was not maintained properly in the Living Lab #1, as shown in Figure 4-7. After troubleshooting with the passive chilled beam system, supply temperature ($T_{air,AHU,s}$) reset and air flow rate ($\dot{V}_{air}$) reset strategies were implemented for the cooling coil in the Living Lab #1 as shown in Figure 4-8.

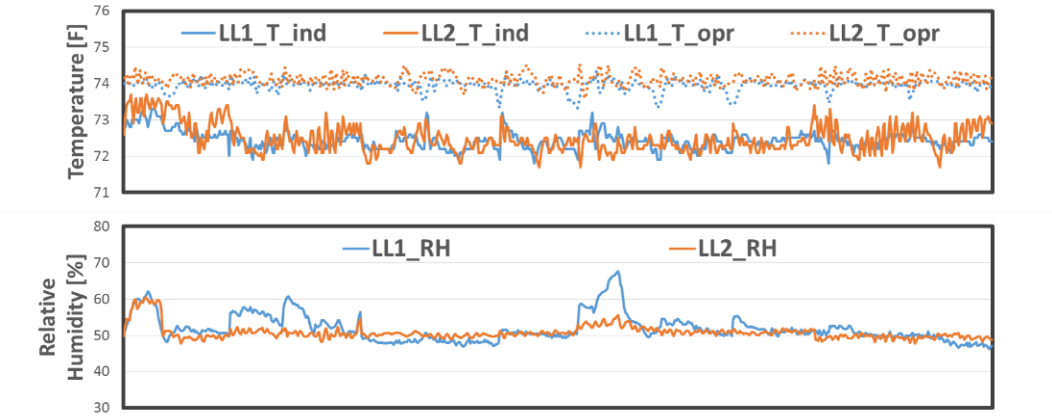

Figure 4-7. Field measurements of CAV system versus passive chilled beam system (1/3).

The passive chilled beam system was operated as a dedicated outdoor air system with 100% fresh air where the minimum outdoor air rate was set with 200 CFM also shown in Figure 4-8. When the air flow reset occurred due to increased latent load demand, additional outdoor air (maximum 400 CFM) was brought into the cooling coil. It is clear that using the damper system in the AHU by mixing with the return air will help to reduce extra load on the cooling coil when additional flow is necessary, however, the worst case scenario was tested as a starting point for this field measurement. Other configurations which will enhance the system efficiency will be covered in the computer simulation study in Chapter 5.

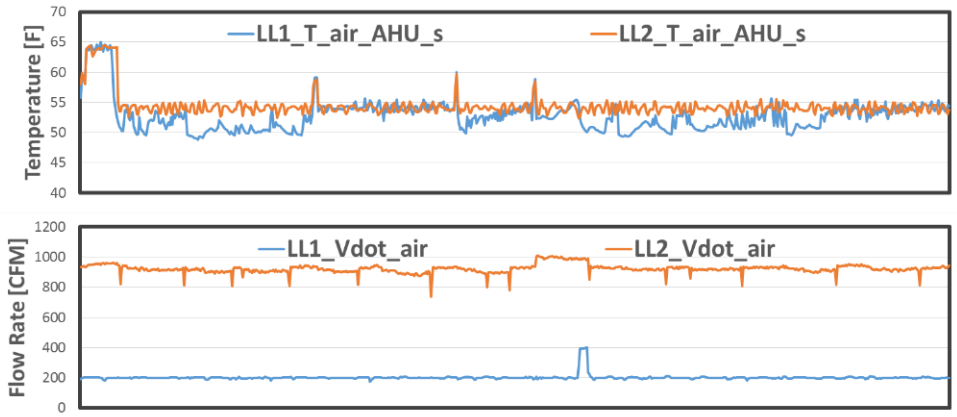

Figure 4-8. Field measurements of CAV system versus passive chilled beam system (2/3).

During the entire period of the field measurement, the water supply temperature ($T_{wat,s,PCB}$) to passive chilled beams varied according to the space cooling demand and the minimum water temperature reached 17.6°C (63.7°F) as shown in Figure 4-9. The cooling coil air outlet temperature ($T_{air,AHU,s}$) was set at 12.2°C (54°F) for the CAV system as shown in Figure 4-8. For the CAV system, the supply air flow rate ($\dot{V}_{air}$) was set as 900 CFM, shown in Figure 4-8, where the fresh air portion was 200 CFM controlled by the damper system.

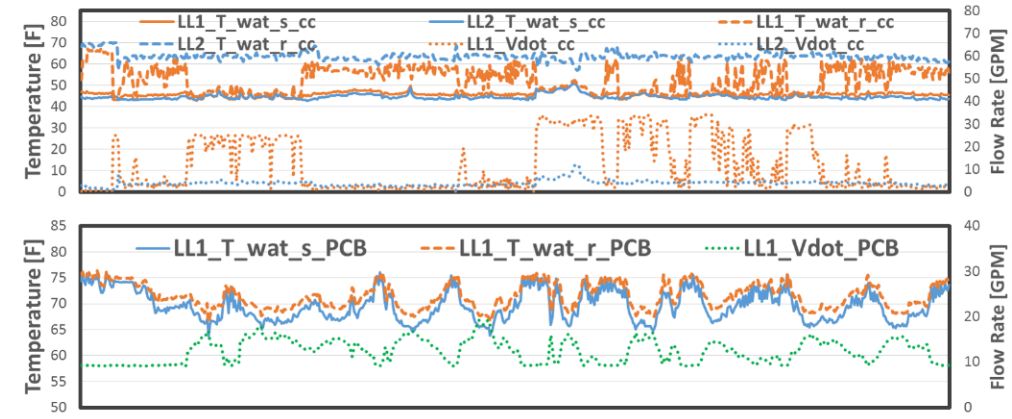

Figure 4-9. Field measurements of CAV system versus passive chilled beam system (3/3).

Based on the measurements shown in Figure 4-7 to Figure 4-9, thermal conditions in both spaces are rearranged as distribution curves shown in Figure 4-10. All six graphs show a certain thermal condition such as the drybulb temperature, operative temperature, predicted mean vote (PMV), predicted percentage of dissatisfied (PPD), relative humidity

and CO_2 level for both offices during the entire measurement period. The y-axis in all graphs are bin counts (×1000) which represents the number of data points that were remained in the corresponding x-axis value. Since the operative temperature is used as the reference temperature, both offices maintained almost similar operative temperature. PMV was maintained around -0.6 (which corresponds to 13% in PPD) scale and CO_2 level was maintained around 500 ppm over the ambient condition. Based on these measurements, it is fair to conclude that both offices maintained similar thermal conditions during the field measurement.

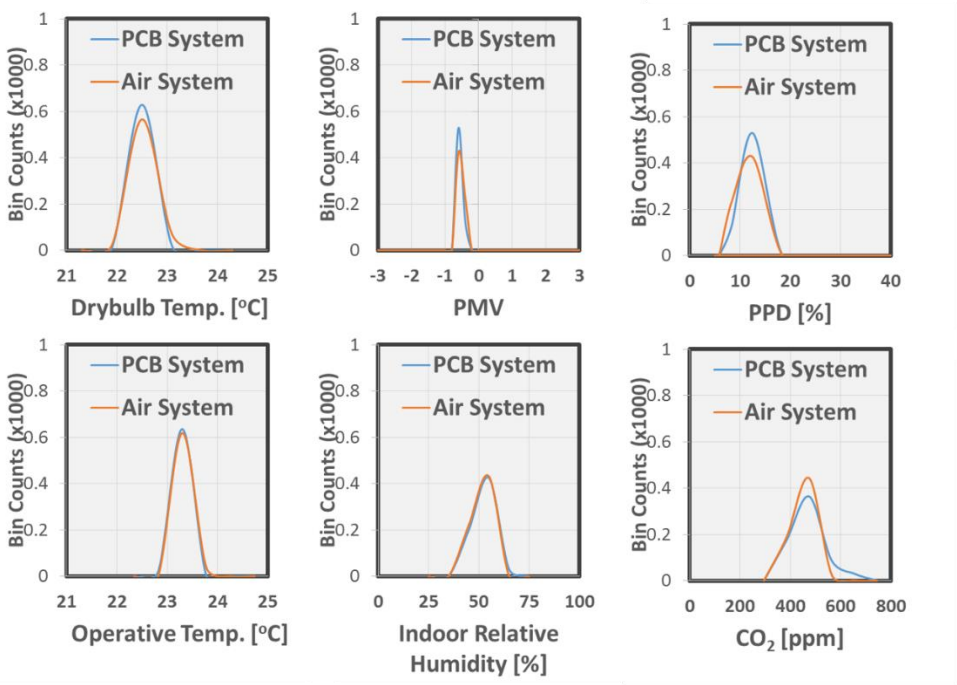

Figure 4-10. Thermal conditions in offices.

4.1.1.2.2. Energy Consumption comparison

Figure 4-11 shows energy consumption comparisons between the passive chilled beam system and the air system (the CAV system) that were determined using the available field measurements of 164 hours. The first graph on the left shows loads for the cooling coil, heating coil in the VAV box and passive chilled beams. While passive chilled beams covered 590 kWh of sensible load in the space, the remaining sensible and latent load

was covered by the cooling coil in the AHU. Since the CAV system uses fixed supply air flow rate with fixed supply air temperature, reheat is necessary except peak cooling periods. Thus the cooling coil load is higher for the CAV system as well as the load on the heating coil in the VAV box.

Purdue University provides district chilled water and steam around the campus through the pressurized water loop. For this reason, the cooling coil and the heating coil are controlled with valves rather than having an additional pump for the flow regulation. Since there is no pump dedicated to the cooling and heating coils, the comfort delivery equipment in the system are the supply and return fan and the water pump dedicated to passive chilled beams. The second graph in Figure 4-11 shows the electrical energy consumption of this comfort delivery equipment. As expected, the fan energy is greatly reduced in the passive chilled beam system and a total of 37% of electrical energy for the delivery system is saved in the passive chilled beam system after including the pump energy consumption.

In order to calculate the total energy consumption of each system, the energy that is consumed to provide cooling or heating energy to the cooling coil, heating coil and passive chilled beams should also be measured. However, the campus uses a centralized plant that provides chilled water and steam to hundreds of buildings on campus. The average COP for the campus chilled water system was assumed to be 5.5 for converting cooling load into chiller energy consumption in this study. In addition, 95% efficiency was assumed for converting heating load into boiler energy consumption. The graph on the right in Figure 4-11 shows the entire energy consumption of both systems and for each component. Compared to the energy consumed by the comfort delivery equipment, the chiller and boiler energy account for a much greater portion. The heating energy is also significant because of reheat related to the use of a CAV systems. Based on these results, the passive chilled beam can save significant energy compared to the CAV system. However, it is important to also evaluate savings in relation to a VAV system as described in the next section.

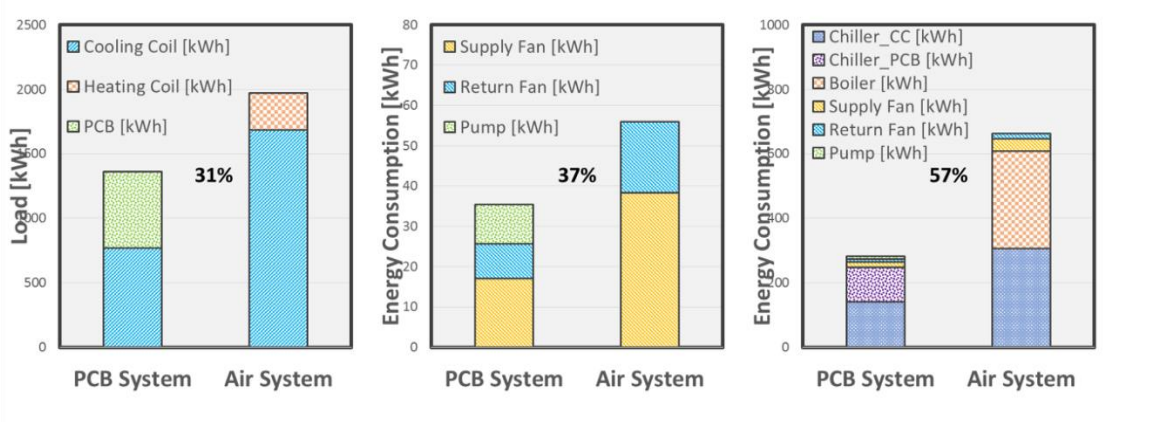

Figure 4-11. Summary of field measurement energy results.

4.1.2. Passive Chilled Beam System versus Variable Air Volume (VAV) System

4.1.2.1. Configuration of VAV System

Table 4-2 shows configurations and control approaches used for the VAV and passive chilled beam systems for this case study. The pre-heating coil and reheat coil in the AHU were not used in both systems. To operate this HVAC system in the Living Lab #2 as a VAV system, three different modifications were made. In this experiment, the supply fan was modulated from a minimum speed of 25% to maximum to maintain the space temperature setpoint. There were a few days when this minimum fan speed could not meet the demand, when the sensible load demand was small but the latent load demand was high. An additional control logic where the minimum fan speed is raised to 40% when the relative humidity in the space reaches 58% was implemented as well. VAV boxes in the VAV system and the passive chilled beam system were only operated when there was a heating demand during night time. The passive chilled beam system was configured as discussed in 4.1.1.1.

Table 4-2. Configurations of the VAV and the passive chilled beam systems.

	Variable Air Volume (VAV) System	**Passive Chilled Beam System**
Pre-heating Coil	not used	

Cooling Coil	cooling coil air outlet stpt 54F	air outlet stpt reset (indoor RH 50-55% → 54-50F)
Re-heat Coil	not used	
Supply Fan	modulate based on space temp & min. spd = if RH < 53% → 25% / If RH > 58% → 40%	two stage fan speed if RH < 53% → 200CFM/if RH > 58% → 400CFM
Return Fan	5% speed offset from supply fan	
VAV Box	enable if indoor temp < 72F	
Passive Chilled Beam	not used	modulate for indoor temp stpt (temperature, flow rate)
Damper System	min. outdoor air requirement control & additional outdoor air when $T_{OA} < T_{RA}$	not used

4.1.2.2. Experimental results

4.1.2.2.1. Thermal Conditions in Offices

Field measurements were taken between September 1st and September 27th 2016. In order to focus on cooling demand conditions, fractions from the entire period of the field measurements, when the space temperature was maintained the same in both offices, were collected separately. Figure 4-12 to Figure 4-14 show 200 hours of field measurements used for performance comparison of the two systems. The x-axis in all these figures matches with each other representing the time when the operative temperatures were mostly the same between Living Lab #1 and #2. The operative temperature (T_{opr}) in both offices was maintained fairly constant and similar to each other as shown in Figure 4-12. For this set of measurements, the relative humidity (*RH*) was maintained similar to each other and below 55% at all times shown in Figure 4-12. The significant drop of the relative humidity in the last part of the second graph shows the drastic weather change which almost ended the summer cooling testing.

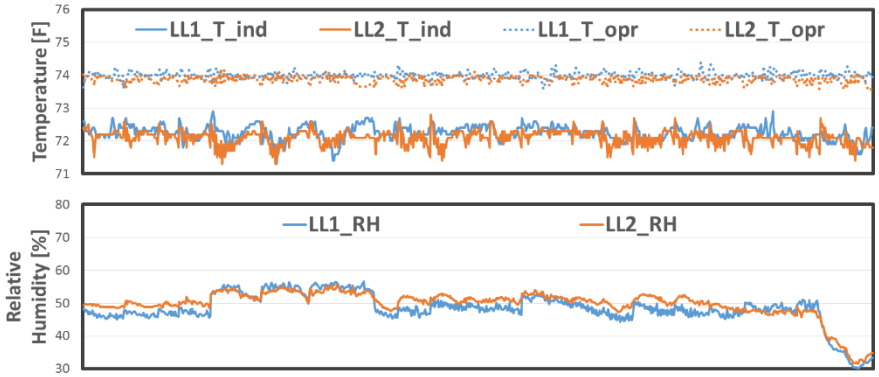

Figure 4-12. Field measurements of VAV system versus passive chilled beam system (1/3).

During this period of the field measurements, the minimum water temperature ($T_{wat,s,PCB}$) for the passive chilled beams reached 17°C (62.6°F) as shown in Figure 4-13. The supply air flow rate ($\dot{V}_{air}$) varied from 800 CFM to 1390 CFM in the VAV system to meet the space cooling demand as shown in Figure 4-14, and the 200 CFM out of the total flow rate was provided from the outdoor fresh air controlled by the damper system. During the early phase of the field measurements, the relative humidity (*RH*) in the Living Lab #2 seemed to be slightly higher than the Living Lab #1. Thus, as shown in the last part of the first graph in Figure 4-14, the cooling coil air outlet temperature setpoint was decreased to 10°C (50°F) to reduce the humidity level in the space.

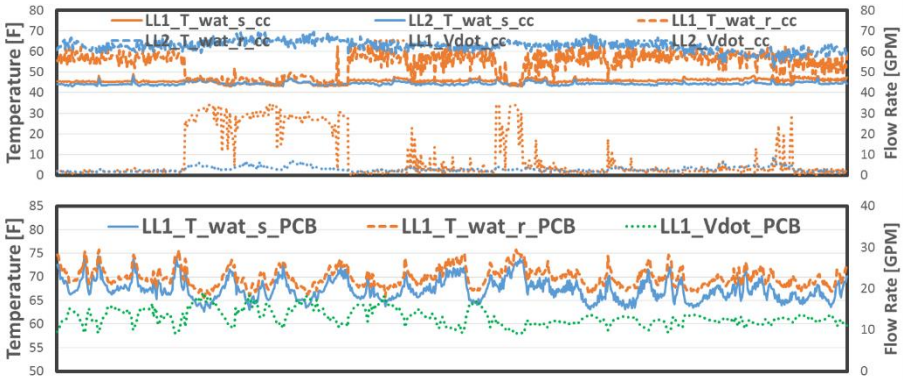

Figure 4-13. Field measurements of VAV system versus passive chilled beam system (2/3).

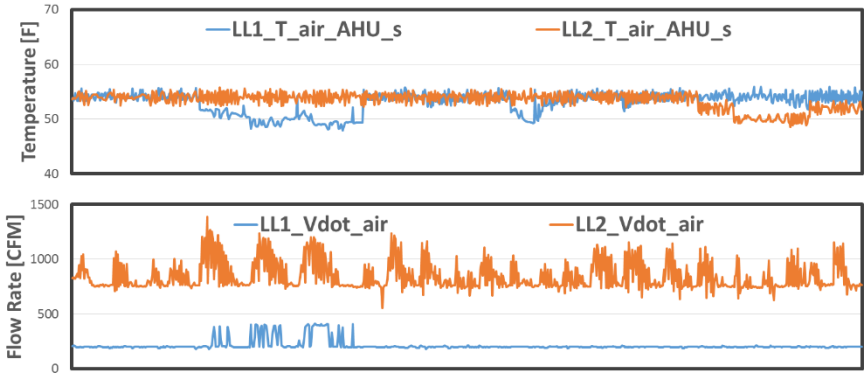

Figure 4-14. Field measurements of VAV system versus passive chilled beam system (3/3).

Based on the measurements shown in Figure 4-12 to Figure 4-14, thermal conditions in both spaces are rearranged as distribution curves shown in Figure 4-15. All six graphs show the same parameters shown in Figure 4-10. The y-axis in all graphs are bin counts (×1000) which represents the number of data points that were remained in the corresponding x-axis value. The operative temperature in both offices maintained almost similar with each other.

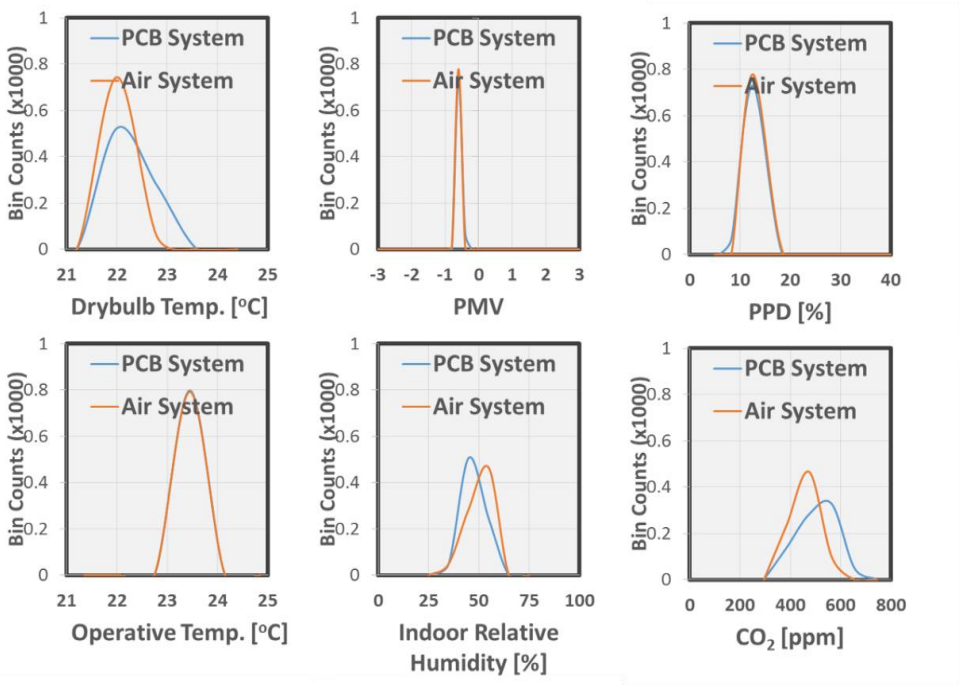

Figure 4-15. Thermal conditions in offices.

PMV was maintained around -0.6 which corresponds to 13% in PPD scale. While the CO_2 level distribution in the Living Lab #2 remained similar between results in Figure 4-10 and Figure 4-15, the distribution in the Living Lab #1 shows higher CO_2 levels as shown in Figure 4-15. Figure 4-16 shows the last 10 days of consecutive measurements when the VAV system and the passive chilled beam system were being compared. The outdoor air measurements ($\dot{V}_{OA}$) between the Living Lab #1 and #2 show that 200 CFM fresh air was provided most of the time besides when the economizer mode was shortly enabled during the night time. While almost the same amount of fresh air was provided to both offices, the CO_2 levels showed difference only in occupied hours as shown in the figure. And during unoccupied hours, CO_2 levels in both offices gradually became similar. Although the number of people staying in the office was not counted during the field measurements, it is expected that occupants' activity has caused the increase of CO_2 level in the Living Lab #1. Based on other measurements, it is fair to conclude that both offices maintained similar thermal conditions during the field measurements.

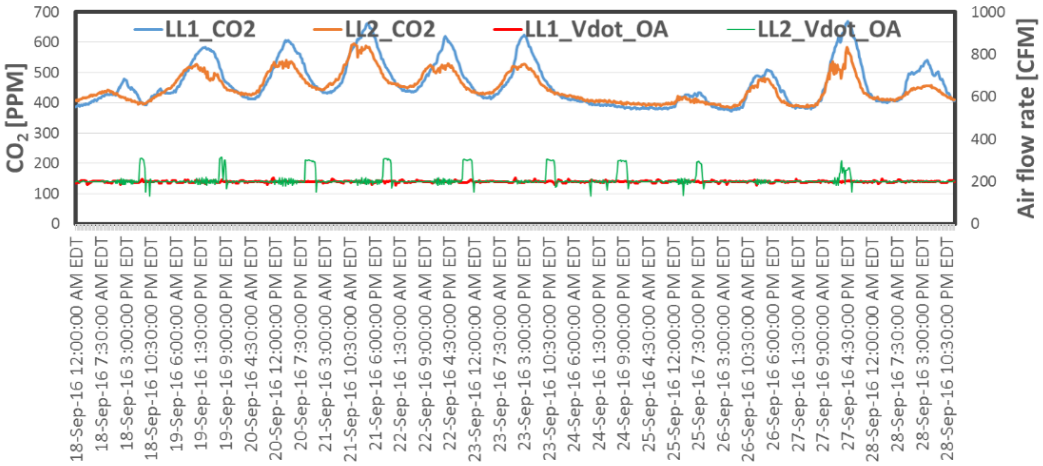

Figure 4-16. CO_2 level and outdoor air flow rate measurements.

4.1.2.2.2. Energy Consumption comparison

Figure 4-17 shows energy consumption comparisons between the passive chilled beam system and the air system (the VAV system) that were determined using the field measurements of 200 hours. The first graph on the left shows loads for the cooling coil and passive chilled beams. While passive chilled beams covered more than half of the cooling load in the space, the remaining sensible and latent load was covered by the cooling coil in the AHU. Compared to the CAV system, the VAV system handles the load more efficiently by modulating the fan speed according to the space cooling demand. Based on the field measurements, the cooling load of the VAV system was 22% less than that of the passive chilled beam system. The reason is that the cooling load might have increased in the passive chilled beam system by using the 100% outdoor air system and treating more fresh air than the VAV system when the latent load demand is high. Although the field measurements of the passive chilled beam system is performed without using the damper system in the AHU at all times for testing the worst case scenario, it is clear that using the damper system by opening up the return air damper when there is higher latent load demand and remaining the outdoor air fraction to minimum will handle the cooling load more efficiently. This improved scenario will be covered in the computer simulation in Chapter 5.

As shown in the graph in the middle in Figure 4-17, the comfort delivery equipment in the passive chilled beam system consumes more energy than the VAV system. Although the fan energy has been reduced compared to the VAV system, including the water pump dedicated to the passive chilled beams results in higher total energy consumption. However, based on the field measurement configuration, there is a room to reduce the water pump energy consumption while providing enough cooling energy to the space. This finding will be covered in detail in section 4.1.4.2.

The graph on the right in Figure 4-17 shows the entire energy consumption of both systems and for each component assuming a COP of 5.5 for converting the cooling load into chiller energy consumption and a 95% efficiency for converting the heating load into boiler energy consumption. The total energy consumption of the passive chilled beam system is about 21% larger than that of the VAV system for this case study. This is

primarily due to a larger load associated with the 100% dedicated outdoor air system. It does not reflect the potential for energy savings if alternative configurations and control strategies were considered. Alternative configuration and control scenarios are considered through computer simulation in Chapter 5.

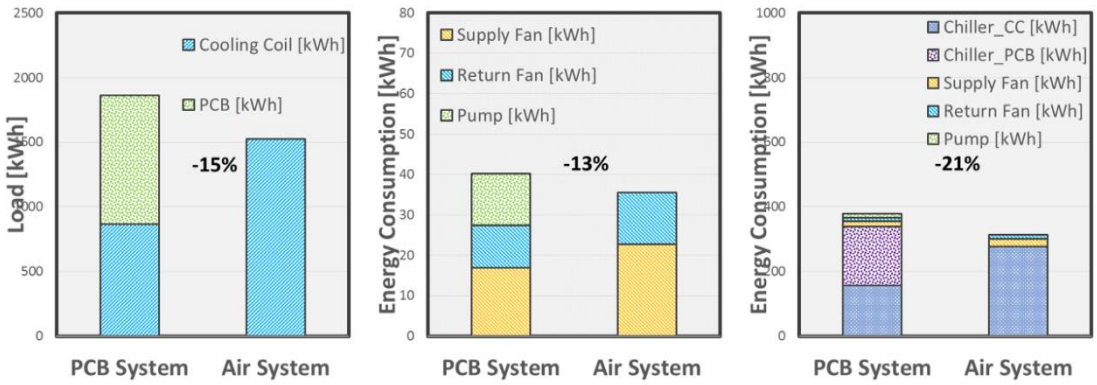

Figure 4-17. Summary of field measurements energy results.

4.1.3. Radiation Cooling Effect of Passive Chilled Beam System

One of the frequently asked questions for the passive chilled beam is whether the radiation cooling effect of passive chilled beams is significant. To answer this question, additional field measurements were conducted.

4.1.3.1. Methodology

The methodology of this additional study is to conduct side-by-side field measurements in Living Lab #1 and #2 by using either the operative temperature (Case 1) or the drybulb temperature (Case 2) as a reference for controlling the space condition. More specifically as shown in Figure 4-18, if the operative temperature is used (Case 1) as the reference temperature and if the radiation cooling of passive chilled beams is significant, the mean radiant temperature term in Eq. (3.5) will be lower in the passive chilled beam system than that of the air system. Thus, in order to maintain the same operative temperature, the indoor drybulb temperature can be relatively higher in the passive chilled beam system than that of the air system. If the indoor drybulb temperature is used (Case 2) as the

reference temperature, the mean radiant temperature term is no longer considered and the effect of radiation cooling is not captured. Thus, by comparing the relative savings between the field measurement results of Case 1 and 2, the difference will stand out only if the radiation cooling of passive chilled beams is significant.

Since field measurement using the operative temperature as reference temperature have already been summarized in section 4.1.1, additional field measurements were taken during the same cooling season using the drybulb temperature as the reference temperature.

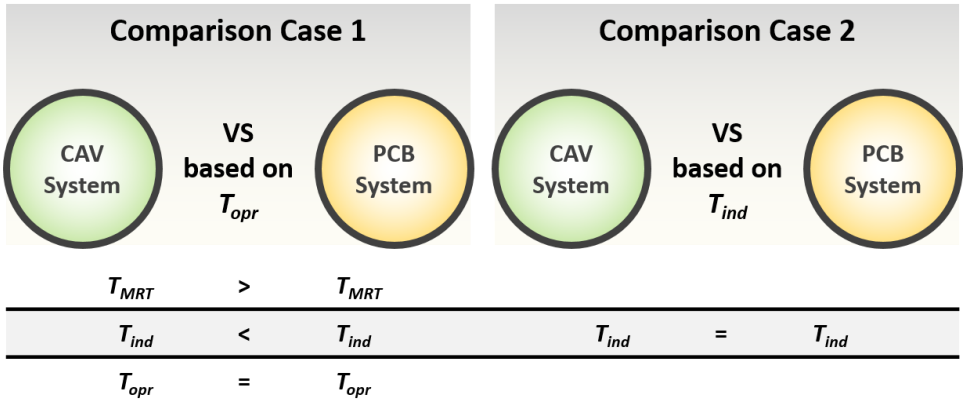

Figure 4-18. Methodology of quantifying the radiation cooling effect of passive chilled beams.

4.1.3.2. Experimental results

4.1.3.2.1. Thermal Conditions in Offices

The field measurements were taken between August 7th and August 30th 2016. Similar to the previous experiments, fractions of the monitoring period were selected when cooling demand was dominant and when the space temperature was maintained the same in both offices. Figure 4-19 to Figure 4-21 show 170 hours of field measurements used for the performance comparison of the two systems. The x-axis in all these figures matches with each other representing the time when the drybulb temperatures were mostly the same between Living Lab #1 and #2. Unlike Figure 4-7, the drybulb temperature (T_{ind}) in both offices was maintained fairly constant and similar with each other while the operative

temperature (T_{opr}) varied relatively more in time as shown in Figure 4-19. There was a cooling coil air outlet temperature ($T_{air,AHU,s}$) reset scheme during this set of field measurements as shown in Figure 4-20, however, it was removed during the early phase of the field measurements shown in section 4.1.1. The effect of this reset control is reflected in the relative humidity (*RH*) measurement and the air supply temperature ($T_{air,AHU,s}$) measurement in Figure 4-19 and Figure 4-20. However, this does not affect the relative performance differences between two systems. During this period of the field measurements, the water supply temperature ($T_{wat,PCB,s}$) to passive chilled beams varied according to the space cooling demand and the minimum water temperature reached 18^{o}C (64.3^{o}F) as shown in Figure 4-21.

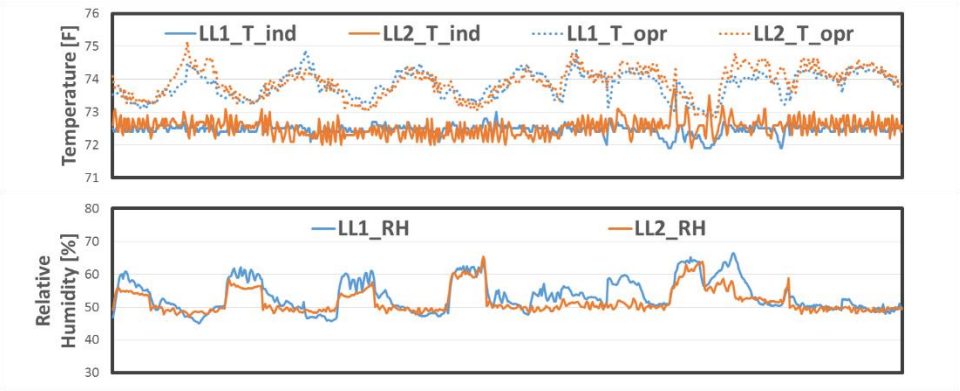

Figure 4-19. Field measurements of CAV system versus passive chilled beam system (1/3).

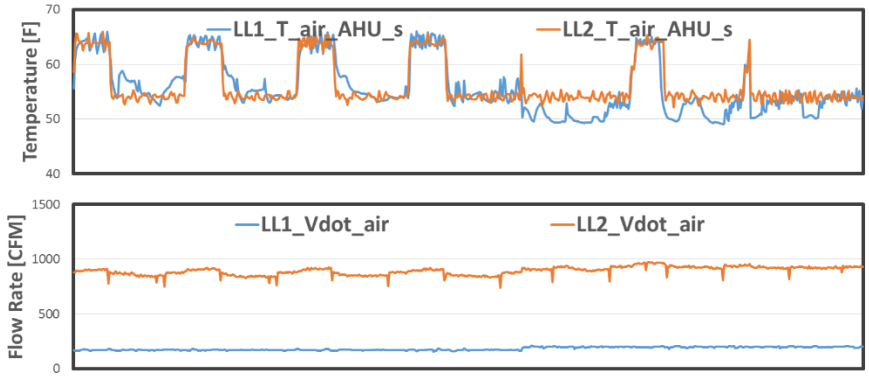

Figure 4-20. Field measurements of CAV system versus passive chilled beam system (2/3).

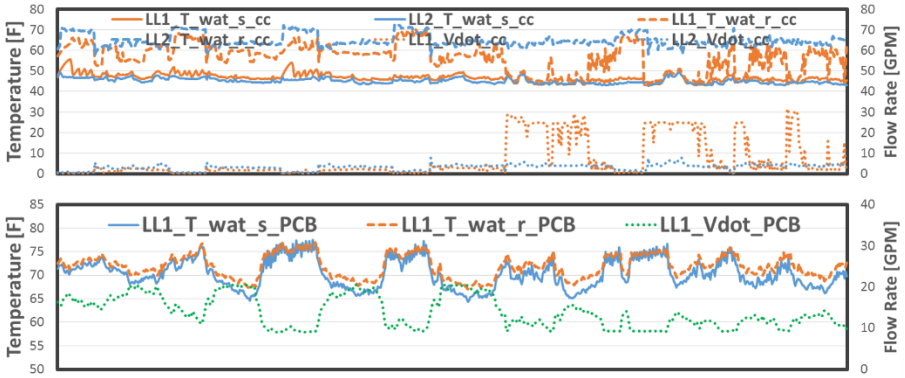

Figure 4-21. Field measurements of CAV system versus passive chilled beam system (3/3).

Based on the measurements shown in Figure 4-19 to Figure 4-21, thermal conditions in both spaces are rearranged as distribution curves in Figure 4-22. The y-axis in all graphs are bin counts (×1000) which represents the number of data points that were remained in the corresponding x-axis value. Compared to Figure 4-10 where the operative temperature is used as the reference temperature, the drybulb temperature distribution between offices shows better agreement with each other than the operative temperature. All the other measurements are similar to measurements that are shown in Figure 4-10. Based on these measurements, it is fair to conclude that both offices maintained similar thermal conditions during the field measurements while using the drybulb temperature as the reference temperature.

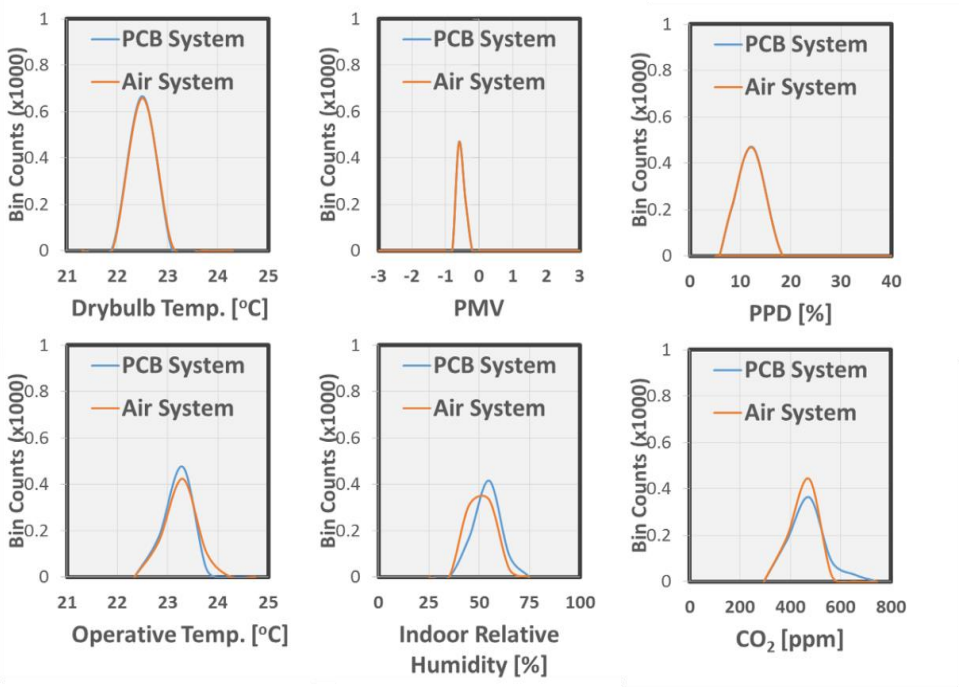

Figure 4-22. Thermal conditions in offices.

4.1.3.2.2. Energy Consumption comparison between Offices

Figure 4-23 shows the field measurement results in terms of energy consumption between the passive chilled beam system and the air system when the drybulb temperature is used as the reference temperature. Based on results of Figure 4-11 and Figure 4-23, it is easy to conclude that the relative savings between the CAV system and the passive chilled beam system are similar. Table 4-3 shows the summary between Case 1 (where the operative temperature is used as the reference temperature) and Case 2 (where the drybulb temperature is used as the reference temperature) field measurements. As shown in the table, the relative energy savings are very similar between the two cases. Additional verification of quantifying the effect of the radiation cooling of passive chilled beams with the computer simulation will be performed in Chapter 5. However, based on field measurements performed in this section, the radiation cooling effect of passive chilled beams is insignificant in terms of energy savings.

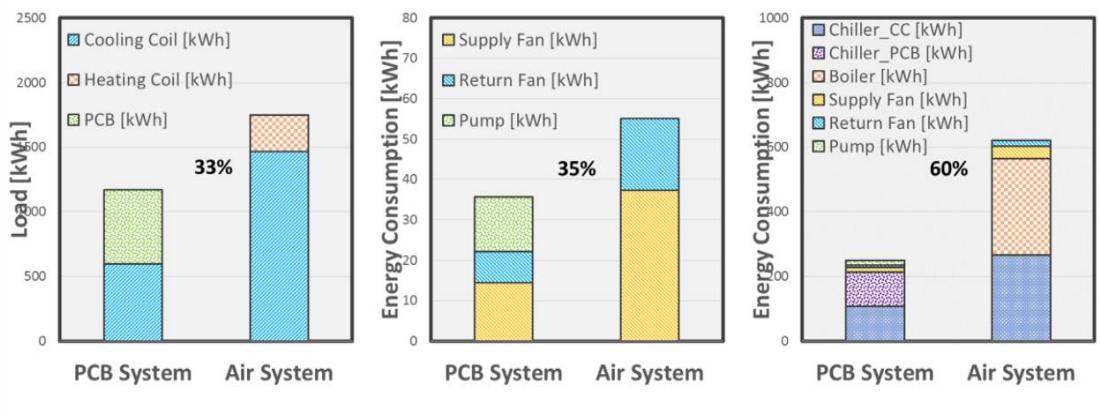

Figure 4-23. Summary of field measurements energy results.

Table 4-3. Field measurements results between two different reference temperature cases.

	Case 1 (T_{opr})		Case 2 (T_{ind})	
	PCB System	CAV System	PCB System	CAV System
Supply Fan [kWh/day]	2.5	5.6	2.0	5.3
Return Fan [kWh/day]	1.3	2.6	1.1	2.5
Pump [kWh/day]	1.4	0.0	1.9	0.0
Chiller $_{CC}$ [kWh/day]	20.5	44.9	15.3	37.7
Chiller $_{PCB}$ [kWh/day]	15.7	0.0	14.8	0.0
Boiler [kWh/day]	0.0	44.1	0.0	42.3
Total Energy Consumption [kWh/day]	41.5	97.2	35.2	87.9
Comfort Delivery Equipment Saving [%]	37%		35%	
Total Energy Saving [%]	57%		60%	

4.1.4. Additional Findings for Better Implementation of Passive Chilled Beam System

This section includes additional observations from the field study that could affect future implementations of passive chilled beam systems.

4.1.4.1. System Control Perspective

A control modification was made on the passive chilled beam system before the field measurement that was taken in section 4.1. Before this modification, the Living Lab #1 which is equipped with the passive chilled beam system had problems with maintaining the space temperature according to the setpoint. The major reason for this problem was

the thermal mass of 30 passive chilled beams installed in the office and the original control logic that was implemented. The original control strategy for the passive chilled beams involved modulating the water flow rate to the passive chilled beams according to the space cooling demand while the supply water temperature was kept constant around 58^{o}F (14.4^{o}C). However, during most of the time, reducing the water flow rate to zero still provided enough cooling energy to the space resulting in significant temperature drop in the space below the setpoint. This behavior caused severe oscillations of the temperature in the space where the system switched back and forth from cooling to heating mode. As a result, a modification was made to control both the water flow rate and water supply temperature to the passive chilled beams. Additionally, different tuning policies are applied in the PID controllers so that the water supply temperature can react faster to the space cooling demand than the water flow rate. This is mostly to keep the pump power at a minimum and take more advantage of the district chilled water with the valve control. There are two degrees of freedom (temperature and flow rate) of controlling passive chilled beams according to the space cooling demand. The field measurement showed that the thermal mass of the passive chilled beams is significant enough to cool down the space further below the setpoint. These two findings point out that further advanced control studies are needed, similar to studies that have been performed for radiant floor systems.

4.1.4.2. System Commissioning Perspective

The parallel air system that is installed in Living Lab #1 was commissioned based on the typical sizing method without considering the presence of the passive chilled beam system. Based on the fact that the most efficient way of using a passive chilled beam system is to have a dedicated outdoor air system with minimum 100% fresh air, the current air system is mostly oversized in Living Lab #1 in terms of using it as a parallel air system with passive chilled beams. This oversized system affected the energy consumption of the fan in the passive chilled beam system. Fans that are installed in AHUs in both Living Lab #1 and #2 have a low limit of operation. Therefore this variable speed fan can ramp up and down between 25 to 100% of the fan speed, however, it

cannot operate between 0 to 25% of the fan speed. During the field measurements, there was a period when the fan speed in both Living Labs was 25% while the Living Lab #1 was providing 200 CFM fresh air to the space and the Living Lab #2 was providing 800 CFM of mixed fresh and return air using a conventional AHU with outdoor and return air damper controls. The static pressure in the AHU of the Living Lab #1 was higher than that of the Living Lab #2 during this period which means there is room to reduce the fan speed in the Living Lab #1 below 25% with smaller size fan, but still providing enough conditioned air to the space.

Another issue that was noticed during the field measurements is related to the installation of passive chilled beams. 30 passive chilled beams in the Living Lab #1 are installed on modular clouds which are hung from the space ceiling as can be seen in Figure 4-5. These clouds are not rigidly held, so they are exposed to vibration. When water was flowing through passive chilled beams during operation, noise and vibration occurred at certain moments. Based on trial and error, the noise and vibration occurred when the water flow rate was around 0-30% or 80-100% of the maximum water flow rate of the system. Thus, a constraint was made in the control logic so that the water flow rate will only vary between 30-80% of maximum flow. However, this constraint made a base load of the water pump which can be seen in the second graph in Figure 4-9. Proper design and commissioning of the passive chilled beam system should improve this.

4.2. Integrated Model Development for Building Simulation

In Chapter 3, regression models of the passive chilled beam were developed based on experimental results. In order to perform whole-building energy simulations, all the other components of the system should be available as well. These other components include a thermal zone model, internal gain models and HVAC component models including a fan, pump, cooling or heating coil, chiller and AHU dampers and controls. In this section, the integrated model development and its validation which are necessary for performing whole-building energy simulation are described.

4.2.1. Building Envelope Parameters

The building envelope model is developed based on construction drawings of the Living Lab #1 as shown in Figure 4-24. The construction specifications of this envelope model are listed in Table 4-4. As shown in Figure 4-24, the thermal zone model is divided into three separate zones, including a double façade feature, acting as a buffer zone between external and internal windows, and a plenum space, where the return air is gathered and flows back to either the HVAC system or to the passive chilled beams. The detailed radiation model is selected in TRNSYS Type 56 to properly reflect the features of this thermal zone such as the double façade, the estimation of human comfort in the space and the radiation heat transfer between indoor surfaces and passive chilled beam surfaces. The surface between the plenum and the office area is mostly -but not fully- covered with nine cloud surfaces as shown in the office photo in Figure 4-5.

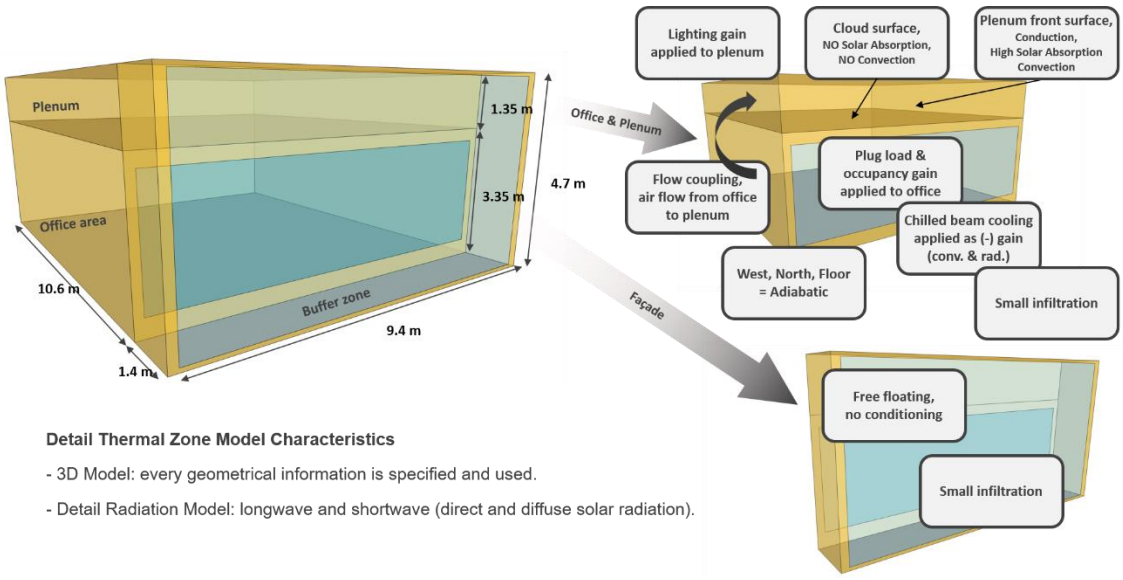

Figure 4-24. Assumptions of modeling the multi-zone thermal model.

Passive chilled beams are installed on these clouds, thus, when the passive chilled beam is in operation, the relatively warm air in the plenum is pulled into the passive chilled beams by natural convection, and the cooled air is pushed towards the office area. To approximate the temperature difference between the office area and the plenum due to thermal stratification and circulation, several assumptions were made as shown in Figure

4-24. First, the lighting gains in the space are applied in the plenum rather than in the office area. The only thermal coupling considered between the office zone and the plenum is due to forced convection. The total supply air flow rate from the diffusers is assumed to flow to the plenum but at the temperature and humidity of the office area. Heat transfer from the office zone to the cloud bottom surfaces was forced to be zero by setting the underside convection coefficient and solar absorption to zero. Solar heat gain to the top surface from the south facing windows is considered along with convective heat transfer between the plenum and clouds. However, the temperature within the clouds is considered to be uniform which was implemented by utilizing a very high thermal conductivity. All the other necessary assumptions are shown in Figure 4-24.

Table 4-4. Construction specifications of the thermal zone model.

Type	Layer Description	Thickness	U-Value
		m	W/m^2K
Roof	Insulation	0.1	0.221
	Concrete	0.038	
Raised Floor	Concrete	0.102	2.558
	Air	0.3	
External Wall	Gypsum Board	0.013	0.358
	Insulation	0.105	
	Stucco	0.025	
Internal Wall	Gypsum Board	0.016	1.894
	Air	0.184	
	Gypsum Board	0.016	
Window	Double glazing (ID: 7041)	5.7/6.4/5.7 (mm)	3.2
Internal Window	Double glazing (ID: 7002)	4.6/12/2.2 (mm)	1.58
Cloud	Massless surface	0	5.76
External Floor	Steel	0.1	5.66
Plenum South Panel	Insulation	0.06	0.598
	Steel	0.02	

4.2.2. Internal Gains and Thermal Comfort Parameters

Internal gains schedules for occupancy, lighting and plug loads were adopted from ASHRAE Standard 90.1 [128] as shown in Figure 4-25. These schedules represent typical load profiles of commercial buildings.

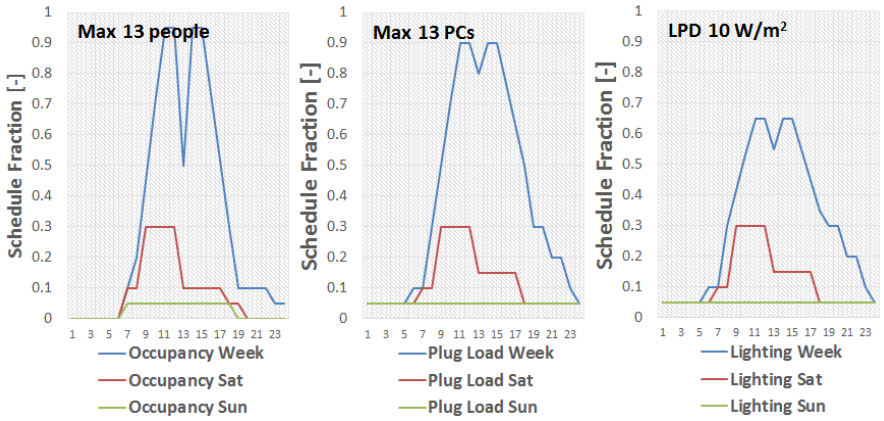

Figure 4-25. Specifications of internal gains and thermal comfort parameters.

Parameters related to thermal comfort calculations are listed in Table 4-5. The operative temperature calculation is adopted from the ASHRAE Standard 55 [126] where there is a different weighting factor between dry-bulb temperature and mean radiant temperature based on the relative air speed as shown in Eq. (3.5). In the simulation, mean radiant temperature is calculated as shown below.

$$T_{MRT}^4 = T_1^4 F_{p-1} + T_2^4 F_{p-2} + \cdots + T_N^4 F_{p-N} \tag{4.1}$$

T_1 to T_N represent interior surface temperatures in the office and F represents view factors between occupants and the interior surfaces. The view factor in the equation is adopted from the literature [129] and applied in the model as shown in Figure 4-26. Parameters that are necessary for the calculation of the Predicted Mean Vote (PMV) and Predicted Percentage Dissatisfied (PPD) are also listed in Table 4-5. All the parameters for PMV and PPD calculation are assumed to be the same except the relative air speed between the conventional and the passive chilled beam system. As was discussed in section 4.1, 0.09 m/s is used as the local air speed for the passive chilled beam system and 0.05 m/s for the

VAV system for the model validation. According to ASHRAE Standard 55, a conventional air system's maximum relative air speed can be limited to 0.2 m/s when the operative temperature is maintained below 23^{o}C. A passive chilled beam's relative air speed can vary based on the cooling power of passive chilled beams installed in the space. Based on an experimental study that focused on the air velocity field in terms of passive chilled beam's cooling power, the maximum relative air velocity was limited to 0.1 m/s in this study [117]. These two maximum relative air speeds are applied to simulations included in Chapter 5 for estimating the PMV and PPD differences between the two systems.

Table 4-5. Thermal comfort parameters.

Specification for Thermal Condition Calculation		
Operative Temperature, PMV, PPD	ASHRAE Standard 55	
Occupant location	Center of the office	
Clothing level	0.57 clo : Trousers, short-sleeve shirt	
Metabolic rate	1.1 met : Office activities (typing)	
External work	0 met	
Relative air speed	PCB System (0.1 m/s)	Air System (0.2 m/s)

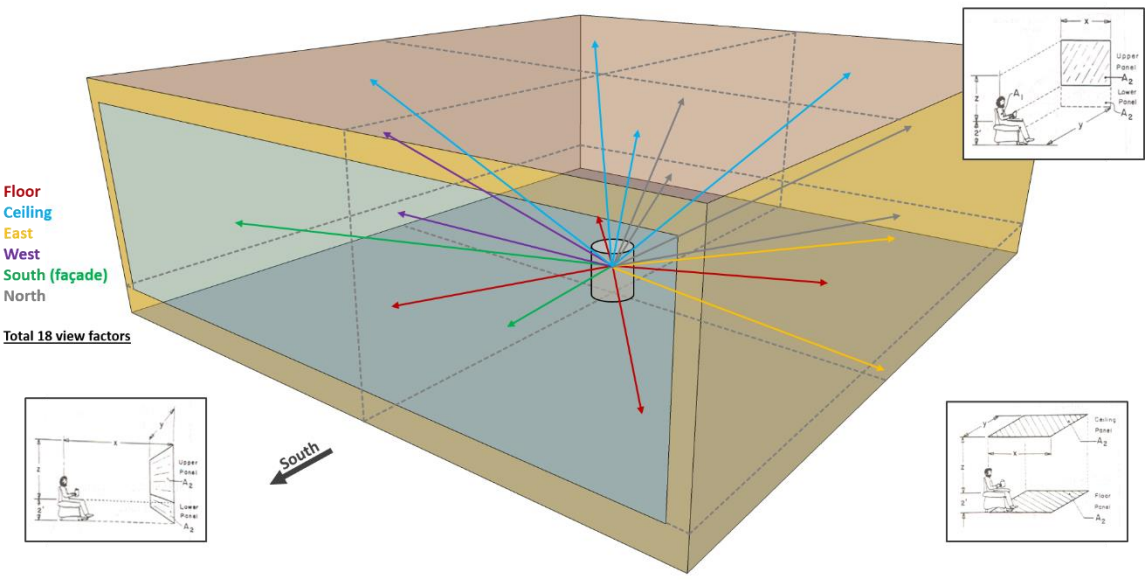

Figure 4-26. View factor calculation of an occupant against indoor surfaces.

4.2.3. Models for Other HVAC Components

A typical air system, which is widely used in large office buildings [130], is considered as the conventional air system. The system usually includes an air handling unit with integrated cooling coil, supply fan and ventilation dampers and controls. A return fan, preheating coil, reheating coil and VAV box were not included in this section to simplify the approach for the consideration of a summer cooling season. The chilled water source for the cooling coil was assumed to be provided from an air-cooled electric chiller and a constant speed pump was used to provide chilled water from the chiller to the cooling coil. A cooling coil bypass valve is used in this model to modulate the amount of chilled water to the coil to maintain a supply air temperature setpoint. The configuration of this air system is shown in Figure 4-27.

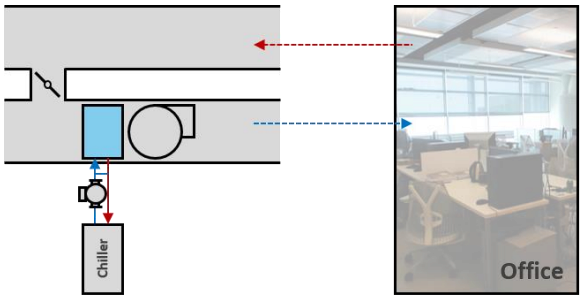

Figure 4-27. Configuration of the VAV system in simulation.

The air-cooled chiller, fan, and pump models are incorporated in the whole building energy simulation model. The air-cooled chiller model is adopted from the TRNSYS library (Type 655). A normalized performance map was used to calculate the power of the chiller from different conditions of rated capacity, rated COP, water mass flow rate, chilled water leaving temperature and ambient air temperature. Performance characteristics of the fan and pump were estimated from actual measurements discussed in section 4.1. Supply flow rate and power consumption of the fan and the pump were directly coupled by using a 2^{nd} order polynomial. Performance characteristics of these components are shown in Figure 4-28. A minimum outdoor air requirement suggested from the ASHRAE Standard 90.1 [128] is applied in each case.

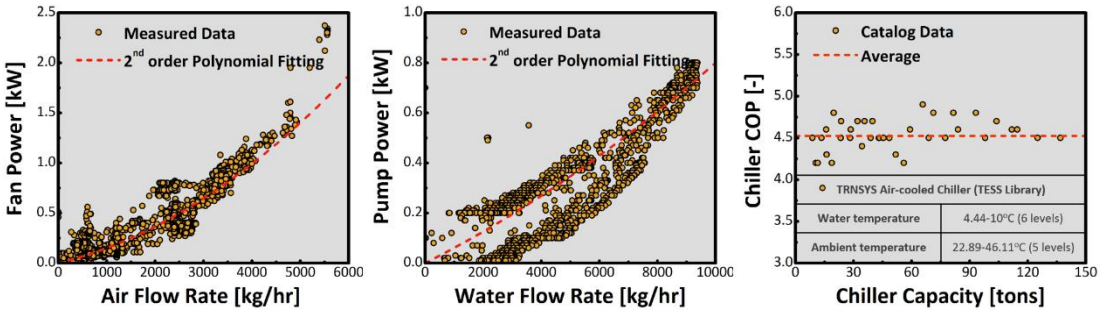

Figure 4-28. Model specification of fan, pump and chiller.

4.3. Validation of Whole-Building Energy Simulation

A validation study is presented in this section to verify whether the whole building energy simulation model can represent the actual building and the system properly under the same weather condition. Typical validation of the whole building energy simulation model can be performed in two steps. The envelope model is usually validated first by comparing free floating temperatures in the space between the experiment and simulation under certain weather condition variation. Then, the HVAC system model can be applied in the simulation and the system performance results can be compared between the measurement and simulation. However, in this study, since the relative performance is mostly analyzed rather than quantifying energy performance on an absolute scale, the validation of the whole building energy simulation is also performed by comparing relative performances between the experiment and simulation. More specifically, the relative energy savings are compared between the field measurement and the whole building energy simulation.

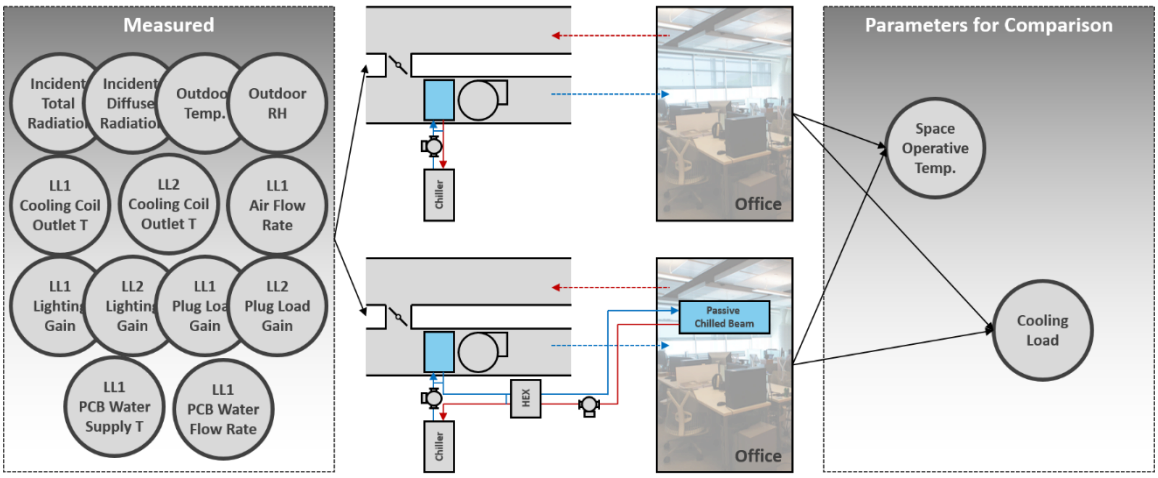

Figure 4-29. Validation methodology of the whole building energy simulation model.

Figure 4-29 shows the methodology of how the validation was performed against field measurements of the Living Lab. Parameters shown in the left box of the figure are collected from the field measurement data to use as inputs to the simulation for both the variable air volume and passive chilled beam system. These inputs include weather data, supply air temperature and flow rate, internal gains and passive chilled beam's operating condition. By applying these data into the simulation, variations of the space operative temperature and the cooling load is compared against the actual measurements from the Living Lab. Figure 4-30 shows the 48 hours of field measurements during 6th and 7th of September 2016 that includes all the input parameters used in the simulation.

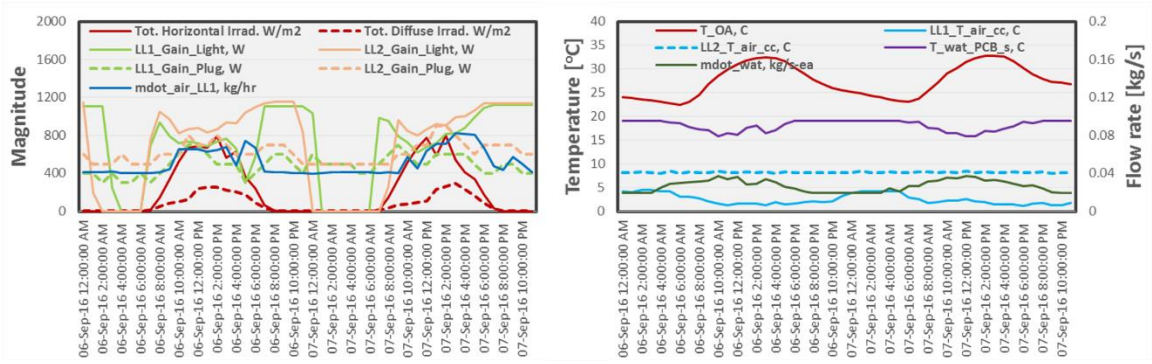

Figure 4-30. Measurement inputs for the validation.

In order to properly represent the current systems, the configurations of the VAV system and the passive chilled beam system are defined as shown in Table 4-6. These configurations mostly follow Table 4-2, while changes were made for using actual measurements as inputs to the simulation.

Table 4-6. Configurations of the VAV and the passive chilled beam system simulations.

	Variable Air Volume (VAV) System	**Passive Chilled Beam System**
Weather Data	measurement data is used	
Cooling Coil	Input data is used	
Supply Fan	modulate based on space temp stpt. min. flow = min. OA requirement 200CFM	measurement data is used
Passive Chilled Beam	not used	30 passive chilled beams measurement data is used for temp. and flow rate
Damper System	min. outdoor air requirement control & additional outdoor air when $T_{OA} < T_{RA}$	not used
Internal Gain	measurement data is used	

Figure 4-31 and Figure 4-32 show 48 hours of time variant results from the experiment and simulation. For the simulation, the timestep was 0.01 hours (36 seconds) and the operative temperature was used for the reference temperature with a setpoint of 23.3^{o}C (74^{o}F). Based on Figure 4-32 which includes operative temperatures in the Living Lab #1 and #2, the sensible cooling demand is only present between 12pm to 8pm. Besides this period, minimum dehumidification with minimum outdoor air requirement was provided to the space resulting in decreasing temperatures in the space. While temperature variations in the Living Lab #2 agree with each other fairly well between the experiment and simulation results, the temperature variation shown in the Living Lab #1's simulation result is relatively unstable. This is mostly because of the water supply temperature and flow rate in passive chilled beams that were used as inputs. The temperature and the flow rate were both modulated in field measurements with separate PID controller where both controllers used the same controlled variable (operative temperature). However, in the TRNSYS simulation, two separate PID controllers cannot use the same controlled

variable. Thus, instead of using the model to control passive chilled beams, the measurements were used as inputs. Additional load variations (human occupant behavior and shading control) in the space that were not captured in the simulation have caused this fluctuation. However, the order of magnitude of the operative temperature matches between the experiment and simulation. Figure 4-32 shows cooling coil and passive chilled beam loads. The absolute scale and the profile differences between the experiment and simulation results are within the reasonable agreement.

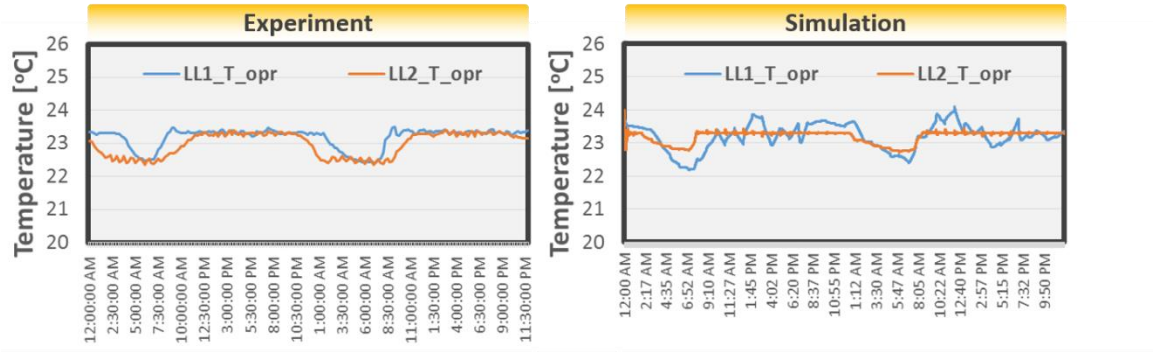

Figure 4-31. Time variant results between experiment and simulation (1/2).

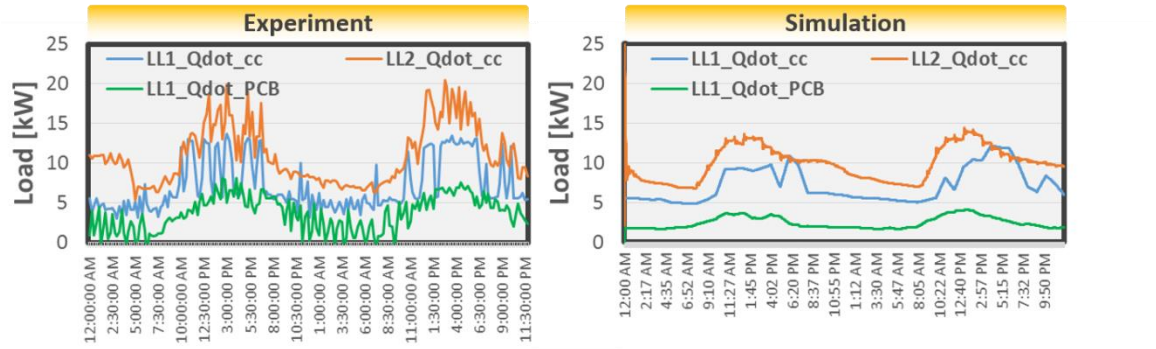

Figure 4-32. Time variant results between experiment and simulation (2/2).

Figure 4-33 shows the summary of the results comparing the cumulative load during 48 hours of experiment and simulation. The cooling coil load shown in the experiment represents the total load which is the sum of sensible and latent load. The absolute scales and the relative savings between the experiment and simulation show reasonable agreement.

In terms of the comparison between systems, the passive chilled beam system does not provide significant amount of energy savings compared to the VAV system as shown in Figure 4-33. While this was discussed in section 4.1.2.2.2 based on the field measurements, the simulation results also support the inefficient passive chilled beam system against the VAV system. The scenario where the damper system in the AHU helps to reduce the load in the passive chilled beam system will be covered with the computer simulation in Chapter 5.

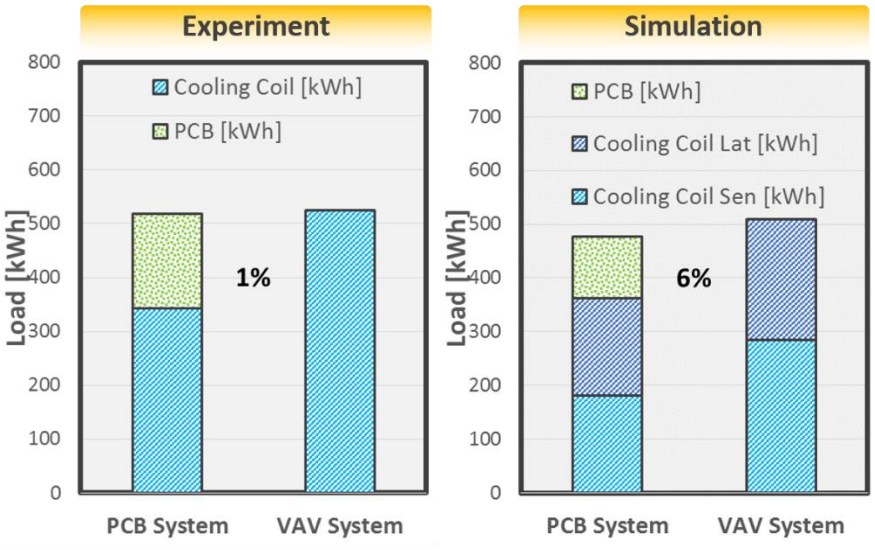

Figure 4-33. Relative energy use comparison between experiment and simulation.

CHAPTER 5. EVALUATION OF ALTERNATIVE PASSIVE CHILLED BEAM SYSTEM CONFIGURATIONS THROUGH WHOLE BUILDING ENERGY SIMULATION

In previous chapters, the performance of passive chilled beams was studied through testing in a laboratory controlled environment and in an office environment at both the component and system level. However, there are other system configurations that could lead to better performance and should therefore be investigated. Figure 5-1 shows a schematic which explains what is being done in this chapter. The performance of four different passive chilled beam systems are analyzed in relation to a conventional VAV system using the whole building energy simulation model that is described in the previous chapter. The systems are analyzed in terms of energy consumption while economic analysis is not considered in this study. However, the economic analysis of the passive chilled beam system should be performed in future studies. The TRNSYS software is used for the whole building energy simulation [131].

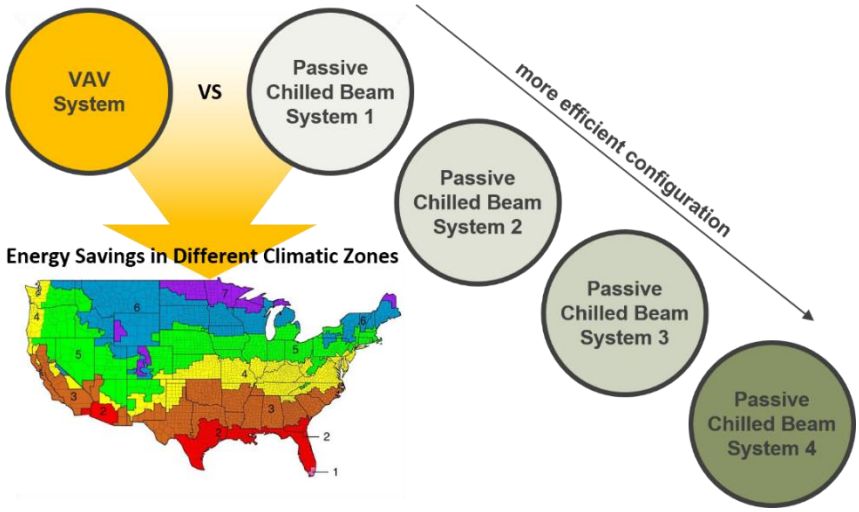

Figure 5-1. The potential for efficient passive chilled beam configurations in different climatic zones vs VAV systems.

5.1. Passive Chilled Beam System's Potentials under Different Climates with Different Configurations

One of the features of using a passive chilled beam system is that it provides energy savings opportunity by decoupling the sensible and latent loads. This savings opportunity will be affected by different climatic zones. Therefore the first goal of this chapter is to estimate the passive chilled beam system's potential in different climatic zones. Another feature is the use of a parallel air system which can have different configurations according to different situations. A dedicated outdoor air system (DOAS) is considered as the best option and since it can have different configurations, investigating its potential benefits with passive chilled beams is set as a second goal of this chapter.

5.1.1. Climatic Data

The 11 US climatic zones shown in Figure 60 are used for this study. The different climatic zones include different ambient humidity levels (marine, dry and moist) with five different latitudes (zone 1 to 5) based on the U.S. climate zone map in ANSI/ASHRAE Standard 90.1 [128]. Based on this classification, eleven different cities were selected to import TMY 2 weather data into the simulation. Since the study focuses on cooling system performance, zone 6 and higher were not considered. Detailed definitions of each climate zone can be found in ANSI/ASHRAE Standard 90.1 [128]. Combinations of one digit number and one alphabet letter representing each climatic zone are used to describe results and the scheme is depicted in Figure 5-2. Lower numbers are used for hotter climates while "A" represents moister climates in the south east, "B" represents drier climates in the non-coastal west and "C" represents marine climates on the west coast.

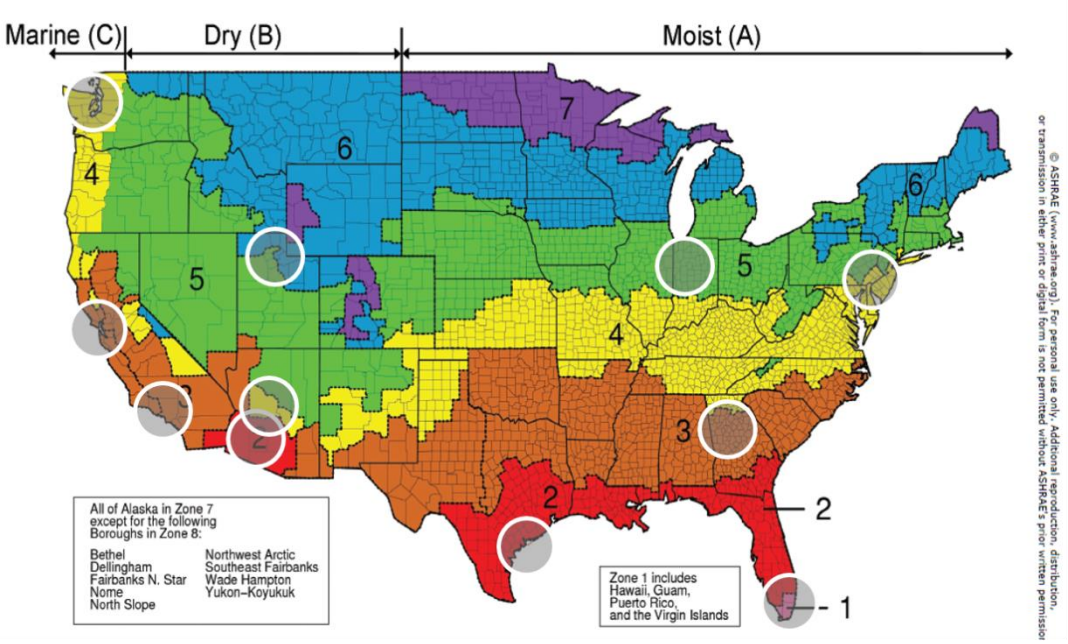

Selected Cities in Each Climate Zone										
1A	2A	3A	4A	5A	2B	3B	4B	5B	3C	4C
Miami	Houston	Atlanta	Philadelphia	Lafayette	Phoenix	L.A.	Prescott	Salt Lake City	San Francisco	Seattle

Figure 5-2. Eleven cities representing the different climatic zones.

5.1.2. Different Configurations of Passive Chilled Beam System

A parallel air system combined with passive chilled beams can have different configurations. Four different configurations were considered under different weather conditions. Figure 5-3 shows the four configurations considered in this chapter.

The first configuration (PCB 1) represents the minimum retrofit scenario when a conventional air system is combined with passive chilled beams. This configuration is very similar to the configuration shown in the field measurement in Chapter 4. The chiller is connected to a pump and bypass cooling coil through a water loop. An additional bypass heat exchanger is used to separate the cooling coil loop and the passive chilled beam loop. Another pump is installed in the passive chilled beam loop to control the water flow rate in the passive chilled beams. Use of this additional heat exchanger provides an ability to control the water supply temperature and the water flow rate separately. While the outdoor air and return air damper system in the AHU was not used in the validation simulation in section 3.1.2, the damper system is used in this

configuration to mix the outdoor fresh air with the return air when the supply air flow rate is larger than the minimum outdoor air requirement. All the equipment models for this configuration are described in section 4.2.3.

The second configuration (PCB 2) represents the simplest dedicated outdoor air system (DOAS) with an energy recovery wheel installed before the cooling coil. This energy recovery wheel starts to rotate when the temperature of the outdoor air is higher than the return air to take the advantage of relatively cool and dry return air stream. All the other configurations are the same as PCB 1. The energy recovery wheel model, Type 667, was adopted from the TRNSYS TESS library. This model is a constant effectiveness and minimum capacitance model which can calculate both the sensible heat and latent moisture exchange. The default values of 0.6 constant sensible effectiveness and 0.3 constant latent effectiveness were used for the simulation.

The third configuration (PCB 3) has one extra feature compared to PCB 2. Instead of using the shared chiller (chiller 1) for both the cooling coil and passive chilled beams, a separate chiller (chiller 2) is installed for passive chilled beams. All specifications are the same between two chillers besides the water supply temperature setpoint. The supply temperature is set as 14^{o}C for chiller 2 which corresponds to the minimum water supply temperature of passive chilled beams. If all the other parameters of the chiller are fixed, higher water supply temperature can result in higher operating COP of the chiller. This configuration is considered to capture this benefit.

The fourth configuration (PCB 4) has another extra feature compared to PCB 3. A desiccant wheel is installed after the cooling coil to take the advantage of the relatively dry return air stream. Moisture removal from the supply air due to this wheel results in a sensible heat gain (increased supply air temperature), which must be offset by an increased sensible load on the passive chilled beams. The desiccant wheel starts to rotate when the space humidity reaches the upper band of the setpoint, and stops when it reaches the lower band of the setpoint. Supplying relatively dry air to the space will decrease the amount of air required for latent load demand which will decrease the load on cooling coil. The desiccant wheel model, Type 716, was adopted from the TRNSYS TESS library. This model which represents a rotary desiccant wheel containing silica gel

is based on a performance map developed from a previous study [132]. Although the same type of desiccant wheel can be used for the energy recovery wheel in reality, this desiccant wheel model application range is beyond the conditions for applying it to the outdoor air side. Thus, a relatively simplified model was used for the energy recovery wheel while the desiccant wheel considered in PCB 4 was analyzed using the detailed model.

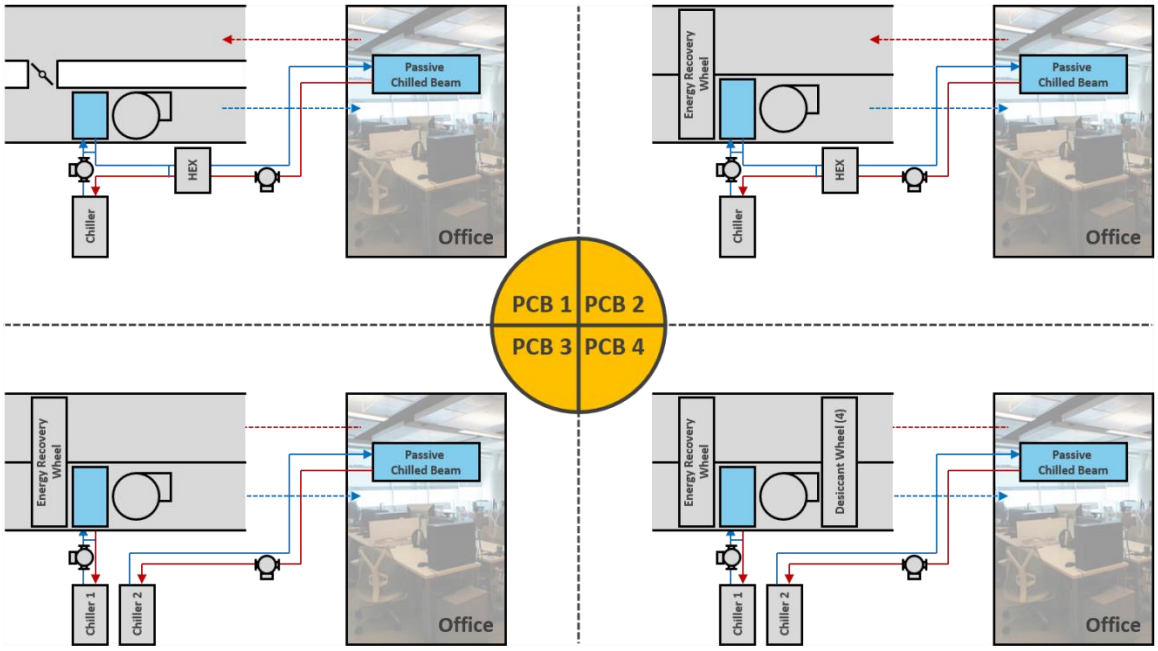

Figure 5-3. Different configurations of passive chilled beam system.

Table 5-1 shows specifications and control strategies for each component in each system. A temperature setpoint reset strategy was implemented for the cooling coil air outlet temperature between occupied hours and unoccupied hours in all systems. Two different scenarios were considered in terms of operating the water pump in the cooling coil water loop. The first is a constant speed pump scenario which is similar to the actual field measurement setup described in section 4.1. The second scenario represents a variable speed pump scenario in the cooling coil water loop. In scenario 1, this pump was operated with fixed speed and sized for the peak cooling demand. And since there is a bypass loop in the cooling coil, the flow could be modulated between the cooling coil and

Table 5-1. Specifications of each configuration.

	VAV	PCB 1	PCB 2	PCB 3	PCB 4
Cooling Coil	Outlet air temp. stpt. reset, 10^{o}C between 8am to 8pm, otherwise 13^{o}C				
Pump (cooling coil)	Scenario 1: constant speed pump 3000 kg/hr Scenario 2: variable speed pump modulate for cooling coil stpt.				
Air-cooled Chiller 1	chiller outlet water temp. stpt. 2^{o}C (8 tons unit)				
Supply Fan	Modulate for space temp stpt. including min. OA (200 CFM)	Modulate (-400CFM) for space humidity stpt. (0.009 kg_{H2O}/kg_{air} between 8am to 8pm, otherwise 0.013 kg_{H2O}/kg_{air}), including min. OA (200 CFM)			
Additional heat exchanger	Not Used	modulate bypass for water temp. stpt. 14^{o}C (effectiveness 0.65)		Not Used	Not Used
Pump (passive chilled beam)	Not Used	Modulate for space temp. stpt.			
Air-cooled Chiller 2	Not Used	Not Used	Not Used	chiller outlet temp. stpt. 14^{o}C (8 tons unit)	
AHU Damper System	If $\dot{m}_{air,SA} > \dot{m}_{air,\min,OA}$ & $enthalpy_{\_OA} > enthalpy_{\_RA}$, make up additional air with RA		Not Used		
Energy Recovery Wheel	Not Used	Not Used	ON if $T_{OA} > T_{RA}$ (sensible effect. = 0.6 / latent effect. = 0.3)		
Desiccant Wheel	Not Used	Not Used	Not Used	Not Used	ON if HR > stpt+0.001 OFF if HR < stpt.-0.001
Passive Chilled Beam	Not Used	10 units			

the bypass so that the cooling coil air outlet temperature could be controlled. In scenario 2, this pump was operated as a variable speed pump where it modulated to meet the cooling coil air outlet temperature setpoint. In this case, there is no bypass loop for the cooling coil. The minimum outdoor air requirement was set with 200 CFM in all configurations and the supply fan in the air system always maintained this minimum ventilation rate. While the humidity in the space was controlled passively by the sensible load demand in the VAV system, a humidity ratio setpoint was applied in the PCB systems to modulate the fan between 200 CFM to 400 CFM. The pump installed in the

passive chilled beam water loop was modulated to meet the space reference temperature setpoint. The dedicated chiller (chiller 2) for passive chilled beams in PCB 3 and 4 had the same specification as chiller 1 with a higher water supply temperature setpoint. The water supply temperature setpoint of the chiller 2 was set as 14^{o}C which will result in higher operating COP compared to the chiller 1. The outdoor and return air damper system in the AHU in VAV and PCB 1 operates to make up the additional amount of air with the return air when the required supply air flow rate ($\dot{m}_{air,SA}$) exceeds the minimum outdoor air requirement ($\dot{m}_{air,\min,OA}$) and when the enthalpy of the outdoor air is higher than that of the return air. The energy recovery wheel in PCB 2, 3 and 4 starts to rotate when the outdoor air temperature (T_{OA}) is higher than the return air temperature (T_{RA}). The desiccant wheel in PCB 4 monitors the space humidity ratio and starts to rotate when the space humidity ratio reaches the upper-band of the setpoint and stops when it reaches the lower-band of the setpoint. Ten passive chilled beams were selected for the simulation cases.

5.1.3. Performance Calculations of Passive Chilled Beams

As was discussed in a previous study [133], the total cooling capacity and the surface temperature of passive chilled beams calculated from Eqs. (3.1) and (3.2) were implemented in TRNSYS in a process shown in Figure 5-4. The total cooling capacity was assumed as the sum of the convection and radiation cooling capacities. The predicted surface temperature of the passive chilled beam calculated from Eq. (3.2) was used with a simplified radiation heat transfer rate calculation [19] shown in the equation below in order to estimate the fraction of convective and radiative cooling provided by passive chilled beams.

$$\dot{Q}_{PCB,rad} = 5\times10^{-8} A_{PCB}\left[\left(AUST + 273.15\right)^4 - \left(T_{surf,PCB} + 273.15\right)^4\right] \quad (4.2)$$

The passive chilled beam considered in this simulation has 0.52 m^2 effective surface area per each chilled beam and this value was used to calculate the total effective surface area

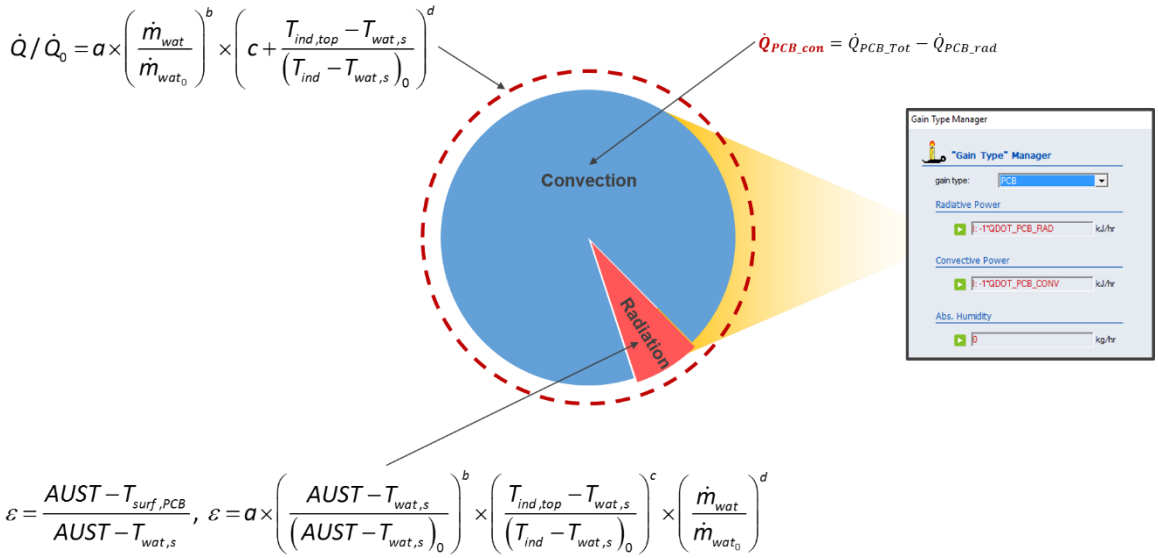

Figure 5-4. Passive chilled beam models applied in TRNSYS.

for the 10 units considered. After both the total cooling capacity and the surface temperature of passive chilled beams are calculated simultaneously in each time step (based on the operating and thermal conditions inside the space), the convective portion of cooling capacity is calculated by subtracting the radiation portion from the total as shown in Figure 5-4. Then the convective and radiative portion of cooling power is applied as a negative heat gain in the TRNSYS Type 56 thermal zone model.

Although the TYPE 56 thermal zone model in TRNSYS calculates mean radiant temperature, operative temperature and PMV, it does not include the effect of the chilled surface of passive chilled beams in the space in calculating these outputs. However, it also has to be noted that the resultant indoor surface temperatures for other surfaces do include the effect of the chilled beam, since the radiation cooling power of passive chilled beams is directly included in the energy balance equation in TYPE 56. Due to this limitation in the software, an external calculation of the mean radiant temperature, operative temperature and PMV was done at each time step.

5.1.4. Simulation Results

Each simulation was performed with a 0.01 hour (36 second) timestep and for 12 days including two weekdays and one weekend. The operative temperature is used as the

reference temperature with a setpoint of 23°C. A total of 110 simulations was performed including 11 climatic zones × 5 configurations × 2 pump scenarios. Results of thermal conditions in the space for each simulation is covered first to verify whether each simulation is fairly comparable. Then the energy savings potential is discussed.

5.1.4.1. Thermal conditions in offices for two representative climatic zones

In order to fairly compare different simulated configurations, the comfort conditions within the space should be within relatively good agreement for any location. Two representative climatic zones (Lafayette, IN, and Phoenix, AZ) were selected to analyze the thermal conditions in the space in detail. Figure 5-5 shows histograms of the operative temperature, indoor drybulb temperature, mean radiant temperature and relative humidity, average thermal comfort levels (PMV and PPD) and several operating conditions (water flow rate and chilled surface temperature of passive chilled beams) during the occupied hours. This figure represents 1 climatic zone (Lafayette, IN), 5 configurations and constant speed pump scenario. Since the operative temperature is used as the reference temperature, all 5 configuration cases show good agreement with each other in terms of the operative temperature distribution. The drybulb and mean radiant temperatures between the VAV system and PCB systems slightly differ with each other due to the radiation cooling effect of passive chilled beams. While the space relative humidity is maintained strictly around 50% for the VAV system, the PCB systems controlled the space humidity based on the humidity ratio setpoint which resulted in 45-60% relative humidity during occupied hours.

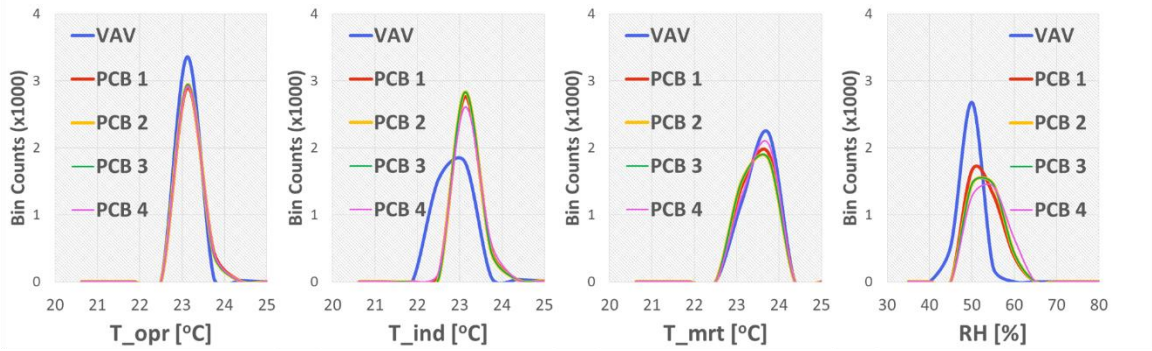

Figure 5-5. Thermal conditions results in Lafayette and constant speed pump scenario.

Thermal comfort indices such as the PMV and PPD based on the combination of the temperature, relative humidity and other parameters defined in Table 4-5 are shown in the figure Figure 5-6. The PCB system's thermal comfort is better than the VAV system and, based on additional simulation runs, this difference mostly comes from the relative air velocity difference rather than the passive chilled beams' radiation cooling effect. Section 4.1.3 showed that the effect of radiation cooling of passive chilled beams is insignificant.

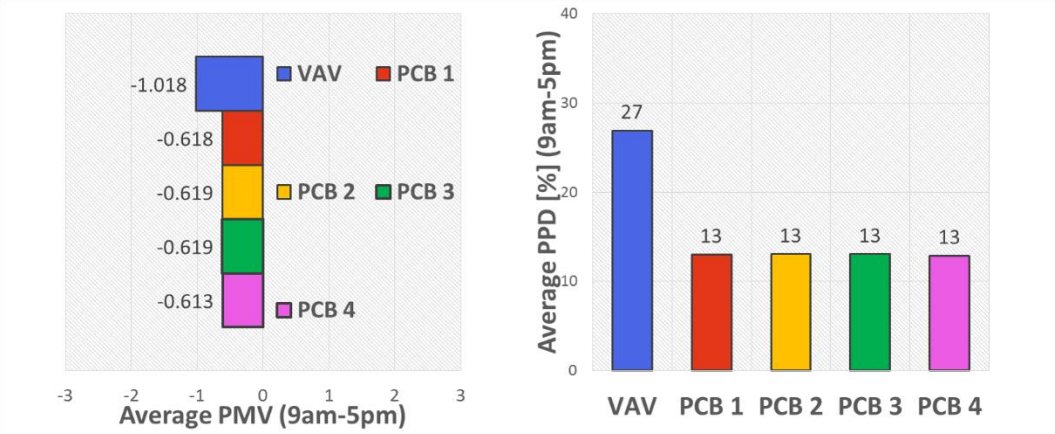

Figure 5-6. Thermal comfort results in Lafayette and constant speed pump scenario.

A typical operating range of the water flow rate for the passive chilled beam can be up to 0.2 kg/s per unit. As shown in Figure 5-7, the maximum and average water flow rate for each configuration are mostly in the low end of the operating range. Although the water supply temperature for passive chilled beams is set to 14^{o}C in all PCB cases, a trade-off (lower temperature with higher flow rate or higher temperature with lower flow rate) between the water supply temperature (14^{o}C to higher) and flow rate (0-0.2 kg/s per unit) can be made depending on the site condition. The chilled surface temperature of passive chilled beams varied from 17 to 22^{o}C with 5.16 m^{2} (10 passive chilled beams) effective surface area.

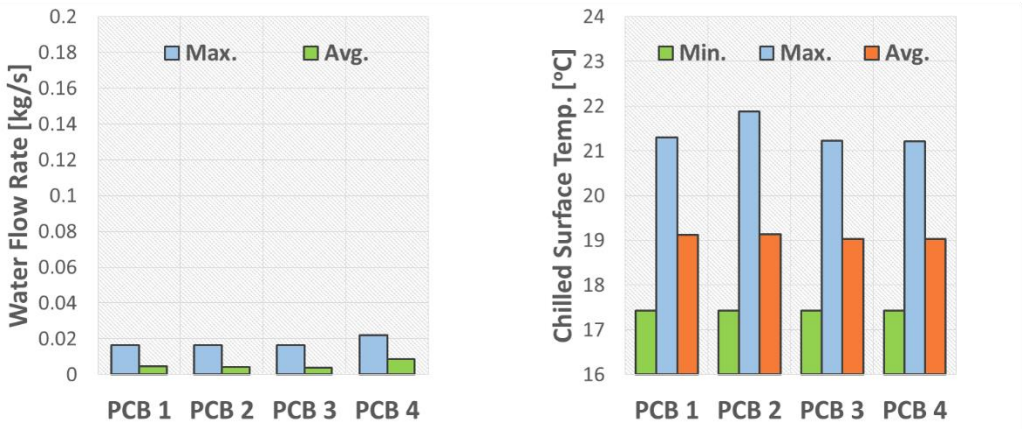

Figure 5-7. Operating conditions results in Lafayette and constant speed pump scenario.

Figure 5-8 to Figure 5-10 represent another climatic zone (Phoenix, AZ), 5 configurations and a constant speed pump scenario. Most of the results shown in the figure are similar to results shown in Figure 5-5 to Figure 5-7.

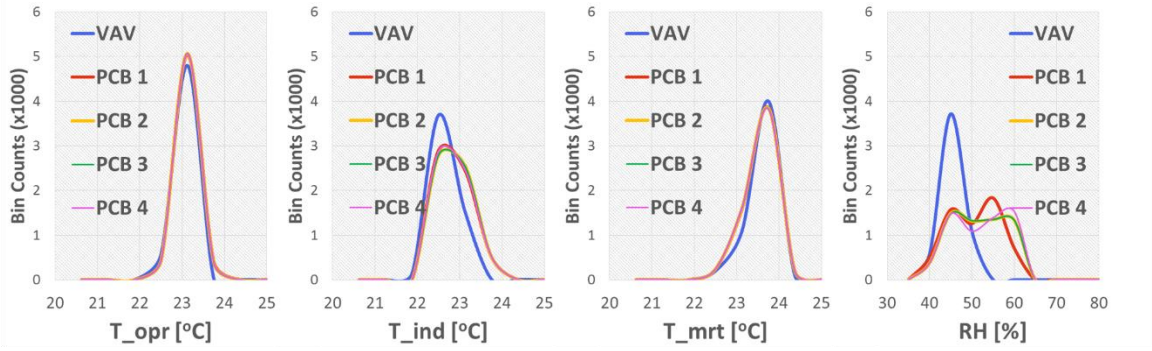

Figure 5-8. Thermal conditions results in Phoenix and constant speed pump scenario.

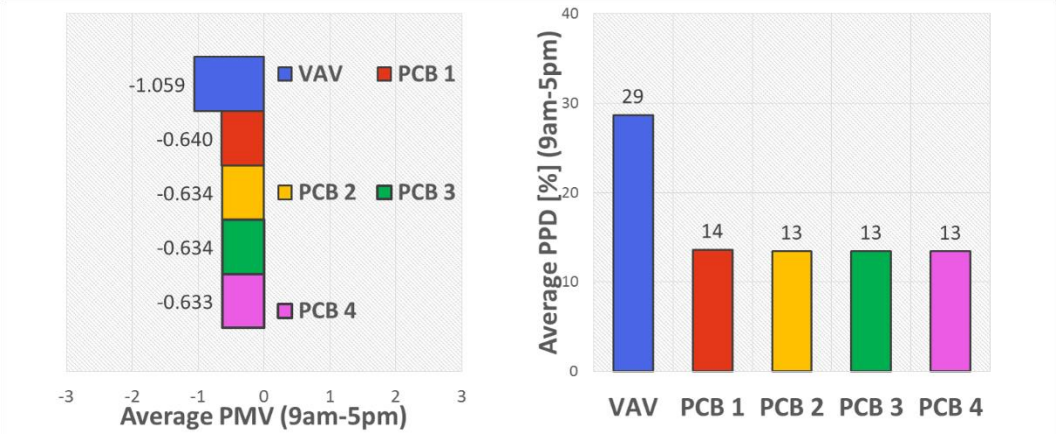

Figure 5-9. Thermal comfort results in Phoenix and constant speed pump scenario.

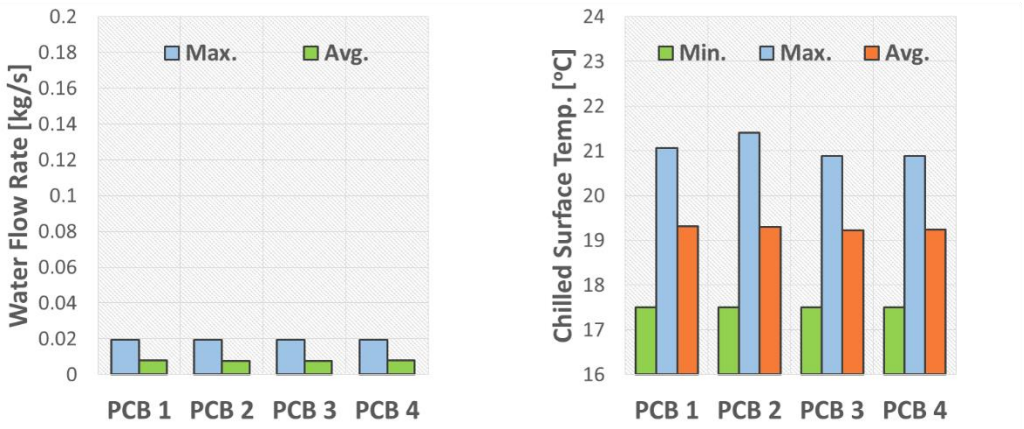

Figure 5-10. Operating conditions results in Phoenix and constant speed pump scenario.

Figure 5-11 to Figure 5-13 and Figure 5-14 to Figure 5-16 show Lafayette and Phoenix results, respectively, but for the variable speed pump scenario. Thermal conditions are mostly the same compared to the previous thermal condition results.

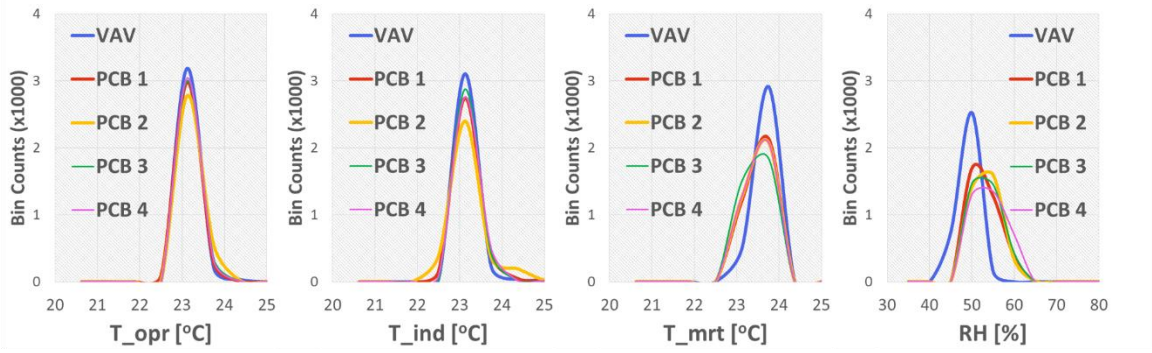

Figure 5-11. Thermal conditions results in Lafayette and variable speed pump scenario.

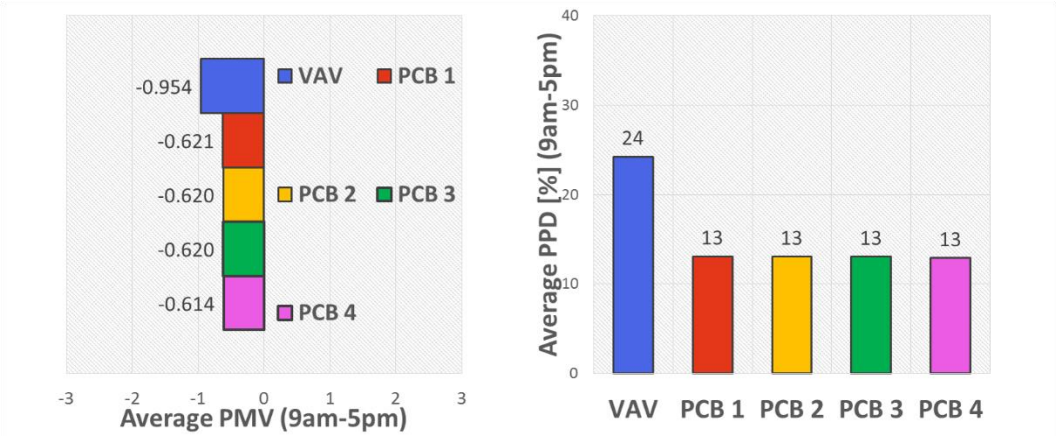

Figure 5-12. Thermal comfort results in Lafayette and variable speed pump scenario.

However, in Figure 5-13, the maximum water flow rate through the passive chilled beams is greatly increased in PCB 1 and 2 compared to the constant speed pump scenario. For the constant speed pump scenario, the flow rate of the pump is sized based on the peak cooling demand and at lower coil load conditions the bypass loop ensures cold enough temperatures to meet the requirements of the passive chilled beams. However in the variable speed pump scenario without the bypass loop, the cooling coil water outlet temperature can be higher than the constant speed pump scenario when the required flow rate of the pump is small. Since this temperature is the source of the passive chilled beam's water supply temperature control, the water supply temperature setpoint cannot be met at certain times. This results in higher water flow rate through the passive chilled beams to offset the increased water supply temperature in order to meet the cooling demand in the space.

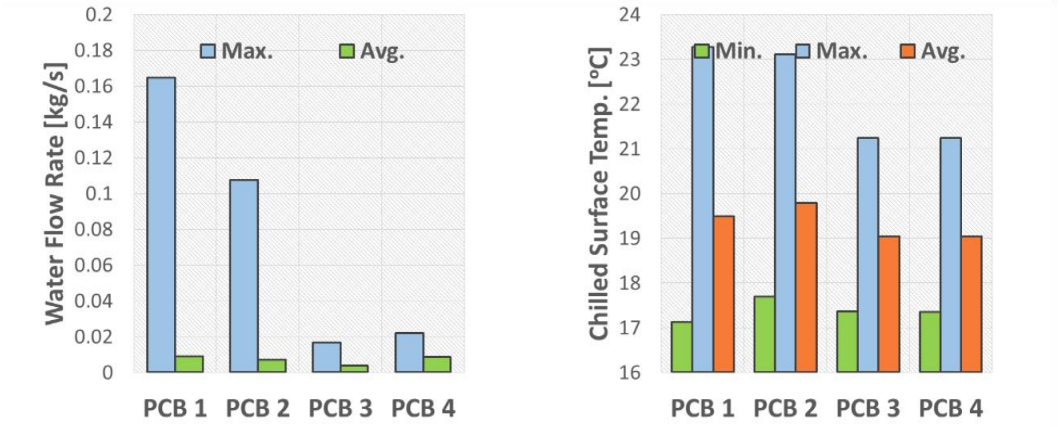

Figure 5-13. Operating conditions results in Lafayette and variable speed pump scenario.

There were cases in certain climatic zones where this issue caused a problem of maintaining proper space condition. In Figure 5-14 to Figure 5-16, PCB 2 under the Phoenix weather condition was not able to maintain the proper thermal conditions in the space. This is the reason why data points for PCB 2 are missing.

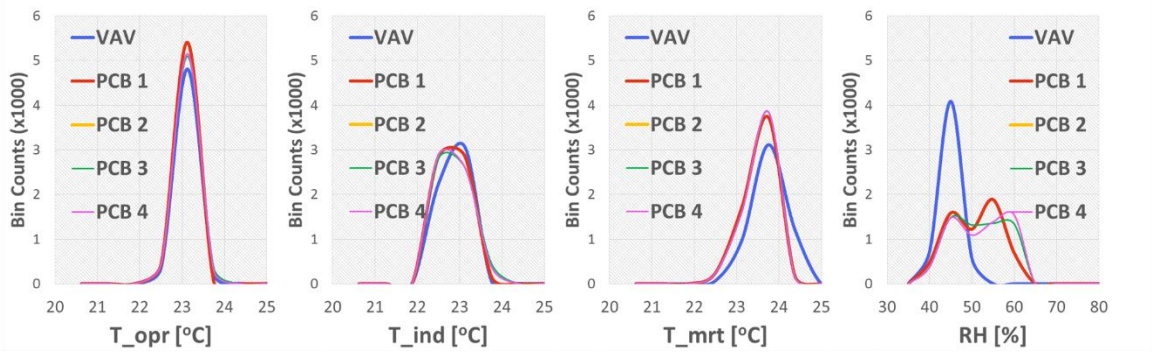

Figure 5-14. Thermal conditions results in Phoenix and variable speed pump scenario.

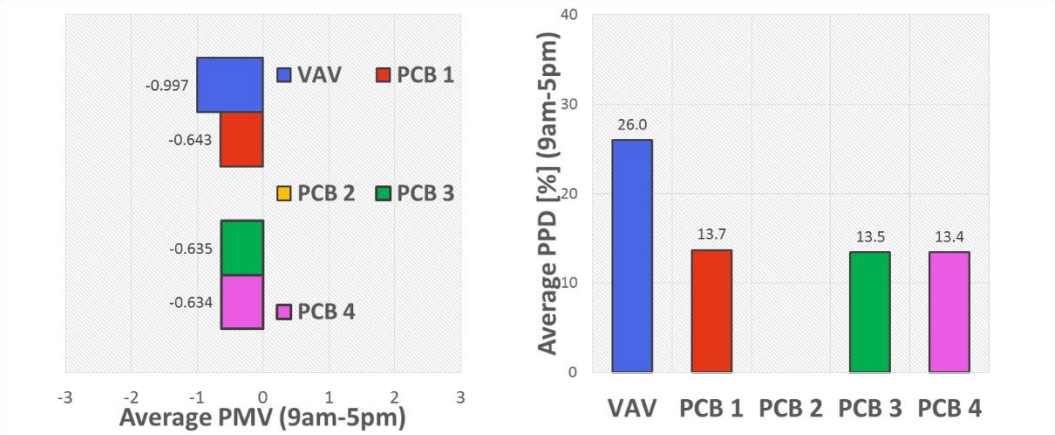

Figure 5-15. Thermal comfort results in Phoenix and variable speed pump scenario.

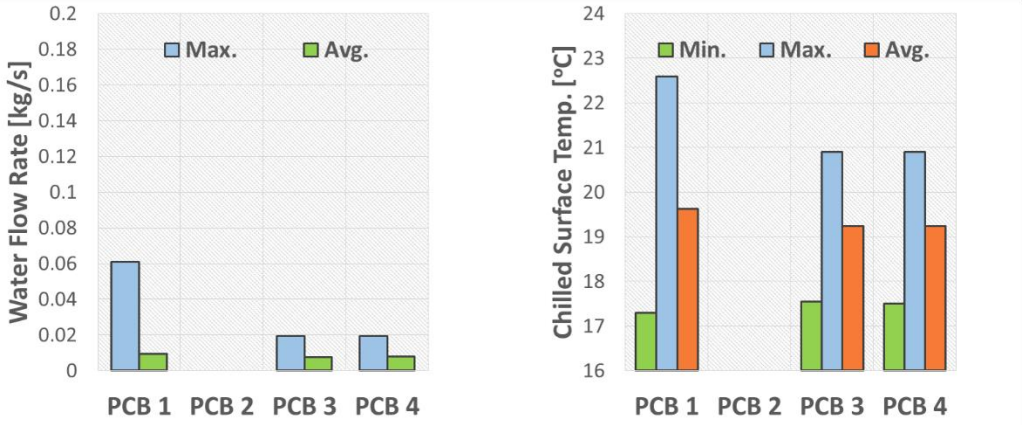

Figure 5-16. Operating conditions results in Phoenix and variable speed pump scenario.

Figure 5-17 shows an example 24-hour period for PCB 1 and PCB 2 with a variable-speed pump in Phoenix. The graph on the top shows the PCB 1 case where the water supply temperature ($T_{wat,PCB,in}$) to the passive chilled beams mostly met the setpoint and

where the system properly conditioned the space. The graph in the bottom shows the PCB 2 case where the water supply temperature to the passive chilled beams did not meet the setpoint. Thus, in order to meet the space conditioning requirement, the water flow rate in the passive chilled beam loop ($\dot{m}_{wat,PCB}$) was greatly increased in PCB 2. Although the space condition remained appropriate during this 24-hour period, there were times when the system could not maintain the space condition properly. Those simulation cases where the space thermal condition was not maintained properly are considered as infeasible and will be shown in section 5.1.4.3. All results shown in this section provide a basis of the fair comparison between simulations for further analysis on the energy savings opportunity shown in the following sections.

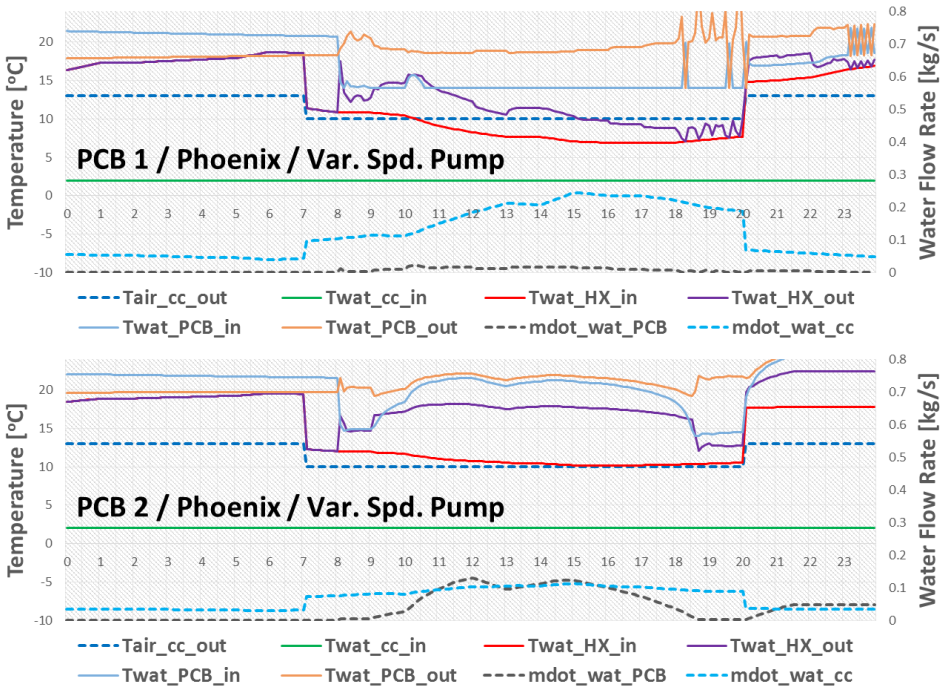

Figure 5-17. Cooling capacity issue in PCB 2 compared to PCB 1 ((Phoenix, variable speed pump).

5.1.4.2. Energy consumptions between systems for two representative climatic zones

This section focuses on detailed aspects of energy saving opportunities for using the passive chilled beam systems compared to the VAV system. Instead of calculating the

rotating power of energy recovery wheels separately, the Recovery Efficiency Ratio (RER) [134], [135] was used to calculate additional power that is consumed due to additional pressure drop caused in the rotary wheels. RER is defined as the "ratio of energy recovered divided by the energy expended in the recovery process". This index is used for estimating additional energy that is required to overcome the extra pressure drop that is caused by air-to-air heat/energy exchangers. Based on one of the manufacturer's technical manuals [136], the RER of rotary wheels was used with 114.6. Figure 5-18 presents energy consumptions and cooling loads for each component for the Lafayette, IN, and constant speed pump scenario.

PCB1 decouples the sensible and latent loads leading to a 4% reduction in total electrical energy compared to the VAV system. In section 4.1.2 and 4.3, both the field measurement and simulation showed that the VAV system used less end-use energy compared to this passive chilled beam system when the outdoor air and return air damper system in the passive chilled beam system were not used for the return air mixing. However, PCB 1 in this study used the damper system in the AHU and when the required supply air flow rate was larger than the minimum outdoor air requirement, the damper system drew return air to make up additional air with return air stream. Based on the simulation result, this can provide slight savings in the passive chilled beam system compared to the VAV system under Lafayette weather conditions.

Compared to PCB 1, replacing the damper system with the energy recovery wheel (PCB 2) does not provide significant additional energy savings. However, the small additional savings come from the different features of the damper system and the energy recovery wheel. Figure 5-19 shows 24 hour period simulation results for PCB 1 (top) and PCB 2 (bottom). In PCB 1, the economizer only draws minimum outdoor air requirement ($\dot{V}_{air,OA}$) when the latent load demand is low. However, when the demand is higher (between 10:30 am to 6:00 pm), the required supply air flow rate ($\dot{V}_{air,SA}$) becomes larger than the minimum outdoor air requirement and the return air damper opens up to make up this extra amount of air. During this period, the ambient air temperature (T_{amb}) can be reduced by taking advantage of mixing with the return air as shown in the cooling coil inlet

temperature ($T_{air,cc,in}$) in the graph. While the benefit of using the damper system is only viable when the latent load demand is high in PCB 1, the energy recovery wheel of PCB2 can ensure a benefit whenever the outdoor air temperature is higher than the return air temperature as shown in the bottom graph. The additional fan power that is caused from the extra pressure drop in the rotary wheel is included starting from this option. Compared to PCB 2, adding a separate chiller (PCB 3) leads to a 5% reduction in total energy consumption due to higher operating COP in the separate chiller (Chiller 2). Compared to PCB 3, adding a desiccant wheel (PCB 4) provides a significant additional energy savings of 14%. Providing relatively dry air by using the desiccant wheel can reduce the amount of air required to meet the latent load demand in the space. Reduced air flow rate decreases the load on the cooling coil. The supply air temperature after the desiccant wheel is higher than the case without the desiccant wheel. However, this difference in sensible cooling power is offset by the passive chilled beams where this equivalent load is handled with higher COP by chiller 2. This transfer of load from the cooling coil to passive chilled beams is also shown in the sensible load graph in Figure 5-18. The most efficient passive chilled beam system considered in this case (PCB 4) can save 14% of the total energy consumed by the VAV system.

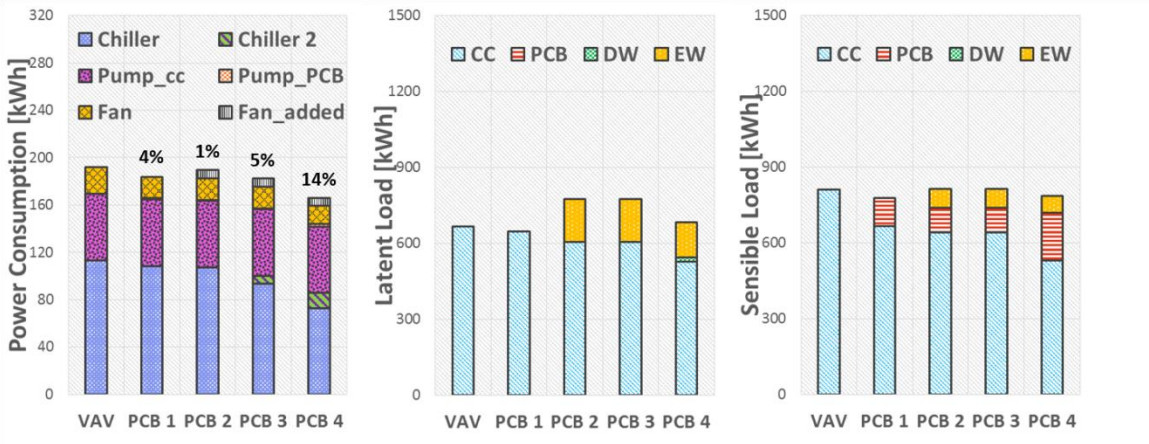

Figure 5-18. Energy consumptions between different configurations (Lafayette, constant speed pump).

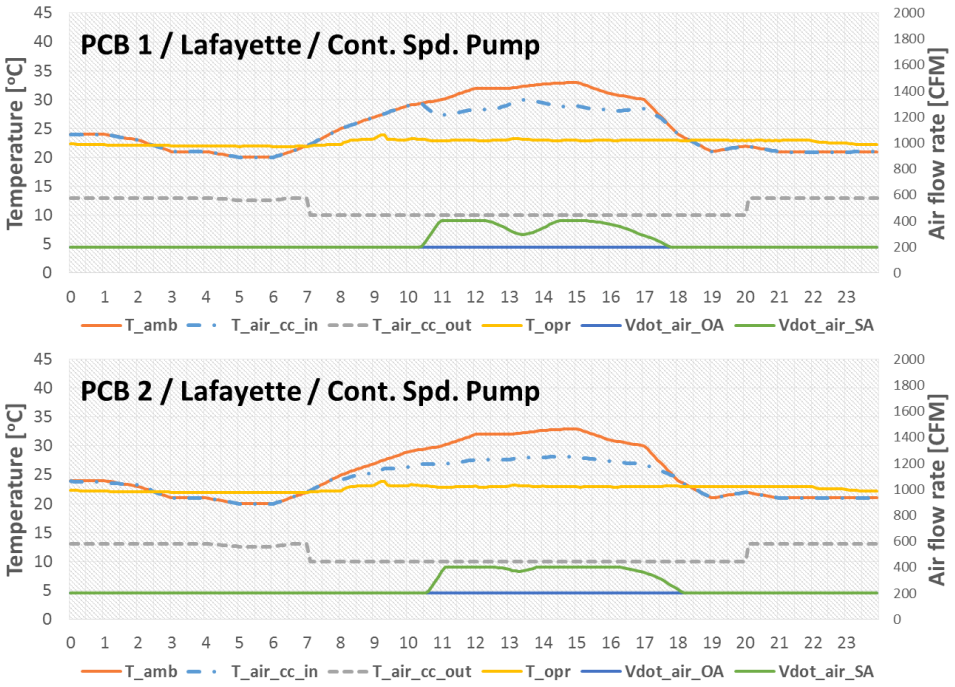

Figure 5-19. Different operation characteristics between the damper system and the energy recovery wheel (Lafayette, constant speed pump).

Figure 5-20 represents Phoenix, AZ, and a constant speed pump scenario. In this case, PCB 1 leads to an energy reduction of 10% compared to the VAV system. The savings percentage increased compared to Lafayette due to a difference in sensible and latent load percentages between the two different climates as shown in Figure 5-18 and Figure 5-20. While the VAV system conditions the space following the sensible load demand, the latent load is automatically taken care of. This can end up over dehumidifying the space compared to what is needed as discussed in a previous study [137]. Since the weather condition in Phoenix is relatively dry compared to Lafayette, there is more opportunity to reduce the dehumidification load in Phoenix by separating the sensible and latent loads using a passive chilled beam system.

Compared to PCB 1, replacing the damper system with an energy recovery wheel (PCB 2) led to additional energy savings of 22%. Unlike the simulation result in Lafayette, the simulated savings opportunity increased significantly for Phoenix due to the higher sensible load to latent load ratio. As shown in the PCB 1 (top) result in Figure 5-21, the

damper system never gets a chance to mix the outdoor air with the return air since the latent load demand is minimum. Thus, 100% outdoor air with minimum ventilation rate is conditioned in the cooling coil for dehumidification. However in PCB 2 (bottom) result, the energy recovery wheel rotates the entire period since the outdoor air temperature is always higher than the return air temperature. Based on characteristics of the damper system and the energy recovery wheel, the savings for this option can be maximized when the sensible load is large and the latent load is small.

Compared to PCB 2, adding a separate chiller (PCB 3) provides 23% energy savings due to higher operating COP in the separate chiller (Chiller 2). Compared to PCB 3, adding a desiccant wheel (PCB 4) does not have a significant impact on energy savings. Since the latent load is already small in terms of total energy demand, the saving is also minimal. The most efficient passive chilled beam system considered in this case (PCB 4) can save 23% of the total energy consumed by the VAV system.

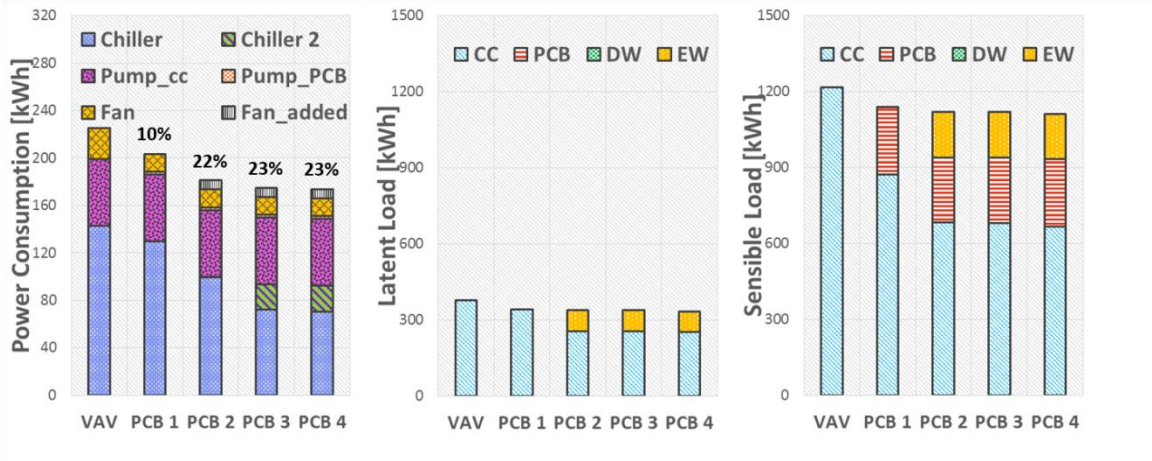

Figure 5-20. Energy consumptions between different configurations (Phoenix, constant speed pump).

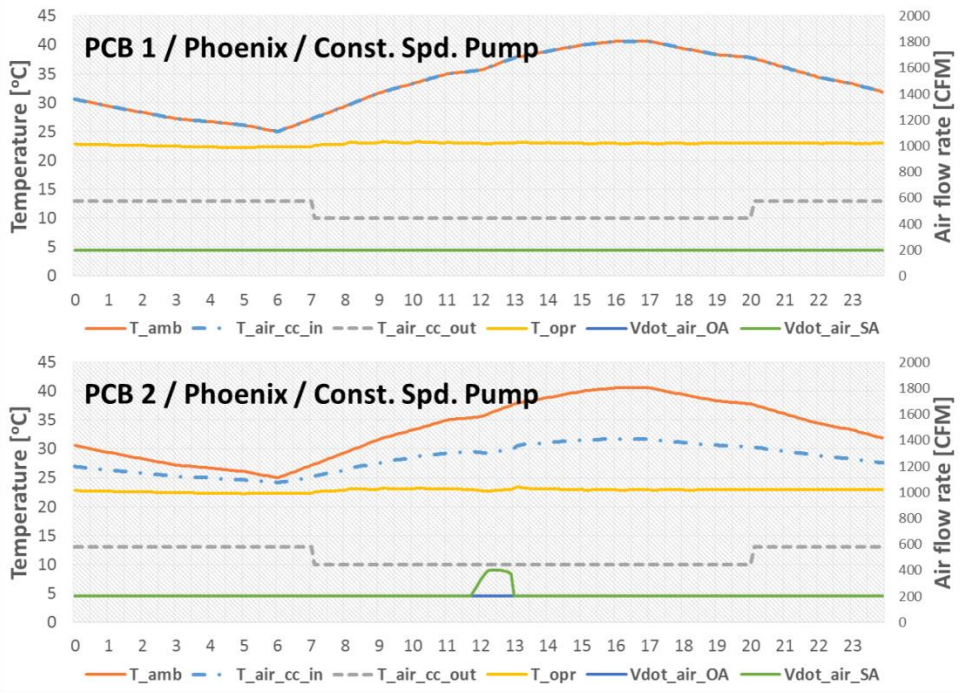

Figure 5-21. Different operation characteristics between the damper system and the energy recovery wheel (Phoenix, constant speed pump).

Figure 5-22 represents Lafayette, IN, and the variable speed pump scenario. The trends in relative savings are similar to those for the constant speed pump scenario shown in Figure 5-18. However, the pump installed in the cooling coil water loop shows significant energy reduction compared to the constant speed pump scenario. Both PCB 1 and PCB 2 configurations are feasible in terms of maintaining proper thermal conditions in the space in these results. Figure 5-23 represents Phoenix, AZ, and the variable speed pump scenario. As described in the previous section, the PCB 2 configuration was not always able to maintain reasonable space thermal conditions and was thus considered an infeasible option for Phoenix. All the other savings trends are similar to the results for the constant pump scenario shown in Figure 5-20. However, the overall energy savings are significantly greater with 19% and 30% savings for PCB 4 in Lafayette and Phoenix, respectively.

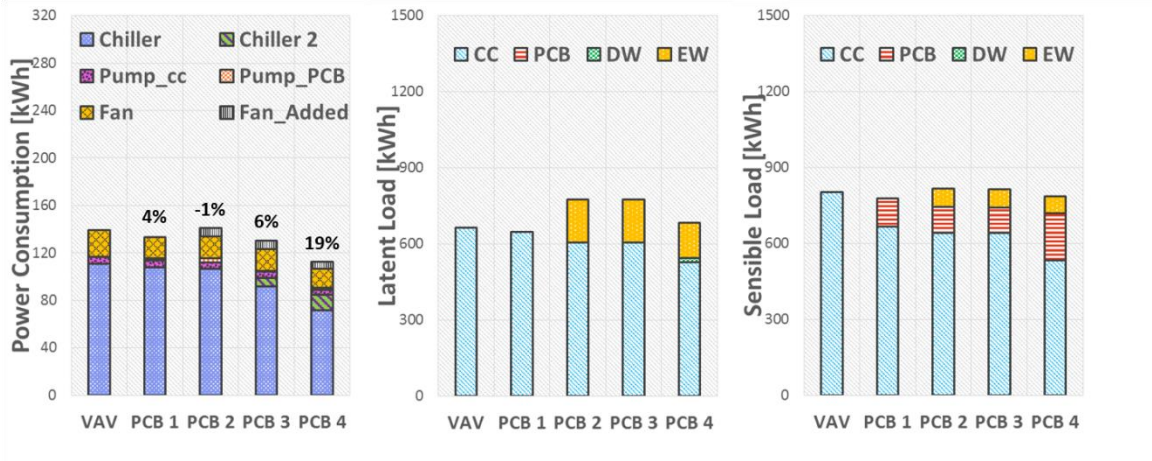

Figure 5-22. Energy consumptions between different configurations (Lafayette, variable speed pump).

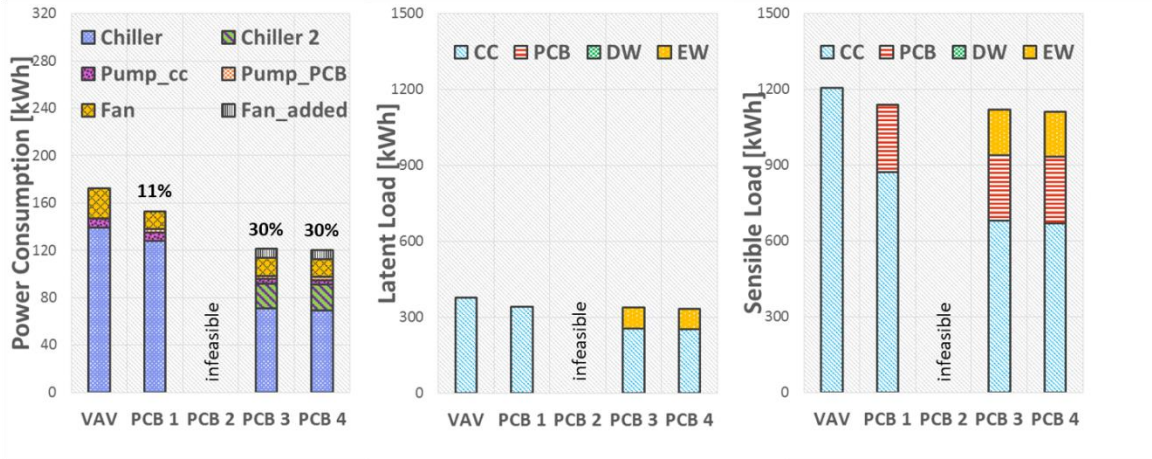

Figure 5-23. Energy consumptions between different configurations (Phoenix, varible speed pump).

5.1.4.3. Energy savings opportunities for all climatic zones and configurations

Figure 5-24 shows relative total end use energy savings compared to the VAV system under 11 different climatic zones with 5 different configurations, but with the constant speed pump scenario.

The savings for PCB 1, which are due to decoupling of the sensible and latent loads, are mostly in the range of 4 to 5 % in humid climatic zones (A). The potential can increase up to 10% in the climates (2B, 4B and 5B) where the ratio of sensible to latent load is

large. In some dry climates where the sensible load is relatively small (3B, 3C and 4C), the savings potential associated with decoupling is minimal. The savings potential associated with replacing the damper system with an energy recovery wheel (PCB 2) can be very significant compared to PCB 1 when the sensible load demand is high while the latent load demand is small (2B). The additional savings potential by adding an extra chiller for the passive chilled beams (PCB 3) is achieved by operating the chiller at a higher COP with the elevated water supply temperature (in this case 2^{o}C to 14^{o}C). If the portion of sensible cooling load taken by passive chilled beams rather than the cooling coil is larger, the savings opportunity can increase as well. This savings opportunity compared to PCB 2 does not vary significantly under different climatic zones. The savings potential associated with adding a desiccant wheel after the cooling coil (PCB 4) is very effective on humid climates (A). There are two aspects of this benefit. The first is the reduced load on the cooling coil which is due to the reduced supply air flow rate. Since the parallel air system's air flow rate is increased when the latent load demand is high in the space, relatively dry air to the space due to using the desiccant wheel can reduce the required air flow rate to the space. The second benefit is due to transferring the sensible load from the cooling coil to the passive chilled beams. After the supply air from the cooling coil passes the desiccant wheel, the temperature of air increases. To maintain the same thermal condition in the space, this temperature increase from the air system is offset by passive chilled beams. This transfer of the sensible load can result in additional energy reduction because the passive chilled beam chiller operates with a higher COP. However, in dry climatic zones (B and C), the savings potential by the desiccant wheel is minimum. The energy savings for PCB 4 with a constant speed pump varied between about 3% and 23% depending on the climate.

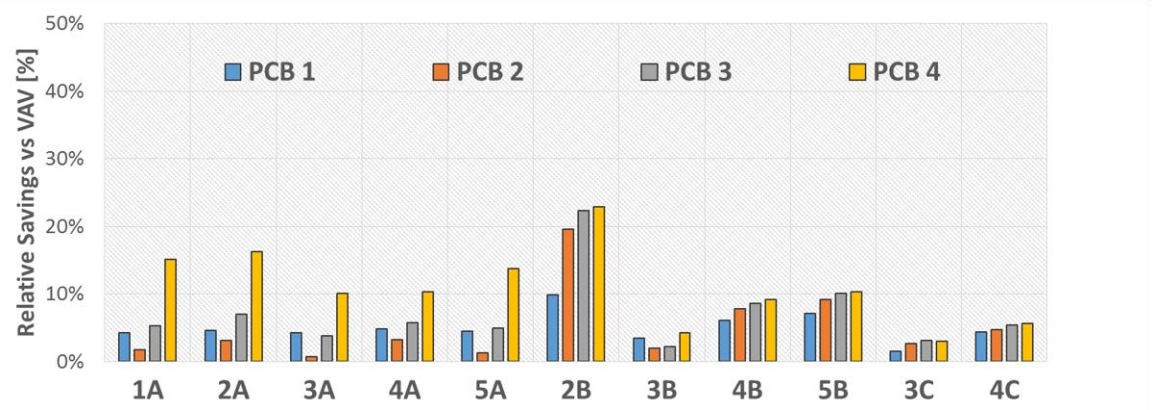

Figure 5-24. Relative energy savings compared to VAV system (constant speed pump) in different climatic zones.

Figure 5-25 shows relative energy savings compared to the VAV system under 11 different climatic zones with 5 different configurations, but with the variable speed pump scenario. As described in section 5.1.4.1, there are climatic zones where the PCB 1 and PCB 2 configurations are infeasible in terms of ensuring proper thermal conditions in the space. In order to maintain proper water supply temperature to passive chilled beams, the water outlet temperature from the cooling coil should also be somewhat lower in PCB 1 and 2 configurations. If the latent load demand is relatively small, the variable speed pump connected to the cooling coil will operate at a lower flow rate since the cooling coil is for dehumidification control in PCB 1 and 2. This will result in higher water temperature to the additional heat exchanger and limits the sensible cooling capacity of passive chilled beams. As shown in Figure 5-25, the infeasible options occur more in relatively dry climatic zones (B and C) since the latent load demand is small. Compared to the constant speed pump scenario, percentages of relative energy savings are larger in all climates. While the constant speed pump in all configurations consumed the same amount of energy, the passive chilled beam system's water pump on the cooling coil consumed less energy compared to the VAV system, resulting in additional savings. The savings for PCB 4 ranged from about 6% to 30% depending on the climate.

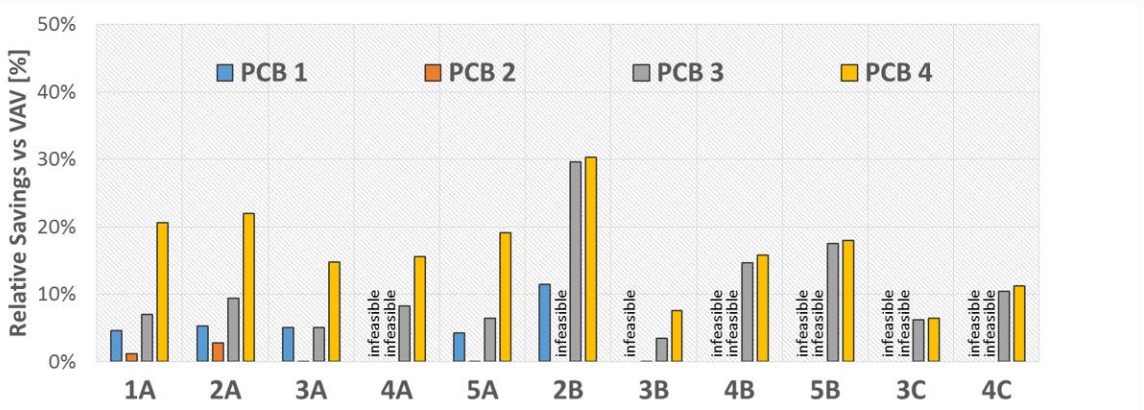

Figure 5-25. Relative energy savings compared to VAV system (variable speed pump).

5.1.4.4. Radiation cooling of passive chilled beams

Using the passive chilled beam models, time variant predictions of passive chilled beams' convective and radiative cooling capacities were calculated in the simulation. Figure 5-26 shows 24 hour period simulation examples under Lafayette (5A) weather conditions with a constant speed pump scenario. The upper graph shows results for the PCB 1 configuration while the lower graph shows PCB 4 results. As previously described, some portion of sensible cooling load is transferred from the cooling coil to passive chilled beams by changing the configuration to PCB 4 from PCB 1. The increased cooling capacities of passive chilled beams in the lower graph corresponds to this change. The convective cooling capacities ($\dot{Q}_{PCB,tot,con}$) are significantly larger than the radiative cooling capacities ($\dot{Q}_{PCB,tot,rad}$) in most of the operating period in both graphs. While the capacity variation is relatively significant with respect to convective cooling capacity in response to water flow rate ($\dot{m}_{wat,PCB}$) variations, the radiative cooling capacity variation is almost negligible. This is also expected from the model validation result shown in Figure 3-25 where the coefficient for the water flow rate term is relatively small compared to the other two terms in Eq. (3.2). For these 24 hour period predictions, portions of radiation cooling energy to the total passive chilled beam cooling energy were calculated as 12% for PCB 1 and 7% for PCB 4.

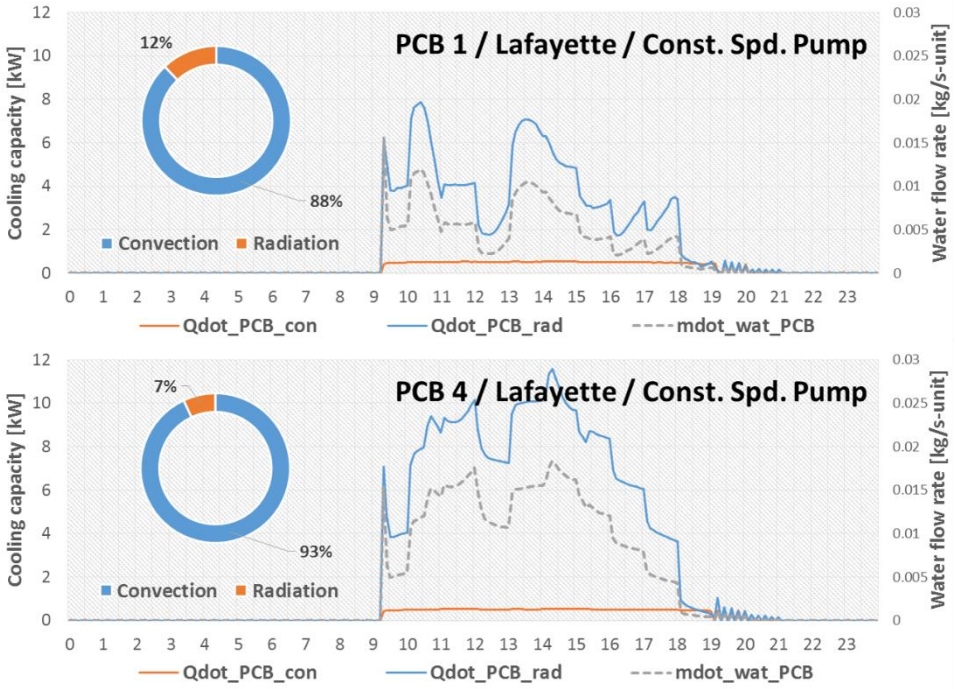

Figure 5-26. Radiation cooling of passive chilled beams (Lafayette, constant speed pump).

The ranges of the passive chilled beams' surface temperature in different simulation cases (constant speed pump scenario) are listed in Table 5-2 which mostly vary from 17°C to 22°C. Variations of these surface temperatures were used as the basis for calculating the radiation cooling power of passive chilled beams as discussed in section 5.1.3.

Table 5-2. Minimum / maximum surface temperatures of passive chilled beams (constant speed pump scenario).

Minimum / maximum surface temperatures of passive chilled beams [°C]					
Climate zone		PCB 1	PCB 2	PCB 3	PCB 4
Miami	1A	17.8 - 22.1	17.8 - 21.2	17.8 - 21	17.8 - 21
Houston	2A	17.5 - 21.4	17.5 - 21.4	17.5 - 21.3	17.5 - 21.3
Atlanta	3A	17.1 - 21.9	17.4 - 21.2	17.3 - 21.2	17.3 - 21.2
Philadelphia	4A	17.4 - 21.6	17.4 - 21.5	17.4 - 21.2	17.4 - 21.2
Lafayette	5A	17.4 - 21.3	17.4 - 21.9	17.4 - 21.2	17.4 - 21.2
Phoenix	2B	17.5 - 21.1	17.5 - 21.4	17.5 - 20.9	17.5 - 20.9
LA	3B	17.3 - 21.1	17.3 - 21.1	17.3 - 21.1	17.3 - 21.1
Prescott	4B	17.4 - 21.2	17.4 - 21.2	17.4 - 21.1	17.4 - 21.1
Salt Lake City	5B	17.5 - 21.2	17.5 - 21.2	17.5 - 21.1	17.5 - 21.1
San Francisco	3C	17.2 - 21.1	17.2 - 21.1	17.2 - 21	17.2 - 21.1
Seattle	4C	17.2 - 21.1	17.2 - 21.1	17.2 - 21	17.2 - 21

Table 5-3 shows the median and maximum radiation cooling capacity for all simulation cases (constant speed pump scenario). Values are fairly similar to each other for the different simulation cases and the difference between the median and the maximum values does not have significant differences. As was shown in the time variant results in Figure 5-26, this is because the water supply temperature setpoint was fixed at 14^{o}C whenever passive chilled beams were in operation.

Table 5-3. Median / maximum radiative cooling capacity of total passive chilled beams (constant speed pump scenario).

Median / Maximum radiative cooling capacity of total passive chilled beams [W]					
Climate zone		**PCB 1**	**PCB 2**	**PCB 3**	**PCB 4**
Miami	1A	493 / 616	495 / 616	501 / 616	500 / 608
Houston	2A	499 / 605	496 / 606	501 / 606	502 / 606
Atlanta	3A	495 / 622	495 / 618	500 / 622	503 / 622
Philadelphia	4A	500 / 638	499 / 638	504 / 638	504 / 638
Lafayette	5A	499 / 630	495 / 630	501 / 630	504 / 630
Phoenix	2B	497 / 611	498 / 611	501 / 611	502 / 611
LA	3B	491 / 619	491 / 619	497 / 619	507 / 619
Prescott	4B	499 / 623	498 / 623	501 / 623	502 / 623
Salt Lake City	5B	505 / 629	504 / 626	507 / 626	507 / 626
San Francisco	3C	484 / 617	483 / 617	489 / 617	502 / 617
Seattle	4C	511 / 643	510 / 643	512 / 643	513 / 643

Table 5-4 shows percentages of radiation cooling energy compared to the total passive chilled beam cooling energy for the entire simulation period for all simulation cases (constant speed pump scenario). In climatic zones where the sensible load demand is moderate, the radiation percentage can be up to 15% of the total cooling demand. However, for the climatic zones with high sensible load demand, the percentage decreases to 8-9%. Since sensible load on passive chilled beams increases for PCB 4 compared to the other configurations, the percentage also decreases to 7-9%.

Table 5-4. Portion of radiation cooling against total passive chilled beam cooling demand (constant speed pump scenario).

Portion of radiation cooling against total passive chilled beam cooling demand [%]					
Climate zone		**PCB 1**	**PCB 2**	**PCB 3**	**PCB 4**
Miami	1A	14	15	15	8
Houston	2A	13	14	15	8
Atlanta	3A	13	14	14	8
Philadelphia	4A	12	12	12	8
Lafayette	5A	13	14	14	8
Phoenix	2B	8	8	8	8
LA	3B	13	14	15	7
Prescott	4B	9	9	9	8
Salt Lake City	5B	8	8	8	8
San Francisco	3C	13	13	14	9
Seattle	4C	9	9	9	8

Table 5-5 shows the maximum water flow rate through the passive chilled beams during the entire simulation period for all simulation cases (constant speed pump scenario). For the constant speed pump scenario, the water flow rate for all simulation cases remained at the low end of the typical water flow rate range which is less than 0.02 kg/s per passive chilled beam.

Table 5-5. Maximum water flow rate of the passive chilled beam (constant speed pump scenario).

Maximum water flow rate of the passive chilled beam [kg/s per unit]					
Climate zone		**PCB 1**	**PCB 2**	**PCB 3**	**PCB 4**
Miami	1A	0.018	0.018	0.018	0.019
Houston	2A	0.016	0.016	0.016	0.019
Atlanta	3A	0.016	0.017	0.016	0.019
Philadelphia	4A	0.017	0.017	0.017	0.019
Lafayette	5A	0.016	0.016	0.016	0.022
Phoenix	2B	0.019	0.019	0.019	0.019
LA	3B	0.017	0.017	0.017	0.017
Prescott	4B	0.017	0.017	0.017	0.017
Salt Lake City	5B	0.018	0.018	0.018	0.018
San Francisco	3C	0.016	0.016	0.016	0.016
Seattle	4C	0.019	0.019	0.019	0.019

The minimum to maximum ranges of the passive chilled beams' surface temperature in all simulation cases (variable speed pump scenario) are listed in Table 5-6 which mostly varies from 17^{o}C to 22^{o}C for PCB 3 and 4 while the maximum chilled surface temperature goes up to around 23^{o}C for PCB 1 and 2. This is due to the lack of cooling capacity issue that was discussed in the previous section. However, for those cases where the "infeasible" option is not specified, the thermal condition was maintained properly for the entire simulation period as shown in section 5.1.4.1.

Table 5-6. Minimum / maximum surface temperatures of passive chilled beams (variable speed pump scenario).

Minimum / maximum surface temperatures of passive chilled beams [^{o}C]					
Climate zone		**PCB 1**	**PCB 2**	**PCB 3**	**PCB 4**
Miami	1A	17.4 - 22	18 - 22.6	17.5 - 21	17.5 - 21
Houston	2A	17.2 - 22	17.7 - 22.6	17.5 - 21.4	17.5 - 21.3
Atlanta	3A	17.1 - 22.3	17.6 - 23	17.3 - 21.2	17.3 - 21.2
Philadelphia	4A	infeasible	infeasible	17.4 - 21.2	17.4 - 21.2
Lafayette	5A	17.1 - 23.3	17.7 - 23.1	17.4 - 21.2	17.4 - 21.2
Phoenix	2B	17.3 - 22.6	infeasible	17.5 - 20.9	17.5 - 20.9
LA	3B	infeasible	17.6 - 23.6	17.3 - 21.1	17.2 - 21.1
Prescott	4B	infeasible	infeasible	17.3 - 21.2	17.3 - 21.2
Salt Lake City	5B	infeasible	infeasible	17.5 - 21.2	17.5 - 21.2
San Francisco	3C	infeasible	infeasible	17.2 - 21.1	17.2 - 21.1
Seattle	4C	infeasible	infeasible	17.2 - 21	17.2 - 21

Table 5-7 shows the median and maximum radiation cooling capacity in watts for all simulation cases (variable speed pump scenario). Values are fairly similar to each other for the different simulation cases.

Table 5-7. Median / maximum radiative cooling capacity of total passive chilled beams (variable speed pump scenario).

Median / Maximum radiative cooling capacity of total passive chilled beams [W]					
Climate zone		PCB 1	PCB 2	PCB 3	PCB 4
Miami	1A	486 / 634	463 / 592	500 / 627	501 / 627
Houston	2A	494 / 620	469 / 582	501 / 590	501 / 596
Atlanta	3A	476 / 630	447 / 599	498 / 614	502 / 616
Philadelphia	4A	infeasible	infeasible	504 / 630	503 / 629
Lafayette	5A	493 / 645	460 / 606	500 / 629	503 / 629
Phoenix	2B	504 / 617	infeasible	501 / 597	501 / 601
LA	3B	infeasible	404 / 589	496 / 614	507 / 615
Prescott	4B	infeasible	infeasible	500 / 622	501 / 622
Salt Lake City	5B	infeasible	infeasible	507 / 617	507 / 618
San Francisco	3C	infeasible	infeasible	488 / 608	502 / 608
Seattle	4C	infeasible	infeasible	512 / 636	513 / 637

Table 5-8 shows percentages of radiation cooling energy compared to the total passive chilled beam cooling energy for the entire simulation period for all simulation cases (variable speed pump scenario). Percentages of the radiation cooling energy are slightly decreased for PCB 1 and 2 compared to the constant speed pump scenario shown in Table 5-4. This is due to the slightly increased water supply temperature. Results of PCB 3 and 4 are similar to results of the constant speed pump scenario.

Table 5-8. Portion of radiation cooling against total passive chilled beam cooling demand (variable speed pump scenario).

Portion of radiation cooling against total passive chilled beam cooling demand [%]					
Climate zone		PCB 1	PCB 2	PCB 3	PCB 4
Miami	1A	12	13	15	8
Houston	2A	11	13	14	8
Atlanta	3A	11	12	14	8
Philadelphia	4A	infeasible	infeasible	12	8
Lafayette	5A	11	13	14	8
Phoenix	2B	7	infeasible	8	8
LA	3B	infeasible	11	15	8
Prescott	4B	infeasible	infeasible	9	8
Salt Lake City	5B	infeasible	infeasible	8	8
San Francisco	3C	infeasible	infeasible	14	9
Seattle	4C	infeasible	infeasible	9	7

Table 5-9 shows the maximum water flow rate through the passive chilled beams during the entire simulation period for all simulation cases (variable speed pump scenario). For variable speed pump scenario, the maximum water flow rates have greatly increased for PCB 1 and 2 to meet cooling capacity requirements while they remain similar for PCB 3 and 4 compared to the constant pump scenario shown in Table 5-5.

Table 5-9. Maximum water flow rate of the passive chilled beam (variable speed pump scenario).

Maximum water flow rate of the passive chilled beam [kg/s per unit]					
Climate zone		**PCB 1**	**PCB 2**	**PCB 3**	**PCB 4**
Miami	1A	0.06	0.029	0.018	0.019
Houston	2A	0.056	0.035	0.016	0.019
Atlanta	3A	0.074	0.057	0.016	0.02
Philadelphia	4A	infeasible	infeasible	0.018	0.02
Lafayette	5A	0.165	0.108	0.017	0.022
Phoenix	2B	0.061	infeasible	0.019	0.019
LA	3B	infeasible	0.079	0.017	0.018
Prescott	4B	infeasible	infeasible	0.018	0.018
Salt Lake City	5B	infeasible	infeasible	0.018	0.018
San Francisco	3C	infeasible	infeasible	0.017	0.017
Seattle	4C	infeasible	infeasible	0.019	0.019

CHAPTER 6. CONCLUSIONS AND FUTURE WORK

Conventional approaches for mapping the performance of passive chilled beam are reasonable for a particular application but are not adequate for incorporation in building simulation tools to enable assessments of overall energy usage and occupant comfort. Characterizing the performance of passive chilled beams was a primary focus of this thesis at both the component and system level.

A comprehensive performance characterization of the passive chilled beam was conducted. Models that can predict the total cooling capacity and chilled surface temperature of a passive chilled beam were developed based on experiments. These are semi-empirical models which use essential operating conditions of the system and thermal conditions in the environment as inputs, and they are able to predict energy and thermal comfort impacts of passive chilled beams when integrated in a system simulation. Performance measurements were compared between single passive chilled beam testing in a laboratory environment and multiple passive chilled beam testing from an office installation. The results indicate that the conventional method of predicting total cooling capacity of a passive chilled beam from individual laboratory tests underestimates its performance when installed in a system. These differences could influence optimal system sizing and commissioning and should be considered in future studies.

Side-by-side field measurements were conducted for a passive chilled beam system and conventional constant air volume and variable air volume systems that serve nearly identical office spaces. While maintaining the same thermal comfort levels in the two offices, the passive chilled beam system had 57% less total electric energy usage compared to the constant air volume system. However, the variable air volume system consumed 21% less energy compared to the passive chilled beam system during these

field measurements. This is mostly because of the current configuration of the passive chilled beam system which represents the worst case scenario in terms of system configuration. The parallel air system used in the field measurement is a typical air system including the outdoor air and return air damper system. As a starting point followed by various configurations assessment with computer simulations, the return air damper was closed during the entire field measurements of the passive chilled beam system. Thus, more realistic evaluations of the potential of alternative passive chilled beam system configurations were conducted using a computer simulation that was validated against the available measurements.

An integrated simulation tool was developed and validated for the field study office and then used to perform comprehensive comparisons of passive chilled beam and conventional systems. The primary goal was to evaluate alternative passive chilled beam system configurations under various climatic zones in order to evaluate energy savings for similar comfort conditions. While maintaining the same thermal environments in the office spaces, the best passive chilled beam system configuration led to electrical energy savings of up to 24% for hot and humid climates and up to 35% for hot and dry climates when compared to a variable air volume system.

The radiation cooling effects of passive chilled beams were also analyzed through experiments and simulations. Both experiments and computer simulations revealed that the effect of the radiation cooling of passive chilled beams was small in terms of energy savings and thermal comfort improvement. Based on simulation results covering various passive chilled beam system configurations and climatic zones, the percentage of radiation cooling energy relative to total passive chilled beam cooling energy varied between 7 to 15%.

Although a comprehensive effort was made to improve our understanding of the modeling and benefits of passive chilled beam systems, there are several recommendations for additional future studies.

- *Additional detailed investigation of the performance differences between test results for single passive chilled beam from laboratory experiments and multiple passive*

chilled beams in office environments: Due to the physical characteristics of natural convection, the primary reason for the differences between the Bowen and Living Lab chilled beam performance could be related to differences in the available area above the chilled beam, local air movement driven by the parallel air system and/or internal gains. The specific reasons and remedies for the different behavior of laboratory and in-situ passive chilled beam performance should be considered in future studies in order to develop better models and design approaches.

- *Analysis of the air flow field below multiple passive chilled beams combined with the parallel air system*: Analysis of the air flow field below the passive chilled beam is also an important topic in terms of precisely predicting the thermal comfort within the space. Since the flow is unstable and significantly affected by internal gains at the breathing level, a numerical or CFD study on the flow field should be considered in future studies.

- *Economic analysis of passive chilled beam system applications*: This study only focused on energy savings potential of using passive chilled beam systems. However, in order to have an impact on market penetration, the energy savings results should be combined with a detailed economic analysis.

LIST OF REFERENCES

LIST OF REFERENCES

[1] *Energy technology perspectives 2012, Pathways to a Clean Energy System*, SECOND EDITION. Paris: International Energy Agency (IEA), 2012.

[2] J. D. Feng, F. Bauman, and S. Schiavon, "Critical review of water based radiant cooling system design methods," *Indoor Air 2014*, Jan. 2014.

[3] T. Moore, F. Bauman, and C. Huizenga, "Radiant cooling research scoping study," *eScholarship*, Apr. 2006.

[4] ASHRAE, American Society of Heating, Refrigerating and Air-conditioning Engineers, *ASHRAE systems and equipment handbook*. Atlanta, GA: American Society of Heating, Refrigerating and Air-Conditioning Engineers, 2004.

[5] K. W. Roth, D. Westphalen, J. Dieckmann, S. D. Hamilton, and W. Goetzler, "Energy Consumption Characteristics of Commercial Building HVAC Systems Volume III: Energy Savings Potential," Department of Energy (DOE), DE-AC01-96CE23798, 2002.

[6] "Fläkt Woods," Accessed on-2014. [Online]. Available: www.flaktwoods.com.

[7] "Halton," Accessed on-2014. [Online]. Available: www.halton.com.

[8] "Price," Accessed on-2014. [Online]. Available: www.price-hvac.com.

[9] "TROX USA," Accessed on-2014. [Online]. Available: www.troxusa.com.

[10] J. D. Feng, S. Schiavon, and F. Bauman, "Cooling load differences between radiant and air systems," *Energy Build.*, vol. 65, pp. 310–321, Oct. 2013.

[11] J. D. Feng, "Design and Control of Hydronic Radiant Cooling Systems," *eScholarship*, Apr. 2014.

[12] C. Karmann, S. Schiavon, and F. Bauman, "Online map of buildings using radiant technologies," *Proc. Indoor Air 2014*, Jul. 2014.

[13] "Building environment design -- Design, dimensioning, installation and control of embedded radiant heating and cooling systems -- Part 1: Definition, symbols, and comfort criteria." International Organization for Standardization, 25-Jul-2012.

[14] “Building environment design -- Design, dimensioning, installation and control of embedded radiant heating and cooling systems -- Part 2: Determination of the design heating and cooling capacity.” International Organization for Standardization, 24-Sep-2012.

[15] “Building environment design -- Design, dimensioning, installation and control of embedded radiant heating and cooling systems -- Part 3: Design and dimensioning.” International Organization for Standardization, 24-Sep-2012.

[16] “Building environment design -- Design, dimensioning, installation and control of embedded radiant heating and cooling systems -- Part 4: Dimensioning and calculation of the dynamic heating and cooling capacity of Thermo Active Building Systems (TABS).” International Organization for Standardization, 25-Jul-2012.

[17] “Building environment design -- Design, dimensioning, installation and control of embedded radiant heating and cooling systems -- Part 5: Installation.” International Organization for Standardization, 11-Apr-2012.

[18] “Building environment design -- Design, dimensioning, installation and control of embedded radiant heating and cooling systems -- Part 6: Control.” International Organization for Standardization, 18-Sep-2013.

[19] ASHRAE, American Society of Heating, Refrigerating and Air-conditioning Engineers, “Chapter 6 - Panel Heating and Cooling,” in *2008 ASHRAE Handbook—HVAC Systems and Equipment (SI)*, 2008, p. 6.1-6.21.

[20] “S&P Coil Products Ltd.,” 20-Apr-2015. [Online]. Available: www.spcoils.co.uk.

[21] “emco klima,” 20-Apr-2015. [Online]. Available: www.emco-klima.com.

[22] “Natural Resources Canada,” 30-Mar-2015. [Online]. Available: www.nrcan.gc.ca/science/story/3725.

[23] M. Virta *et al.*, *Chilled beam application guidebook*. REHVA (Federation of European Heating and Airconditioning Associations), 2004.

[24] J. Woollett and J. Rimmer, *Active and Passive Beam Application Design Guide*. REHVA (Federation of European Heating and Airconditioning Associations), 2015.

[25] ECS, *BS EN 14518:2005: Ventilation for buildings. Chilled beams. Testing and rating of passive chilled beams*, vol. European Committee for Standardization. 2005.

[26] J. Kim, A. Tzempelikos, and J. E. Braun, “Review of modelling approaches for passive ceiling cooling systems,” *J. Build. Perform. Simul.*, vol. 8, no. 3, pp. 145–172, May 2015.

[27] S. G. Hodder, D. L. Loveday, K. C. Parsons, and A. H. Taki, “Thermal comfort in chilled ceiling and displacement ventilation environments: vertical radiant temperature asymmetry effects,” *Energy Build.*, vol. 27, no. 2, pp. 167–173, 1998.

[28] T. Imanari, T. Omori, and K. Bogaki, “Thermal comfort and energy consumption of the radiant ceiling panel system.: Comparison with the conventional all-air system,” *Energy Build.*, vol. 30, pp. 167–175, 1999.

[29] L. Schellen, M. G. L. C. Loomans, M. H. de Wit, B. W. Olesen, and W. D. van M. Lichtenbelt, “The influence of local effects on thermal sensation under non-uniform environmental conditions — Gender differences in thermophysiology, thermal comfort and productivity during convective and radiant cooling,” *Physiol. Amp Behav.*, vol. 107, no. 2, pp. 252–261, 2012.

[30] D. L. Loveday, K. C. Parsons, A. H. Taki, and S. G. Hodder, “Displacement ventilation environments with chilled ceilings: thermal comfort design within the context of the BS EN ISO7730 versus adaptive debate,” *Energy Build.*, vol. 34, no. 6, pp. 573–579, 2002.

[31] K. Nagano and T. Mochida, “Experiments on thermal environmental design of ceiling radiant cooling for supine human subjects,” *Build. Environ.*, vol. 39, no. 3, pp. 267–275, 2004.

[32] S. J. Rees and P. Haves, “An Experimental Study of Air Flow and Temperature Distribution in a Room with Displacement Ventilation and a Chilled Ceiling,” *Build. Environ.*, no. 0, 2012.

[33] S. Oxizidis and A. M. Papadopoulos, “Performance of radiant cooling surfaces with respect to energy consumption and thermal comfort,” *Energy Build.*, vol. 57, pp. 199–209, 2013.

[34] A. S. Binghooth and Z. A. Zainal, “Performance of desiccant dehumidification with hydronic radiant cooling system in hot humid climates,” *Energy Build.*, vol. 51, no. 0, pp. 1–5, 2012.

[35] Í. B. Kilkis, S. S. Sager, and M. Uludag, “A simplified model for radiant heating and cooling panels,” *Simul. Pract. Theory*, vol. 2, no. 2, pp. 61–76, 1994.

[36] Í. B. Kilkis, “Enhancement of heat pump performance using radiant floor heating systems,” *ASME AES*, vol. 28, pp. 119–127, 1992.

[37] Í. B. Kilkis, “Radiant ceiling cooling with solar energy: Fundamentals, modeling and a case design,” *ASHRAE Trans*, vol. 99, pp. 521–533, 1993.

[38] T. C. Min, L. F. Schutrum, G. V. Parmelee, and J. D. Vouris, “Natural convection and radiation in a panel heated room,” *ASHRAE Trans.*, vol. 62, pp. 337–58, 1956.

[39] F. J. Kreider and F. Kreith, *Solar energy handbook*. New York: McGraw-Hill, 1981.

[40] I. B. Kilkis, S. S. Sager, and M. Uludag, “Thermo-hydraulic simulation of radiant floor heated indoor spaces,” presented at the International ANSYS Conference, 1994.

[41] M. Koschenz and V. Dorer, “Interaction of an air system with concrete core conditioning,” *Energy Build.*, vol. 30, no. 2, pp. 139–145, 1999.

[42] B. Glück, *Wärmeübergang*. Berlin: VEB Verlag für Bauwesen, 1989.

[43] B. Glück, *Strahlungsheizung – Theorie und Praxis*. Verlag C. F. Müller, 1982.

[44] C. L. Conroy and S. A. Mumma, “Ceiling Radiant Cooling Panels as a Viable Distributed Parallel Sensible Cooling Technology Integrated with Dedicated Outdoor-Air Systems,” *ASHRAE Trans.*, vol. 107, no. 1, pp. 578–85, 2001.

[45] J.-W. Jeong and S. A. Mumma, “Ceiling radiant cooling panel capacity enhanced by mixed convection in mechanically ventilated spaces,” *Appl. Therm. Eng.*, vol. 23, no. 18, pp. 2293–2306, 2003.

[46] J.-W. Jeong and S. A. Mumma, “Simplified cooling capacity estimation model for top insulated metal ceiling radiant cooling panels,” *Appl. Therm. Eng.*, vol. 24, no. 14–15, pp. 2055–2072, 2004.

[47] J.-W. Jeong and S. A. Mumma, “Practical cooling capacity estimation model for a suspended metal ceiling radiant cooling panel,” *Build. Environ.*, vol. 42, no. 9, pp. 3176–3185, 2007.

[48] D. Montgomery, *Design and analysis of experiments*, 5th ed. New York: Wiley, 2001.

[49] J. A. Duffie and W. A. Beckman, *Solar engineering of thermal processes*, 2nd ed. New York: Wiley Interscience, 1991.

[50] Z. Tian, X. Yin, Y. Ding, and C. Zhang, “Research on the actual cooling performance of ceiling radiant panel,” *Energy Build.*, vol. 47, no. 0, pp. 636–642, 2012.

[51] R. K. Strand and K. T. Baumgartner, “Modeling radiant heating and cooling systems: integration with a whole-building simulation program,” *Energy Build.*, vol. 37, no. 4, pp. 389–397, 2005.

[52] R. K. Strand and C. O. Pederson, “Modeling radiant systems in an integrated heat balance based energy simulation program,” *ASHRAE Trans.*, vol. 108, no. 2, pp. 1–9, 2002.

[53] *EnergyPlus*. 2015.

[54] D. B. Crawley *et al.*, “EnergyPlus: creating a new-generation building energy simulation program,” *Energy Build.*, vol. 33, no. 4, pp. 319–331, 2001.

[55] E. Fabrizio, S. P. Corgnati, F. Causone, and M. Filippi, “Numerical comparison between energy and comfort performances of radiant heating and cooling systems versus air systems,” *HVACR Res.*, vol. 18, pp. 692–708, 2012.

[56] P. Raftery, K. H. Lee, T. Webster, and F. Bauman, “Performance analysis of an integrated UFAD and radiant hydronic slab system,” *Appl. Energy*, vol. 90, no. 1, pp. 250–257, 2012.

[57] T. Weber and G. Jóhannesson, “An optimized RC-network for thermally activated building components,” *Build. Environ.*, vol. 40, no. 1, pp. 1–14, Jan. 2005.

[58] H. Carslaw and J. Jaeger, *Conduction of heat in solids*. Oxford Science Publication: Clarendon Press Oxford, 1959.

[59] J. Akander, “The ORC method - effective modelling of multilayer building components,” Doctoral Dissertation, Department of Building Sciences, KTH-Royal Institute of Technology, Stockholm, 2000.

[60] T. Weber, G. Jóhannesson, M. Koschenz, B. Lehmann, and T. Baumgartner, “Validation of a FEM-program (frequency-domain) and a simplified RC-model (time-domain) for thermally activated building component systems (TABS) using measurement data,” *Energy Build.*, vol. 37, no. 7, pp. 707–724, Jul. 2005.

[61] S. Okamoto, H. Kitora, H. Yamaguchi, and T. Oka, “A simplified calculation method for estimating heat flux from ceiling radiant panels,” *Energy Build.*, vol. 42, pp. 29–33, 2010.

[62] S. Okamoto, M. Miura, H. Yamaguchi, K. Omoto, M. Takaoka, and T. Oka, “Comparison between the calculation method for estimating heat fluxes of radiation and convection of ceiling radiant panels and experiment data,” *J. Environ. Eng. Trans. AIJ*, vol. 73, pp. 221–227, 2008.

[63] *DOE 2.1E*. 2015.

[64] A. Livchak and C. Lowell, “Don’t turn active beams into expensive diffusers,” *ASHRAE J.*, pp. 52–60, Apr. 2012.

[65] “DOE 2.1E Manual,” 25-Sep-2014. [Online]. Available: http://simulationresearch.lbl.gov/dirsoft/21e_update2.pdf.

[66] “EnergyPlus Manual,” 25-Sep-2014. [Online]. Available: http://apps1.eere.energy.gov/buildings/energyplus/pdfs/engineeringreference.pdf.

[67] K. A. Antonopoulos, “Analytical and numerical heat transfer in cooling panels,” *Int. J. Heat Mass Transf.*, vol. 35, no. 11, pp. 2777–2782, 1992.

[68] K. A. Antonopoulos and F. Democritou, “Periodic steady-state heat transfer in cooling panels,” *Int. J. Heat Fluid Flow*, vol. 14, no. 1, pp. 94–100, 1993.

[69] K. A. Antonopoulos, M. Vrachopoulos, and C. Tzivanidis, “Experimental and theoretical studies of space cooling using ceiling-embedded piping,” *Appl. Therm. Eng.*, vol. 17, no. 4, pp. 351–367, 1997.

[70] K. A. Antonopoulos and C. Tzivanidis, “Numerical solution of unsteady three-dimensional heat transfer during space cooling using ceiling-embedded piping,” *Energy*, vol. 22, no. 1, pp. 59–67, 1997.

[71] M. Tye-Gingras and L. Gosselin, “Investigation on heat transfer modeling assumptions for radiant panels with serpentine layout,” *Energy Build.*, vol. 43, no. 7, pp. 1598–1608, 2011.

[72] J. A. Castillo and R. Tovar, “Transient cooling of a room with a chilled ceiling,” *Sol. Energy*, vol. 86, no. 4, pp. 1029–1036, 2012.

[73] B. R. Morton, G. I. Taylor, and J. S. Turner, “Turbulent gravitational convection from maintained and instantaneous sources,” *Proc. R. Soc. A*, vol. 234, pp. 1–23, 1956.

[74] W. D. Baines and J. S. Turner, “Turbulent buoyant convection from a source in a confined region,” *J. Fluid Mech.*, vol. 37, pp. 51–80, 1969.

[75] S. J. Rees and P. Haves, “A nodal model for displacement ventilation and chilled ceiling systems in office spaces,” *Build. Environ.*, vol. 36, no. 6, pp. 753–762, 2001.

[76] S. Klien and F. Alvarado, *EES engineering equation solver*. Wisconsin: F-chart software, 1997.

[77] K. Ben Nasr, R. Chouikh, C. Kerkeni, and A. Guizani, “Numerical study of the natural convection in cavity heated from the lower corner and cooled from the ceiling,” *Appl. Therm. Eng.*, vol. 26, no. 7, pp. 772–775, 2006.

[78] M. Ayoub, N. Ghaddar, and K. Ghali, “Simplified Thermal Model of Spaces Cooled with Combined Positive Displacement Ventilation and Chilled Ceiling System,” *HVACR Res.*, vol. 12, pp. 1005–1030, 2006.

[79] N. Ghaddar, K. Ghali, R. Saadeh, and A. Keblawi, “Design charts for combined chilled ceiling displacement ventilation system,” *ASHRAE Trans.*, vol. 143, no. 2, pp. 574–587, 2008.

[80] A. Keblawi, N. Ghaddar, K. Ghali, and L. Jensen, “Chilled ceiling displacement ventilation design charts correlations to employ in optimized system operation for feasible load ranges,” *Energy Build.*, vol. 41, no. 11, pp. 1155–1164, 2009.

[81] T. Kim, D. Song, S. Kato, and S. Murakami, “Two-step optimal design method using genetic algorithms and CFD-coupled simulation for indoor thermal environments,” *Appl. Therm. Eng.*, vol. 27, no. 1, pp. 3–11, 2007.

[82] T. Catalina, J. Virgone, and F. Kuznik, “Evaluation of thermal comfort using combined CFD and experimentation study in a test room equipped with a cooling ceiling,” *Build. Environ.*, vol. 44, no. 8, pp. 1740–1750, 2009.

[83] K. Abe, T. Kondoh, and Y. Nagano, “A new turbulence model for predicting fluid flow and heat transfer in separating and reattaching flows—I. Flow field calculations,” *Int. J. Heat Mass Transf.*, vol. 37, pp. 139–151, 1994.

[84] S. P. Corgnati, M. Perino, G. V. Fracastoro, and P. V. Nielsen, “Experimental and numerical analysis of air and radiant cooling systems in offices,” *Build. Environ.*, vol. 44, pp. 801–806, 2009.

[85] R. Karadağ, “New approach relevant to total heat transfer coefficient including the effect of radiation and convection at the ceiling in a cooled ceiling room,” *Appl. Therm. Eng.*, vol. 29, no. 8–9, pp. 1561–1565, 2009.

[86] R. Karadağ and I. Teke, “New approach relevant to floor Nusselt number in floor heating system,” *Energy Convers. Manag.*, vol. 49, no. 5, pp. 1134–1140, 2008.

[87] R. Karadağ, “The investigation of relation between radiative and convective heat transfer coefficients at the ceiling in a cooled ceiling room,” *Energy Convers. Manag.*, vol. 50, no. 1, pp. 1–5, 2009.

[88] A. H. Taki, L. Jalil, and D. L. Loveday, “Experimental and computational investigation into suppressing natural convection in chilled ceiling/displacement ventilation environments,” *Energy Build.*, vol. 43, no. 11, pp. 3082–3089, 2011.

[89] W.-H. Chiang, C.-Y. Wang, and J.-S. Huang, “Evaluation of cooling ceiling and mechanical ventilation systems on thermal comfort using CFD study in an office for subtropical region,” *Build. Environ.*, vol. 48, no. 0, pp. 113–127, 2012.

[90] A. Novoselac, B. J. Burley, and J. Srebric, “New Convection Correlations for Cooled Ceiling Panels in Room with Mixed and Stratified Airflow,” *HVACR Res.*, vol. 12, pp. 279–294, 2006.

[91] F. Causone, S. P. Corgnati, M. Filippi, and B. W. Olesen, “Experimental evaluation of heat transfer coefficients between radiant ceiling and room,” *Energy Build.*, vol. 41, no. 6, pp. 622–628, 2009.

[92] M. Andrés-Chicote, A. Tejero-González, E. Velasco-Gómez, and F. J. Rey-Martínez, “Experimental study on the cooling capacity of a radiant cooled ceiling system,” *Energy Build.*, vol. 54, no. 0, pp. 207–214, 2012.

[93] N. F. Díaz and C. Cuevas, “Testing and thermal modeling of radiant panels systems as commissioning tool,” *Energy Convers. Manag.*, vol. 51, no. 12, pp. 2663–2677, 2010.

[94] N. F. Díaz, C. Cuevas, and V. Lemort, “Radiant ceiling systems coupled to its environment part 1: Experimental analysis,” *Appl. Therm. Eng.*, vol. 30, no. 14–15, pp. 2187–2195, 2010.

[95] N. F. Díaz, J. Lebrun, and P. André, “Experimental study and modeling of cooling ceiling systems using steady-state analysis,” *Int. J. Refrig.*, vol. 33, no. 4, pp. 793–805, 2010.

[96] N. F. Díaz, S. Bertagnolio, and C. Cuevas, “Radiant ceiling systems coupled to its environment part 2: Dynamic modeling and validation,” *Appl. Therm. Eng.*, vol. 30, no. 14–15, pp. 2196–2203, 2010.

[97] N. F. Díaz, “Experimental study of hydronic panels system and its environment,” *Energy Convers. Manag.*, vol. 52, no. 1, pp. 770–780, 2011.

[98] N. F. Díaz, “Experimental analysis and modeling of hydronic radiant ceiling panels using transient-state analysis,” *Int. J. Refrig.*, vol. 34, no. 4, pp. 958–967, 2011.

[99] N. F. Díaz, “Modeling of a hydronic ceiling system and its environment as energetic auditing tool,” *Appl. Energy*, vol. 88, no. 3, pp. 636–649, 2011.

[100] P. Celata, M. Cumo, J. McPhail, and G. Zummo, “Single-phase laminar and turbulent heat transfer in smooth and rough microtubes,” *Microfluid Nanofluids*, vol. 3, pp. 697–707, 2007.

[101] J. Niu and J. V. D. Kooi, “Dynamic simulation of combination of evaporative cooling with cooled ceiling systems for office room cooling,” presented at the Proc. Building Simulation ’93 - Third Int. Conf., 1993, pp. 16–18.

[102] J. Niu, “Modelling of cooled-ceiling air-conditioning systems - Influences on indoor environment and energy consumption,” Delft University of Technology, Netherlands, 1994.

[103] Q. Chen and J. V. D. Kooi, “ACCURACY: a computer program for combined problems of energy analysis, indoor air flow and air quality,” *ASHRAE Trans 94 Part2*, pp. 196–214, 1988.

[104] J. Niu, J. v d Kooi, and H. v d Rhee, “Energy saving possibilities with cooled-ceiling systems,” *Energy Build.*, vol. 23, no. 2, pp. 147–158, 1995.

[105] H. G. Z. J. L Niu, “SIMULATION METHODOLOGY OF RADIANT COOLING WITH ELEVATED AIR MOVEMENT.”

[106] J. L. Niu, L. Z. Zhang, and H. G. Zuo, “Energy savings potential of chilled-ceiling combined with desiccant cooling in hot and humid climates,” *Energy Build.*, vol. 34, no. 5, pp. 487–495, Jun. 2002.

[107] X. Wang, J. Niu, and A. H. C. van Paassen, “Raising evaporative cooling potentials using combined cooled ceiling and MPCM slurry storage,” *Energy Build.*, vol. 40, no. 9, pp. 1691–1698, 2008.

[108] L. Z. Zhang and J. L. Niu, “Indoor humidity behaviors associated with decoupled cooling in hot and humid climates,” *Build. Environ.*, vol. 38, no. 1, pp. 99–107, Jan. 2003.

[109] C. Stetiu, H. E. Feustel, and F. C. Winkelmann, “Development of a simulation tool to evaluate the performance of radiant cooling ceilings,” Lawrence Berkeley Laboratory, 1995.

[110] C. Stetiu, “Energy and peak power savings potential of radiant cooling systems in US commercial buildings,” *Energy Build.*, vol. 30, no. 2, pp. 127–138, 1999.

[111] L. Ferkl and Š. Jan, “Ceiling radiant cooling: Comparison of ARMAX and subspace identification modelling methods,” *Build. Environ.*, vol. 45, no. 1, pp. 205–212, 2010.

[112] G. Ge, F. Xiao, and S. Wang, “Neural network based prediction method for preventing condensation in chilled ceiling systems,” *Energy Build.*, vol. 45, no. 0, pp. 290–298, 2012.

[113] M. Mossolly, K. Ghali, N. Ghaddar, and L. Jensen, “Optimized Operation of Combined Chilled Ceiling Displacement Ventilation System Using Genetic Algorithm,” *ASHRAE Trans.*, vol. 114, pp. 541–554, 2008.

[114] Y.-C. Chan and A. Tzempelikos, “Analysis and comparison of absorbed solar radiation distribution models in perimeter building zones,” *ASHRAE Trans*, vol. accepted for publication, 2013.

[115] J. E. Braun, S. A. Klein, and J. W. Mitchell, “Effectiveness models for cooling towers and cooling coils,” *ASHRAE Trans*, vol. 95, pp. 164–174, 1989.

[116] H. Koskela, H. Häggblom, R. Kosonen, and M. Ruponen, “Air distribution in office environment with asymmetric workstation layout using chilled beams,” *Build. Environ.*, vol. 45, no. 9, pp. 1923–1931, 2010.

[117] J. Fredriksson, M. Sandberg, and B. Moshfegh, “Experimental investigation of the velocity field and airflow pattern generated by cooling ceiling beams,” *Build. Environ.*, vol. 36, no. 7, pp. 891–899, 2001.

[118] J. Fredriksson and M. Sandberg, “The effect of false ceiling on the cooling capacity of passive chilled beams,” *Build. Environ.*, vol. 44, no. 7, pp. 1426–1430, 2009.

[119] I. C. Nelson, C. H. Culp, J. Rimmer, and B. Tully, “The effect of thermal load configuration on the performance of passive chilled beams,” *Build. Environ.*, vol. 96, pp. 188–197, Feb. 2016.

[120] G. Sastry and P. Rumsey, “VAV vs. Radiant, Side-by-Side Comparison,” *ASHRAE J.*, pp. 16–24, May 2014.

[121] H. Shen and A. Tzempelikos, “Daylighting and energy analysis of private offices with automated interior roller shades,” *Sol. Energy*, vol. 86, no. 2, pp. 681–704, Feb. 2012.

[122] J. Kim, J. E. Braun, and A. Tzempelikos, “Characterizing the In-Situ Performance of Passive Chilled Beams,” *ASHRAE Trans.*, vol. 121, 2015.

[123] *Methods of Testing Chilled Beams*. ANSI/ASHRAE Standard 200-2015, 2015.

[124] *ExSelAir*. http://exselair-web.flaktwoods.com/?UICulture=: Flaktwoods.

[125] S. J. Kline and F. A. McClintock, “Describing Uncertainties in Single Sample Experiments,” *Mech Eng*, pp. 3–8, Jan. 1953.

[126] ASHRAE, American Society of Heating, Refrigerating and Air-conditioning Engineers, *Standard 55-Thermal Environmental Conditions for Human Occupancy*. 2013.

[127] ASHRAE, American Society of Heating, Refrigerating and Air-conditioning Engineers, *Standard 62.1-Ventilation for Acceptable Indoor Air Quality*. 2010.

[128] ASHRAE, American Society of Heating, Refrigerating and Air-conditioning Engineers, *Standard 90.1-Energy Standard for Buildings except Low-rise Residential Buildings*. 2010.

[129] J. R. Howell, M. P. Mengüç, and R. Siegel, *Thermal Radiation Heat Transfer, 5th Edition*. 2011.

[130] Thornton, B.A. et al., "Achieving the 30% Goal: Energy and Cost Savings Analysis of ASHRAE Standard 90.1-2010," Pacific Northwest National Laboratory, PNNL-20405, 2011.

[131] A Transient System Simulation Program, Version 17, *TRNSYS*. University of Wisconsin, 2015.

[132] J. J. Jurinak, "Open cycle solid desiccant cooling—component models and system simulation," Ph.D. Thesis, University of Wisconsin-Madison, 1982.

[133] J. Kim, J. E. Braun, A. Tzempelikos, and W. T. Horton, "Performance Evaluation of a Passive Chilled Beam System and Comparison with a Conventional Air System," *Proc. 4th High Perform. Build. Conf. Purdue*, Jul. 2016.

[134] ASHRAE, American Society of Heating, Refrigerating and Air-conditioning Engineers, *Standard 84-Method of Testing Air-to-Air Heat/Energy Exchangers*. 2013.

[135] AHRI Guideline V, *2011 Guideline for Calculating the Efficiency of Energy Recovery Ventilation and its Effect on Efficiency and Sizing of Building HVAC Systems*. 2011.

[136] SEMCO, A Fläkt Woods Company, "AHRI GUIDELINE V: RECOVERY EFFICIENCY RATIO (RER) AND COMBINED EFFICIENCY (CEF)."

[137] J. Kim, J. E. Braun, and A. Tzempelikos, "Energy Savings Potential of Passive Chilled Beam System as a Retrofit Option for Commercial Buildings in Different Climates," *Proc. 3rd High Perform. Build. Conf. Purdue*, 2014.

VITA

VITA

Janghyun Kim
Ray W. Herrick Laboratories, School of Mechanical Engineering
Purdue University

Education and Training

Purdue University, West Lafayette, Indiana, US *Doctor of Philosophy, Mechanical Engineering*	Sep 2011 – Dec 2016
Hanyang University, Seoul, South Korea *Master of Science, Mechanical Engineering*	Mar 2009 – Feb 2011
Hanyang University, Seoul, South Korea *Bachelor of Science, Mechanical Engineering*	Mar 2007 – Feb 2009
Republic of Korea Army, Seoul, South Korea *Korean Augmentation to the United States Army*	Oct 2004 – Oct 2006
Hongik University, Seoul, South Korea *Freshman-Sophomore, Mechanical Engineering*	Mar 2002 – Feb 2004

Research Interests

Optimization of a passive chilled beam system

Development of commercial building HVAC retrofit solutions

HVAC equipment modeling (empirical and theoretical)